Ola Mosebø Haukeland

Experimental Testing, Dynamic Modeling and Control of Roll and Pitch for a SES with a Split Cushion

Master's thesis in marine cybernetics
Supervisor: Vahid Hassani, IMT
Co-supervisor: Øyvind Auestad, Umoe Mandal
Co-supervisor: Jan Tommy Gravdahl, ITK
June 2019

Norwegian University of Science and Technology
Faculty of Engineering
Department of Marine Technology

NTNU
Norwegian University of
Science and Technology

Abstract

This master thesis investigates the roll and pitch damping properties of a surface effect ship with an air cushion that is divided into four separate cushion chambers. This new four cushion solution makes it possible to generate a counteracting roll and pitch moment by manipulating the pressure inside each of the cushion chambers.

Umoe Mandal has developed a mathematical model that is used to simulate the cushion dynamics of a single cushion surface effect ship. In this thesis, the model is expanded to express the cushion dynamics and cushion forces for a vessel with four cushions. In addition, the existing model is altered to account for varying cushion chamber geometry as a function of the heave, roll and pitch motion of the vessel. Some additional minor changes are also made to the mathematical model with respect to the cushion air flow. The mathematical model is implemented in MATLAB®/Simulink® and is combined with a larger system used to simulate waves and the hydrodynamic forces acting on the vessel hull. Two simple PID controllers are designed and applied for control of heave, roll and pitch.

Towards the end of the project several model scale tests are performed in the NTNU wave basin. The results from these tests confirm that the mathematical model acts as a good approximation of the physical system. The data from these experiments also confirm the efficacy of the roll and pitch damping capabilities of the split cushion SES. For the wave basin tests simulating regular waves, the peak to peak roll angle is reduced by as much as 76.7%. For irregular JONSWAP sea, the significant roll angle is reduced by as much as 54.2% . For pitch damping, the same numbers are 66.8% and 49.8% damping respectively. The results generated from the numerical simulations indicate that under more ideal conditions, as much as 80-90% damping for both roll and pitch may be obtainable.

The model tests take place quite close to the thesis deadline, and further work should include further analysis of the data from the scale model tests. With respect to the mathematical model, the initial results from the scale model tests indicate that further work should include improving on the modeling of the cushion air flow, specifically the cushion air leakage. Controlling the airflow within the cushion chambers is key to maintain a good degree of motion control. For the physical implementation, the cushion separation walls need to be retractable during transit. In addition, the separation walls must be designed to minimize the air leakage from chamber to chamber during pitch and roll control. Though the current solution provides very promising results, further work and improvement on this design may produce even better results.

Sammendrag

Denne masteroppgaven undersøker egenskapene for rull og trim demping til et overflateeffektskip med en luftpute som er delt inn i fire separate putekamre. Denne nye puteinndelingen gjør det mulig å generere et motvirkende rull og trim moment ved å manipulere trykket i hvert av putekamrene.

Umoe Mandal har utviklet en matematisk modell som kan brukes til å simulere pute dynamikken for et overflateeffektskip med én luftpute. I denne oppgaven blir modellen utvidet for å uttrykke pute dynamikken og å regne ut de tilhørende putekreftene for en SES med fire luftputer. I tillegg blir den eksisterende modellen endret for å ta hensyn til varierende putekammergeometri som en funksjon av hiv, rull og trim. Noen ekstra endringer i den matematiske modellen gjøres med hensyn til luftstrømmen inn og ut av putekammerene. Den matematiske modellen er implementert i MATLAB®/Simulink® og innlemmes i et større system som brukes til å simulere bølger og de hydrodynamiske kreftene som virker på fartøyets skrog. To enkle PID-kontrollere designes og anvendes for kontroll av hiv, rull og trim.

Mot slutten av prosjektet utføres flere modellskalaforsøk i NTNU sitt bølgebasseng. Resultatene fra disse testene brukes til å verifisere nøyaktigheten til den matematiske modellen. Dataene som samles fra disse testene bekrefter at den matematiske modellen fungerer som en god tilnærming av det fysiske systemet. Dataene fra disse forsøkene bekrefter også at rull- og trimdemping egenskapene til en SES med fire putekammer er betraktelige. For bølgebassengtestene med regulære bølger reduseres rullbevegelsen med opp til 76,7%. For irregulær JONSWAP sjø reduseres den signifikante rullevinkelen med så mye som 54,2%. For trimdemping er de tilsvarende tallene henholdsvis 66,8% og 49,8%. Resultater generert fra de numeriske simuleringene indikerer at under mer ideelle forhold kan så mye som 80-90% demping av rull og trim være oppnåelig.

Modeltestene utføres ganske nær avhandlingsfristen og videre arbeid burde derfor omfatte en dypere analyse av dataene fra modellskalatestene. Med hensyn på den matematiske modellen indikerer resultatene fra skalamodelltestene at videre arbeid burde omfatte en forbedring av modelleringen av luftstrømmen ut av putene, spesielt med tanke på luftlekkasje. Kontroll av luftstrømmen inn og ut av putekamrene er kritisk for å opprettholde god kontroll over bevegelsene til skipet. For en fysisk implementering i fullskala må veggene som inndeler luftputekammerene være mulige å trekke tilbake når skipet skal forflytte seg. Samtidig må veggene som inndeler luftputekammerene være utformet for å minimere luftlekkasjen fra kammer til kammer når kontroll av rull og trim er ønsket. Den nåværende løsningen gir svært lovende resultater, men videre arbeid og forbedring av denne inndelingen vil trolig kunne gi enda bedre resultater.

Preface

The objective of this master thesis is to develop a mathematical model of a split cushion SES, design a control system, and investigate the roll and pitch damping properties. Furthermore, a scale model experiment is carried out to verify the validity of the model and damping properties of the vessel. A large portion of this thesis has gone into creation and implementation of the mathematical model. The complete SES-sim model is large and complex, and troubleshooting in both new and existing parts of the model has shown to be quite tedious work. A big thanks is owed to Umoe Mandal for letting me work on their existing model, providing me with documentation and for the close cooperation and help they have provided.

In addition to the mathematical modeling, the scale model testing as well as analysis and presentation of the gathered data has been long and painstaking work. The model has a lot of moving parts and from the testing an immense amount of data was gathered. Initially, the goal was to do a rudimentary analysis of the scale model data, and a simple comparison with the mathematical model. However, as the hours went by, the rabbit hole grew deeper, and it eventually became clear that a swift analysis of the data would neither become a good nor an accurate analysis. To maintain the accuracy and truthfulness of the conclusions drawn through the analysis of the scale model data, the analysis contains a lot of caveats and has become more entangled and convoluted than initially intended.

A big thanks is owed to my supervisor, associate professor Vahid Hassani, for suggesting this thesis for me. Thanks for all your good suggestions and help. In stressing periods of the thesis work, taking a chat with you would invariably be calming and reassuring.

Finally, a special thanks is owed to Dr. Øyvind Auestad at Umoe Mandal for his role as a sparring partner and mentor. Thanks for always being available, for all the good tips and ideas, and for all the time and effort you have dedicated to me and my work through the span of this thesis.

Table of Contents

Abstract **i**

Sammendrag **ii**

Preface **iii**

List of Figures **ix**

List of Tables **xi**

1 Introduction **1**
- 1.1 Motivation 2
- 1.2 Existing motion control 2
  - 1.2.1 Roll damping 3
  - 1.2.2 Pitch damping 3
- 1.3 Existing SES cushion control systems 4
- 1.4 The vessel 6
  - 1.4.1 Cushions 6
  - 1.4.2 Cushion air flow 8
- 1.5 The model-scaled vessel 9
  - 1.5.1 Instrumentation 9
  - 1.5.2 Scaling 12
  - 1.5.3 Cushion seals and separation walls 12
- 1.6 Model testing 14
- 1.7 Presentations of results 14

2 Mathematical model **15**
- 2.1 Contribution of the thesis 15
- 2.2 Equations of motion 16
- 2.3 Variable cushion length 17
- 2.4 Cushion geometry 18

2.5 Pressure area . . . 19
2.5.1 Center of pressure . . . 20
2.6 Cushion volume . . . 21
2.7 Wave volume and wave volume pumping . . . 23
2.8 Linearized cushion pressure dynamics . . . 24
2.9 Non-linear cushion pressure dynamics . . . 26
2.10 Cushion air flow . . . 27
2.10.1 Cushion air gain . . . 28
2.10.2 Cushion air loss, leakage . . . 28
2.11 Cushion forces . . . 32
2.11.1 Non-linear cushion forces . . . 32
2.11.2 Linear cushion forces . . . 34
2.12 Control plant model . . . 34
2.12.1 State space representation . . . 35
2.13 Process plant model . . . 36
2.14 Noise . . . 37

3 Filter and controller design **38**
3.1 Controller 1 - Roll, pitch PD controller . . . 39
3.2 Controller 2 - Heave, roll, pitch damping . . . 41
3.3 Stability of the closed loop system . . . 42
3.3.1 Stability of unperturbed system . . . 42
3.3.2 Robustness of perturbed system . . . 42
3.4 Filters . . . 43
3.4.1 Low-pass filter . . . 44
3.4.2 High-pass filter . . . 45

4 Results **46**
4.1 Numerical simulations . . . 46
4.1.1 Regular waves - roll control . . . 47
4.1.2 Regular waves - pitch control . . . 49
4.1.3 Irregular sea - combined roll and pitch control . . . 52
4.2 Model verification . . . 54
4.2.1 Static heave . . . 55
4.2.2 Static roll . . . 56
4.2.3 Static pitch . . . 57
4.2.4 Valve leakage coefficient, c_n^{vv} . . . 58
4.2.5 Non-solid walls . . . 59
4.3 Scale model experiments . . . 60
4.3.1 Regular waves - 1 meter . . . 61
4.3.2 Regular waves - 2.5 meter . . . 63
4.3.3 Irregular waves . . . 66

5 Discussion **70**
5.1 Model Verification 70
5.1.1 Pressure - heave relation 70
5.1.2 Pressure - roll/pitch relation 71
5.1.3 Cushion air flow 72
5.1.4 Vessel motion in waves 75
5.2 Motion control 76

6 Conclusion **77**

Bibliography **77**

A State space matrices **80**

B Equations for water volume calculations **83**

C Simulink block-diagram of the SES-dynamics **84**

D Calculation of significant heave, roll and pitch motions **86**

E IFAC CAMS 2019 submissions **87**
E.1 Dynamic Modeling and Simulation of aSurface Effect Ship with Four Air Cushions 87
E.2 Roll and Pitch Damping of a Surface EffectShip Utilizing a Four Cushion Solution 95

List of Figures

1.1 Cross section of a SES. Illustration by Umoe Mandal. 1
1.2 Bilge keel in the back. Stabilizing fins in the front 4
1.3 An Umoe Mandal vessel used for crew transport and boarding to an offshore wind turbine. Illustration by Umoe Mandal. 5
1.4 Concept sketch of a ses crew transfer vessel. Illustration by Umoe Mandal. 6
1.5 The cushion separation and numbering as seen from above. 8
1.6 Cross section of a SES from behind. Illustration by Faltinsen [2005] . . . 8
1.7 Model-testing at the NTNU wave basin 9
1.8 Model setup in the NTNU ship towing tank. 10
1.9 Fully open ventilation valve. 11
1.10 Underside of model. Bow skirt (front), transverse separation bag (back). . 13
1.11 The inside of a cushion chamber. 13
1.12 Picture from the second round of testing in the NTNU ocean basin. 14

2.1 Coordinate system $\{\mathrm{b}\}$ is used for the mathematical model. Illustration by Umoe Mandal. 16
2.2 Cross section of a SES. Length of chambers varies. Illustration by Umoe Mandal. 17
2.3 Illustration of planes/areas enclosing an arbitrary cushion chamber. Points of intersection between the planes are noted P_1 through P_4. 19
2.4 Definition of constants x, y and z for an arbitrary cushion chamber. 19
2.5 Possible shape of water area inside a cushion, as seen from above 21
2.6 Cross section underwater area divided into A^{Tra} and A^{Tri} 22
2.7 Leakage area for cushion chamber *i*. Blue area illustrates the water plane, red area shows the corresponding passive leakage area. 30
2.8 Diagram of the SES-sim model structure 36

3.1 Low-pass filter magnitude response as a function of frequency. 44
3.2 High-pass filter magnitude response as a function of frequency. 45

4.1 Normalized roll angle, cushion 1 pressure, cushion 3 pressure and valve opening for regular, bow sea, 2.5 meter $T_p = 7s$ wave. 48
4.2 Normalized pitch angle, cushion 1 pressure, cushion 3 pressure and valve opening for regular, head sea, 2.5 meter $T_p = 7s$ wave. 50
4.3 Roll and pitch damping percentage in regular waves as a function of the wave period. 51
4.4 Time series for normalized roll and pitch angle in irregular beam and head sea. 52
4.5 Roll and pitch damping as a function of wave direction. 53
4.6 Controlled and uncontrolled roll and pitch normalized angle power spectral density. 53
4.7 Position of the ventilation louvers and corresponding bias. 54
4.8 Pressure and corresponding heave for simulation and experiment. 55
4.9 Port and starboard pressure differential and corresponding roll angles for simulation and model testing. 56
4.10 Bow and stern pressure differential and corresponding pitch angles for simulation and model testing. 57
4.11 Average cushion pressure for simulation and experiment with bias $\beta = 75$ and $c_n^{vv} = 0.8$. 58
4.12 Average cushion pressure for simulation and experiment with bias $\beta = 75$ and $c_n^{vv} = 0.4543$. 58
4.13 Vessel dynamics and pressure for regular head sea, $\psi = 180°$. Wave height 1 meter, wave period 5 seconds. 59
4.14 Controlled and uncontrolled pitch and roll for 1 meter, 5 second bow sea ($\psi = 135°$). 61
4.15 Controlled and uncontrolled vessel dynamics and pressure for 1 meter, 5 second bow sea ($\psi = 135°$). 62
4.16 Simulation and experiment pitch and roll with and without cushion control for 2.5 meter, 7 second beam and head sea. 63
4.17 Uncontrolled vessel dynamics and pressure for 2.5 meter, 7 second beam and head sea. 64
4.18 Controlled vessel dynamics and pressure for 2.5 meter, 7 second beam and head sea. 65
4.19 Snapshot of time series for roll and pitch motion in irregular sea for scale model experiments. 67
4.20 Snapshot of time series for roll and pitch motion in irregular sea for numerical simulation. 67
4.21 Radial plot of the significant heave, roll and pitch motion for scale-model experiments. 68
4.22 Power spectral density for roll and pitch motion in irregular sea, for wave basin experiments. 68
4.23 Percentage motion damping, irregular sea, experimental data and numerical simulation. 69

5.1 Fully open ventilation valves. Green colored area displays the area which is registered by AutoCAD® for estimation of effective leakage area. . . . 73

5.2 Inflated transverse cushion dividers at full cushion lift. 75

List of Tables

1.1 Parameter scaling, model : full-scale 12

4.1 Wave description 47
4.2 Normalized peak to peak height of roll angle with control OFF/ON 47
4.3 Wave description 49
4.4 Normalized peak to peak height of pitch angle with control OFF/ON . . . 49
4.5 Wave description 52
4.6 Wave description 61
4.7 Experiment data, regular 1 meter, $T_p = 5s$ waves. Peak to peak angle for roll and pitch with control OFF/ON. 62
4.8 Wave description 63
4.9 Experiment data, regular 2.5 meter, $T_p = 7s$ waves. Peak to peak angle for roll and pitch with control OFF/ON. 64
4.10 Wave description 66
4.11 Modes of control for each heading. 66
4.12 Experiment data, irregular waves. Significant height for heave, and significant angles for roll and pitch, with control OFF/ON. 69

Chapter 1

Introduction

The modern surface effect ship can be described as a hybrid between a catamaran and hovercraft. The hull of a SES is formed like the hull of a catamaran except the bow and stern is sealed off. Figure 1.1 gives an illustration of a SES cross-section as seen from the side. The purpose of this special shape, is to create a volume in which the air will be trapped and the flow of air can be controlled. This volume is referred to as the cushion chamber, where as the air inside the volume is referred to as the air cushion. This cushion allows the vessel to glide on the layer of air, rather than floating due to the displacement of the hull like conventional vessels. The design brings a few benefits such as reduction in drag, improved ride comfort and added flexibility with respect to heave motions.

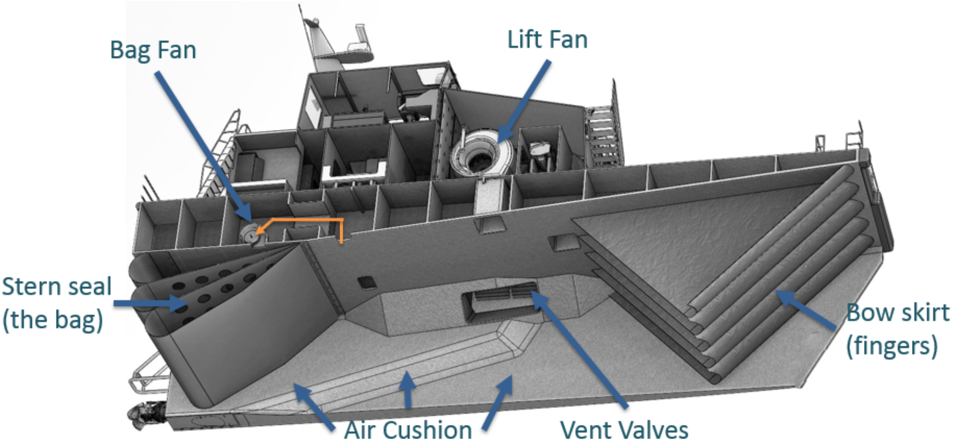

Figure 1.1: Cross section of a SES. Illustration by Umoe Mandal.

The new SES design proposed in this thesis is to further divide the cushion into four air chambers. This introduce the ability to perform roll and pitch control on a SES. Doing so, one can add the pitch and roll control to the list of benefits. Due to the low drag and improved ride comfort of the SES, most SES-vessels are high-speed vessels. The drawback with the cushion solution is that the seals in the front and aft of the vessel suffer a lot of wear and tear and can cause additional drag during transit. Depending on use and the transit velocities of the vessel, these seals will need replacement approximately every 4-5000 engine hours.

This thesis will present modeling and control of a surface effect ship with its air cushion divided into four chambers. The thesis will focus on the mathematical modeling and control but also highlight some of the thoughts and considerations that has gone into the split cushion design. The geometrical, and control system, design is experimentally model-tested at the NTNU Ocean Basin. The data gathered from these tests will be used to investigate the validity of the mathematical model, and will serve as further verification of the multi-cushion SES design. This project is done in collaboration with Umoe Mandal, and is building on some of their previous work. At project start, Umoe Mandal has provided a Simulink model of a vessel operating with a single cushion. The work at hand is to become familiar with their current model, and expand it to incorporate a multi-cushion design. The thesis will also include several improvements and additions to the simulation model. Finally, the model is verified by comparison to the experimental results.

Two papers based on this thesis are also submitted to CAMS19[1], [Haukeland et al. 2019a] and [Haukeland et al. 2019b]. The papers are condensed versions of the main work presented in this thesis. The papers can be found in appendix E.1 and E.2.

1.1 Motivation

The rough seas surrounding offshore structures such as oil platforms, oil-rigs and wind turbines provide a challenge for both crew transport and offshore structure inspections. The use of surface effect ships has emerged as a competitive alternative to helicopter transport, proving high levels of safety, comfort, fuel efficiency and overall reduced cost of offshore logistics, [Mandal 2018]. The main challenge for personnel transfer to an offshore asset is the safety for the crew and ride comfort at high transit speeds. Motion control provides the solution to these challenges, and contributes to an expand of the operational window for marine vessels in harsh weather conditions.

1.2 Existing motion control

The existing systems for motion damping can be divided into passive and active systems. Passive systems aim only to remove energy from the motion, and can in essence be viewed as motion resistance. Active systems add energy to the system in counter phase to the motions, in order to counteract the movement.

---

[1] The 12th IFAC Conference on Control Applications in Marine Systems, Robotics, and Vehicles. KAIST, Daejeon, Korea, 18th to 20th September 2019.

1.2.1 Roll damping

There exist several types of systems for roll damping. The damping of roll movements is highly relevant for all manned vessels traveling in the open sea. Some examples for the most used roll damping systems are:

- **Bilge keel (passive)** is a cheap and effective device for roll damping. The bilge keel normally stretches 25-50% of the length of a ship, with a depth of 1-3% of the ship width, [Pettersen 2007]. Though these dimensions will vary pending on the specific nature of the vessel. Most mono-hulls, regardless of size, are equipped with a form of bilge keel. Other alternatives similar to the bilge keel are fin keels and ballast keels. An illustration of the bilge keel can be seen in Figure 1.2. According to Rawson and Tupper [2001], bilge keels will provide an approximate 35% roll reduction. The drawback of the bilge keel is that it increases the drag resistance of the vessel. Though this is not substantial for large slow-going vessels, for smaller high-speed vessels such as a SES, the drag will be significant and undesired.

- **Stabilizing fins (active)** acts in the same way as the wings of an airplane. While the vessel has a forward momentum, the fins can rotate to vary the generated lift. With proper control, the fins will create a counter moment to the wave induced roll motion. However in low speeds, traditional stabilizing fins have a small damping effect. According to Rawson and Tupper [2001], active fin stabilization can reduce the roll motion as much as 90%.

- **Active and passive roll tanks** are tanks fitted into a vessel for reducing roll movement. Passive roll tanks, such as u-tube tanks and free surface tanks work by letting water flow from one side of the ship to the other as the vessel rolls. By careful design, the roll moment induced by the water flow can be in counter phase to the roll motion of the vessel, and will generate a damping moment. Alternatively, it can be designed to pass water at a frequency lower than the vessels natural rolling frequency to damp out that resonance. Roll tanks are somewhat space consuming and are generally only used for larger vessels.

- **Massive gyroscope (active)** provides a stabilizing moment via production of torque. Gyroscope stabilizers work for stationary vessels, but can only produce a limited amount of stabilizing moment. They are also quite heavy and costly in comparison to most of the options listed above.

1.2.2 Pitch damping

Systems for pitch damping are much less widespread than for roll. This is because pitch motions are generally harder to control [Smith and Thomas 1990]. The pitch motions are exited over a large range of frequencies, and as the vessel is much longer than it is wide, pitch motion generate a very large moment, which are therefore harder to counteract. However, some systems are designed for pitch control such as:

- **Anti-pitching fins (passive)** have the same mechanism for generating force as the anti-rolling fins. Instead of being placed around the vessel center of gravity, the

Figure 1.2: Bilge keel in the back. Stabilizing fins in the front

fins are placed at the aft or rear end of the ship. Therefore, when the fins generate lift, they also induce a pitch moment. According to Reguram et al. [2016], the anti-pitching fins can contribute to a 58-80% reduction in pitch motion. The drawback of the anti-pitching fins is that they create an increased drag, and like the rolling fins, they require the vessel to be moving in order to generate any lift.

- **Anti-pitching tanks (active)** work by the same principle as the active rolling tanks. They are not nearly as widely used as the anti-rolling tanks, but companies such as Marine Roll & Pitch Control, [MRPC 2019], do provide a solution for anti-pitching tanks. The major drawback of such tanks is that the large moment generated by the pitching motion require large amounts of water, transferred a long distance from aft to bow to counteract the motion. This is both energy consuming, space consuming and can be technically challenging to implement.

1.3 Existing SES cushion control systems

In recent years much has happened on motion control for the surface effect ship. Vamråk et al. [2016] proposed a method for lateral control. Auestad et al. [2014] proposed a system for stationary motion compensation. And Tønnessen et al. [2018] investigated the effect of roll damping on a SES with a lateral split cushion. Perhaps the two most important systems for SES cushion control that are the Ride Control System (RCS) and the Boarding Control System (BCS). Both of these systems are currently in use on several full-scale vessels.

- **The Ride Control System** was first featured in Kaplan and Davis [1978], and has since been further developed by Sørensen and Egeland [1995]. The purpose of the system is to create a more smooth ride at high transit velocities. The system provides active damping of vertical motions by manipulating and reducing the cushion pressure fluctuations caused by the encountered sea-wave, non-spatial and spatial varying cushion pressure resonances.

- **The Boarding Control System** is presented in Auestad et al. [2015]. The main use of the boarding control system is to reduce the movements of the vessel bow, so that it is possible to secure safer transfer from the ship to offshore structures, specifically, offshore wind-turbines. See Figure 1.3. The boarding control system relies on manipulating the pressure of the single cushion to counteract wave induce vertical motions at the location of an accelerometer.

These examples of manipulating the cushion pressure as a way of controlling the vessel motions have proven to be of essence in the day-to-day operation. As such, they provide a good basis and motivation for further development within motion control on a SES.

Figure 1.3: An Umoe Mandal vessel used for crew transport and boarding to an offshore wind turbine. Illustration by Umoe Mandal.

Figure 1.4: Concept sketch of a ses crew transfer vessel. Illustration by Umoe Mandal.

1.4 The vessel

This section will cover most of the relevant descriptions and data for the vessel in question. Physical implementations for many of the things discussed and described here can be seen in the next section 1.5. The hypothetical full-scale vessel that will be discussed in this thesis is a 38m long, 200-ton vessel shown in Figure 1.4. The simulation performed in this thesis does not represent such a full-scale commercial vessel, but is instead a generic SES, inspired by the design shown in Figure 1.4. The simulation data generated in this thesis will therefore not represent the performance of any Umoe Mandal vessels.

1.4.1 Cushions

The purpose of the thesis is to investigate the properties and possible advantages and disadvantages of a four-chamber solution. As the starting point is a one-chamber solution, the first task is to divide the cushion chamber into four separate sections. These four cushion-chambers are separated longitudinally and laterally to provide both roll and pitch control.

Mono cushion chamber

The design at project start consists of a single cushion. This cushion is contained within the side-hull of the vessel, as well as the front fingers of and the aft bag. This is illustrated in Figure 1.1. The fingers consist of a bendable reinforced rubber material that will move with the water surface and elevation of the craft. This ensures minimal air-leakage from the cushion, while the vessel can operate at semi-cushioned mode, without the bow acting as a plow in the water. The aft separation of the cushion chamber is called the bag. As the name suggests, this is an inflated bag, holding a slightly higher pressure than that of the cushion itself. This ensures minimal air leakage, while also allowing the bag move in tact with the motion of the water surface to ensure low drag.

Multi cushion division

The multiple cushion solution is simply an extension of the single-cushion solution. The cushion volume encasement as expressed for the single cushion solution remains unchanged, but is additionally divided into four chambers. As the vessel needs to maintain its high speed properties, the cushion dividers must be created in a way that does not obstruct or cause unnecessary drag during the high speed modes for the vessel. A couple of different solutions to this problem have been discussed. Completely solid, retractable, walls would be ideal with regards to inter-cushion leakage. However, due to structural complications, this idea has been discarded. The solution the the cushion division problem, is the combination of a solid wall and pressurized, inflatable bags. The solid wall is placed longitudinally, stretching from aft to bow, covering the height from the top of the cushion chamber, also known as the wetdeck, and approximately half way down towards the water surface. The remaining distance is separated by an inflatable cushion. Figures 1.10 and 1.10 illustrate this implementation for the scale-model.

The lateral dividers consist solely of inflatable bags. These bags are pressurized with a substantially higher pressure than the pressure in the surrounding chambers to make the separators stiff enough so that the cushion pressure does not equalize between the chambers. The height of the lateral dividers has been a discussion These are perpendicular to the direction of movement and will cause substantial drag if they come in contact with the water during transit. Ultimately, the decision fell on making them stretch all the way from the wetdeck, to the bottom of the cushion, also known as the baseline. The reasoning behind this decision is that a shorter separation wall will possibly cause more air leakage from one chamber to another. This is further addressed in section 2.10.2.

The placement of the longitudinally divider is naturally centered at the middle of the vessel. The lateral cushion dividers are placed at the position where the single-cushion center of pressure is when the cushions hold the equilibrium pressure of p_0. Because of this, there is a small distance from the center of gravity to the lateral chamber dividers. This means that large pitch angles theoretically can contribute to leakage between aft and stern cushions. Leakage between these cushions would mitigate any pitch stabilization originating from a pressure differential between the front and aft cushions. This would in turn increase the pitch angle, and thus further increase the cushion leakage. This is yet another reason for the lateral cushion dividers to cover the entire height from wetdeck to baseline. For the remainder of this thesis, the separated cushions will be numbered and referred to as illustrated in Figure 1.5.

Figure 1.5: The cushion separation and numbering as seen from above.

1.4.2 Cushion air flow

The air flow in and out of the cushions are controlled via lift fans and ventilation valves. Each cushion has its own lift fan and ventilation valve. Furthermore, as can be seen in Figure 1.1, an additional fan is used to inflate the aft bag. For the four chamber solution, yet one more fan will be used to inflate the bags separating the cushion chambers. While the lift fans take in air from the atmosphere, the fan inflating the rear seal, as well as the fan inflating the separation walls will use pressurized air from the cushions. This will reduce the differential pressure, so that smaller fans can be applied. Figure 1.6 illustrates the cross section of a surface effect ship as seen from behind. Note that the water column inside the cushions is lower than that on the outside due to the cushion pressure. This will be further addressed in chapter 2.

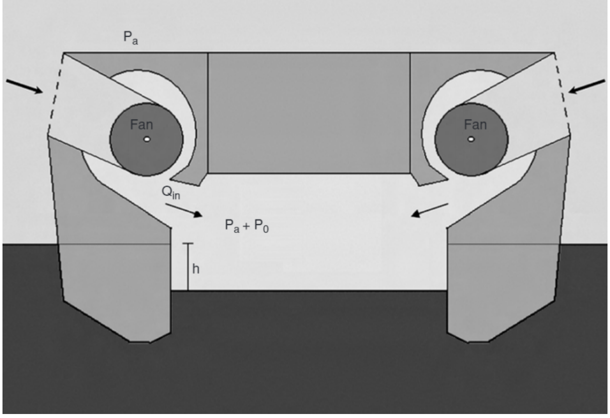

Figure 1.6: Cross section of a SES from behind. Illustration by Faltinsen [2005]

1.5 The model-scaled vessel

This section contains descriptions and illustrations of the scale model which used for model testing in the NTNU wave basin, see Figure 1.7.

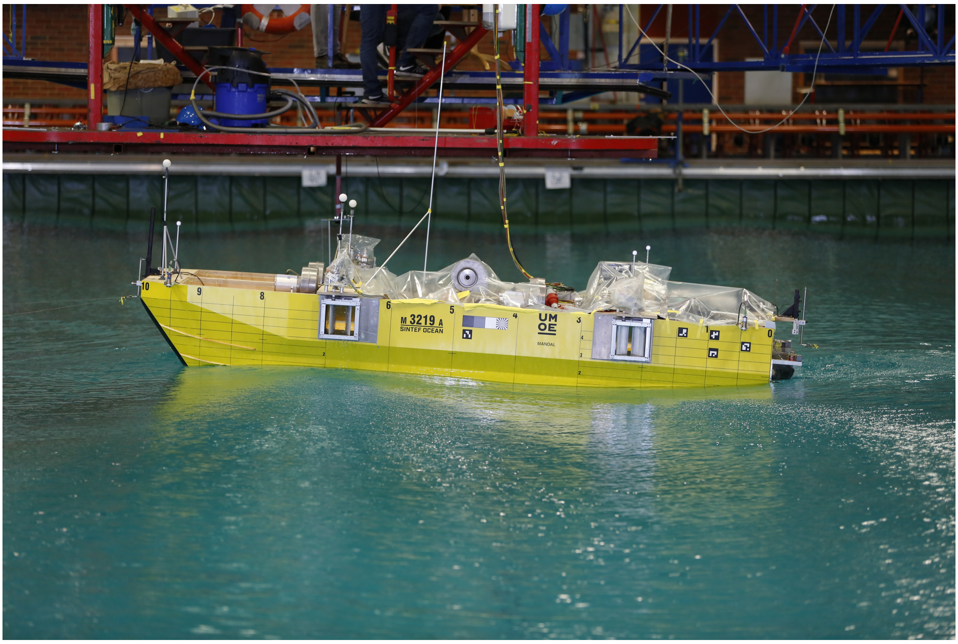

Figure 1.7: Model-testing at the NTNU wave basin

1.5.1 Instrumentation

Actuation

The actuation and control of roll, pitch and heave motions of the model is through the use of lift fans and the ventilation valves. These actuators respectively provide airflow, into and out from, the air cushions. All actuators dimensions and properties are carefully scaled so that they represent the full-scale design.

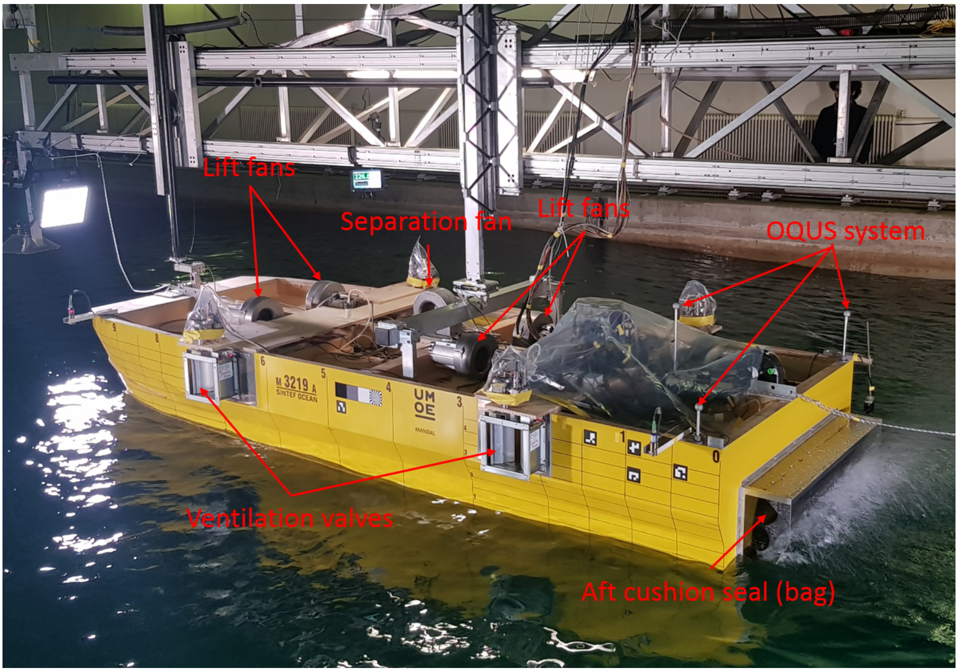

Figure 1.8: Model setup in the NTNU ship towing tank.

- **Lift fans:** Four lift fans are mounted to the top of the model, one for each cushion. The lift fans run at a fixed speed. Having a variable speed setup is not favorable since the full-scale design is not suited for rapid speed variations on such short periods as the wave period (4-10s).

- **Separation and bag fan:** For the model test, the separation fan, which is responsible for inflating the transverse and longitudinal separation bags, does not receive air from the cushion chambers. Again, this is to reduce the complexity of the model, and number of moving parts. Unlike the separation fan, the bag fan, which is used to inflate the aft cushion seal, does gather air from the rear cushion chambers. As with the lift fans, both of these fans are fixed to an appropriate flow rate.

- **Ventilation louvers:** The air leakage through the ventilation valves are actuated by controllable louvers. The actuation of the ventilation valve louvers is designed to be very fast, so that no notable delay will be introduced into the control. Unlike the fans, the varying louver positions will constitute the mode of control for the model, meaning that their position is in no way fixed. The picture in Figure 1.9 shows one of the model ventilation valve with its louvers fully opened.

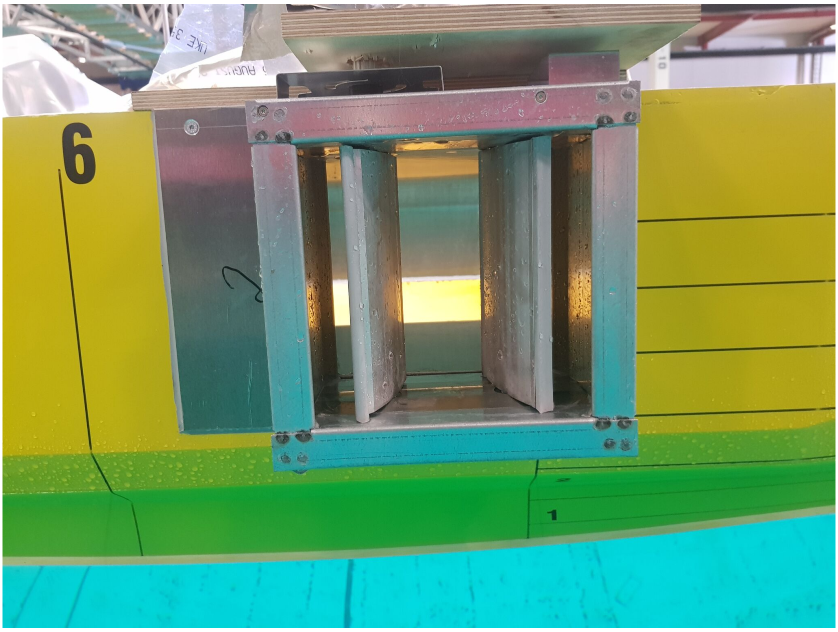

Figure 1.9: Fully open ventilation valve.

Data capture

The model data is registered and captured by several different instruments, many of which create redundancies to ensure that no data is lost. Most important for our system is

- **Accelerometers** register the accelerations in surge, sway and heave. They provide the base for calculating the heave velocity which are used for control feedback during heave control.
- **The gyroscopes** register the angular velocity for roll, pitch and yaw. This data is the base for calculating the roll and pitch angles. The gyroscope data will also be used as the control feedback for roll and pitch control.
- **The OQUS system** is a camera system used to capture position and orientation in 6 degrees of freedom. Several cameras recognize and track the relative movements of several silver spheres, which are highlighted in the picture above in Figure 1.8. By combining the tracked paths of these spheres, the position and angles of the vessel can be calculated. The OQUS system is used when evaluating vessel motions.
- **Pressure sensors** are used to measure the pressure of both the insides the cushions, and inside the different bags used for sealing the cushion chambers.
- **The potentiometer** captures the actual louver position of each of the ventilation valves.

1.5.2 Scaling

As the model is designed by Umoe Mandal and manifactured by Sintef Ocean, model-scaling will not be discussed in depth here. However it is important to note that the dimensions of the vessel and the model is scaled by 9:1. In other words, the length of the model is 4.22 meters, while the full-scale vessel is 38 meters. The scaling of time for the model-scale against the full-scale is given as $\sqrt{9} : 1$. Meaning that time runs three times faster in the model basin. Table 1.1 lists the scaling factors for some of the most relevant parameters. The last three scaling factors in the table are especially important with respect to the control and signal filtering for the scaled model.

Table 1.1: Parameter scaling, model : full-scale

	Unit	Scaling factor
Length	[m]	1 : 9
Area	[m^2]	$1 : 9^2$
Pressure	[Pa]	$1 : 9^2$
Force	[N]	$1 : 9^3$
Moment	[Nm]	$1 : 9^4$
Weight	[Kg]	$1 : 9^3$
Time	[s]	3 : 1
Heave rate, $\dot{\eta}_3$	[m/s]	1 : 3
Pitch angle, η_5	[deg]	1 : 1
Pitch rate, $\dot{\eta}_5$	[deg/s]	3 : 1

1.5.3 Cushion seals and separation walls

As briefly mentioned in sections 1.4.1 and 2.10.2, the cushion chambers are divided by the use of inflatable bags. Figure 1.10 is a picture taken from the underside of the model during assembly. The picture displays how the separation walls look when they are pressurized.

The picture in Figure 1.11 is taken from inside one of the cushion chambers, and shows the center separation bag connected to the center separation wall, as explained in section 1.4.1.

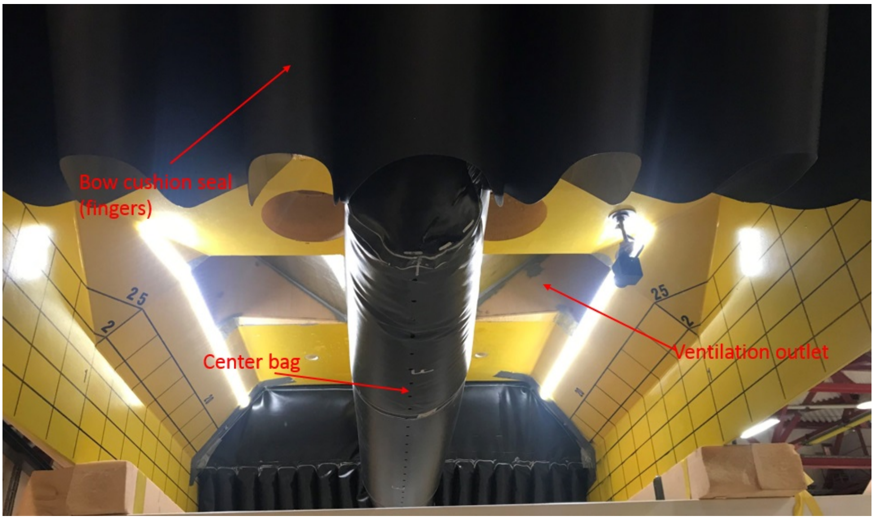

Figure 1.10: Underside of model. Bow skirt (front), transverse separation bag (back).

Figure 1.11: The inside of a cushion chamber.

1.6 Model testing

The model testing takes place in two stages.

Test round 1 - February 2019

The first round of model testing takes place in February 2019 in the NTNU ship towing tank. The goal for this round of testing is to register pitch control during transit. For this thesis we are focused on control at zero or low velocities. Therefore only a small amount of data from the first round of testing is evaluated in this thesis.

Test round 2 - May 2019

The second round of model testing took place at the NTNU ocean basin in late May 2019. The goal here was to evaluate and verify the efficiency of the four cushion solution while performing roll, pitch and heave damping. Unfortunately these test are completed quite close to the deadline for this project, and as such, only a limited time can be devoted to post-testing data analysis. Figure 1.12 is a picture taken of the model during the second round of testing in the NTNU ocean basin.

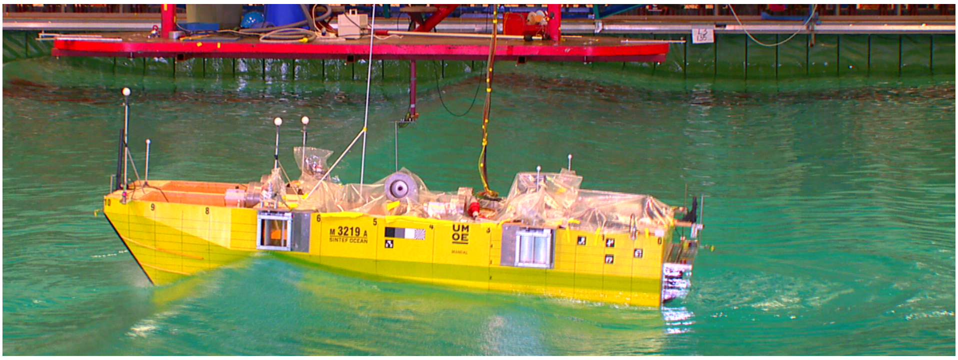

Figure 1.12: Picture from the second round of testing in the NTNU ocean basin.

1.7 Presentations of results

At the request of Umoe Mandal, and to ensure the preservation of intellectual property rights, all results regarding metrics such as pressures, volume flow, distances and angles will be normalized. This entails that the y-axis on all graphs will be set at a value of approximately -1 to 1 instead of the actual values. Though the scaling for each metrics is different, the scale will be consistent through the paper, so that different graphs and results may be compared to each other. Furthermore, all pressures are scaled following the same constant, such that the different cushion pressures can be compared. Roll and pitch angles will be scaled after different constants and are not 1 to 1.

Chapter 2

Mathematical model

The purpose of the mathematical model is to model the physical interaction between the vessel and its relevant surroundings as accurately as possible. This is achieved by expressing the known physical interactions through equations. Upon completion, the model is simulated by calculating the equations in iterations. For the mathematical model to be a good approximation of the real system, the provided equations must represent the physical system as closely as possible. An effort has been made to make the mathematical model presented below as general as possible with respect to the cushions. In other words, ideally, the model can be applied to vessels using either one, two or four cushions by only making minor input changes in the vessel specifications. Some aspects of this flexibility in the model is incomplete and untested though most equations given below will be generalized.

The mathematical model that will be developed in this chapter, will be implemented in the programs Matlab and Simulink. These programs will also be used for simulations of the model. A layout of the Simulink block diagram covering the vessel dynamics can be seen in appendix C, and a simplified block diagram of the system structure can be seen in Figure 2.8. For the equations in this chapter, unless it is specified otherwise, subscript i will refer to cushion numbering. Here $i = \{1, 2, 3, 4\}$ refers to the cushions following the cushion numbering illustration in Figure 1.5.

2.1 Contribution of the thesis

This thesis contributes with new mathematical modelling of a SES and expanding the current single cushion model provided by Umoe Mandal into a four cushion model. In addition to this, the sub-chapters 2.3, 2.4, 2.5 and 2.6 are the original work of this thesis. The air cushion flow in chapter 2.10 has also been further developed to include inter-cushion air leakage, leakage as a function of varying sea elevation and modified leakage to account for non-linear compressible air flow. The subsequent sub-chapters, which deals with process- and control-plant modelling, will also include these contributions.

2.2 Equations of motion

The motions of the vessel are calculated using newtons second law, $F = m \times a$. In the Matlab/Simulink model, the conversion from forces acting on the ship to the corresponding motions are mostly handled by the Marine Systems Simulator (MSS) by Fossen and Perez [2004], with some alterations made by Umoe Mandal. Therefore, the mathematical model that is created here, will only have to compute the forces acting on the vessel which are related to the cushions. The coordinate system for the vessel is illustrated in Figure 2.1. In the implementation of the mathematical model, all three coordinate systems are utilized. For this thesis, only the body fixed frame, {b} will be used.

The origin of the coordinate frames, O_b and O_n, are located on the center-line, on the water surface, and on the longitudinal center of gravity.

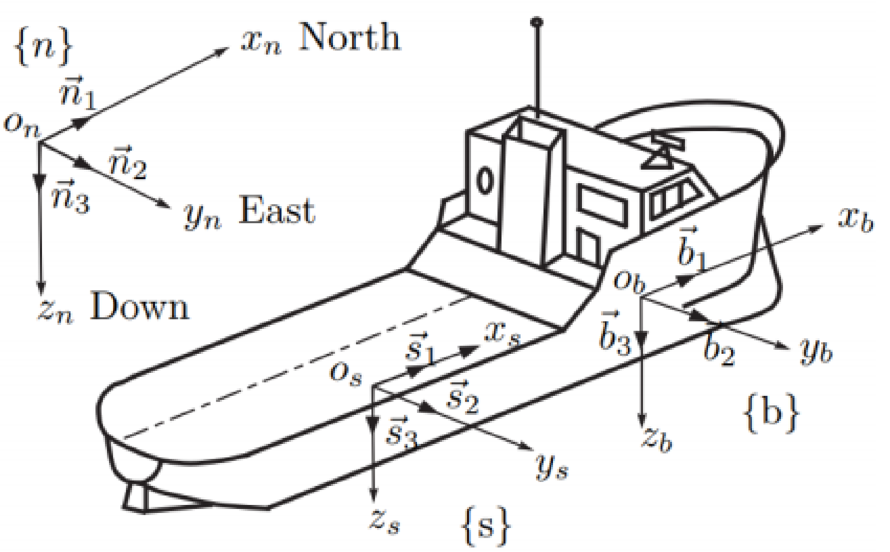

Figure 2.1: Coordinate system {b} is used for the mathematical model. Illustration by Umoe Mandal.

Considering 6 degrees of freedom (DOF) and non-linear motion, the equations of motion using a body-fixed coordinate system becomes as stated in equation (2.1). The equation is collected from Sørensen [2012].

$$\boldsymbol{M}\dot{\boldsymbol{\nu}} + \boldsymbol{C}_{RB}(\boldsymbol{\nu})\boldsymbol{\nu} + \boldsymbol{C}_A(\boldsymbol{\nu}_r)\boldsymbol{\nu}_r + \boldsymbol{D}(\boldsymbol{\nu}_r) + \boldsymbol{G}(\boldsymbol{\eta}) = \Sigma\boldsymbol{\tau} \tag{2.1}$$

Here, $\dot{\boldsymbol{\eta}} = \boldsymbol{\nu}$, where $\boldsymbol{\nu}$ denotes the velocities of the vessel and thus $\boldsymbol{\eta}$ represents the position and orientation of the vessel. Since we consider motion in six degrees of freedom, $\boldsymbol{\eta}$ is a matrix with six entries. The first three entries of $\boldsymbol{\eta}$ are translations along the x, y an z-axes, which are referred to as surge, sway and heave, respectively. The last three entries of $\boldsymbol{\eta}$ are rotations around the x, y and z-axes, and are referred to as roll, pitch and yaw. Combined, these 6 translations and rotations are denoted as η_1 through η_6, respectively. Furthermore, the term $\boldsymbol{M}\dot{\boldsymbol{\nu}}$ expresses the generalized inertial forces. The term $\boldsymbol{C}_{RB}(\boldsymbol{\nu})\boldsymbol{\nu} + \boldsymbol{C}_A(\boldsymbol{\nu}_r)\boldsymbol{\nu}_r$ expresses the Coriolis and centripetal forces of the vessel. These forces can be disregarded as they are not relevant to the case of our vessel which will be regarded as stationary for the scope of this thesis. $\boldsymbol{D}(\boldsymbol{\nu}_r)$ and $\boldsymbol{G}(\boldsymbol{\eta})$ are the generalized damping forces and the generalized restoring forces. The excitation forces acting on the vessel are noted as $\boldsymbol{\tau}$. For this model, $\boldsymbol{\tau}_c$ will signify the force originating from the cushions. $\boldsymbol{\tau}_e$ denote the excitation forces, which for this project will be synonymous with the wave excitation forces.

2.3 Variable cushion length

In the simulation model provided by Umoe Mandal, the cushion chambers are modeled as a square right-angled volumes. However, due to the angle of the front skirt and the aft bag, this is not completely accurate. Figure 2.2 attempts to illustrate how the length of each chamber will vary with the water-level inside the chamber, and hence with the heave, pitch and roll of the vessel. The red line represents an imagined chamber separation wall, while the green and blue lines illustrate the different chamber lengths when the water-level inside the cushion reaches the wet-deck, and when the cushion chamber is completely free of water. As the length of the cushion changes, the area of pressure against the water changes. The pressure force of each cushion can be as described in equation (2.2).

$$F_i = A_{c_i} p_{u_i} \tag{2.2}$$

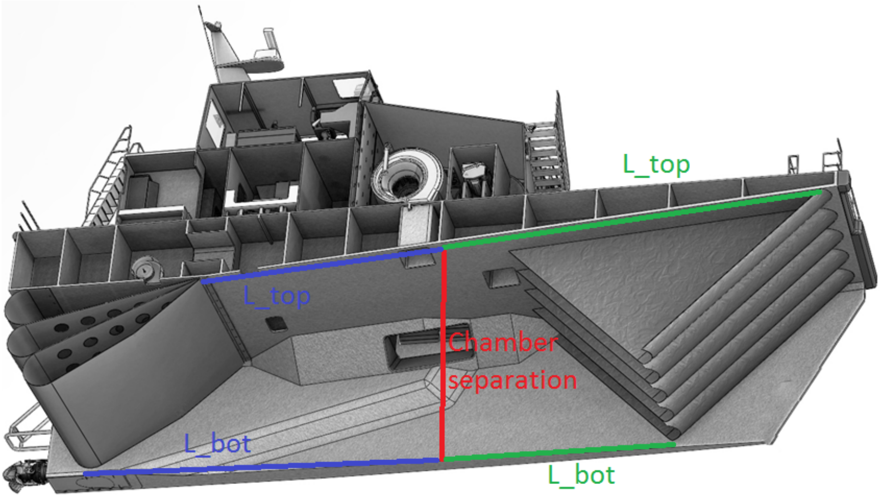

Figure 2.2: Cross section of a SES. Length of chambers varies. Illustration by Umoe Mandal.

As stated in the introduction to the mathematical model, i denotes chambers 1 through 4 in equation (2.2). The cushion force from each chamber is dependent on the area of the water inside the cushion, and thus it will change as the length of the cushion changes. Furthermore, the center of pressure in the ship longitudinal direction, noted x_{cp}, will scale with the length of the cushion chamber. From equation (2.3), it can be seen that the moment in pitch acting on the vessel will have a non-linear dependence on the length of the cushion, due to both $A_c(i)$ and $x_{cp}(i)$ depending on the changing cushion length.

$$F_5(i) = x_{cp}(i)A_c(i)P_c(i) \tag{2.3}$$

For previous models without the lateral cushion chamber divider, modeling the cushion as a square chamber might have been an adequate approximation. However, when dividing the chamber laterally, the change in the cushion pressure surface and center of pressure will especially affect the pitch control of the vessel. For these reasons, it has been opted to include the variable cushion length in this model of the vessel dynamics.

2.4 Cushion geometry

Each cushion chamber is modeled as a volume enclosed by 5 planes. Four of the planes represent the surrounding hull and cushion walls, while the fifth plane represents the water surface. The five planes enclosing an arbitrary chamber are illustrated in Figure 2.3. Here, the areas A_1 through A_4 can be seen as the hull and cushion walls, while area A_5 illustrates the water plane. In order to generalize the equations to be applicable to both one and four cushions, both the aft and forward cushion walls must be modeled as non-vertical planes. That is, the areas A_3 and A_4 must be able to represent the aft bag and bow fingers, respectively. The fifth plane, representing the water surface, will be heaved and tilted corresponding to the heave, roll-angle and pitch-angle of the craft. The mathematical expression for each of these planes are shown in equations (2.4) through (2.8).

$$A_1; \quad y = y_1 \tag{2.4}$$

$$A_2; \quad y = y_2 \tag{2.5}$$

$$A_3; \quad x = x_2 + \frac{x_1 - x_2}{z_1 - z_2}(z - z_1) \tag{2.6}$$

$$A_4; \quad x = x_4 + \frac{x_3 - x_4}{z_1 - z_2}(z - z_1) \tag{2.7}$$

$$A_5; \quad z = -\eta_3 - y\sin(\eta_4) + x\sin(\eta_5) - (z_2 + h_0) \tag{2.8}$$

The notations used on x, y and z are visualized in Figure 2.4. The term h_0 in equation (2.8) is added to account for the water displaced in the cushion due to the cushion pressure. This water displacement effect is better illustrated in Figure 1.6, and can be expressed mathematically as given in equation (2.9). The heave level of the vessel should be be relative to the initial heave position, given at initial cushion pressure p_0. Thus h_{init} is added to offset the heave position from the baseline of the vessel to the initial heave position, relative to the vessel center of gravity. The term h_{init} can then be expressed as $h_{init} = CoG_z - T$, where T is the draught of the vessel at p_0, and CoG_z is the height of the center of gravity for the vessel. The initial pressure p_0 is further addressed and explained in chapter 2.8.

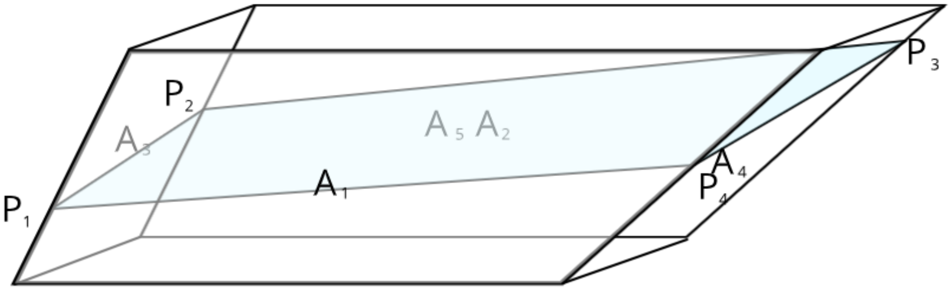

Figure 2.3: Illustration of planes/areas enclosing an arbitrary cushion chamber. Points of intersection between the planes are noted P_1 through P_4.

$$h_{0i} = \frac{p_{0i}}{g\rho_w} \tag{2.9}$$

In the equation above, p_{0i} is the initial pressure in cushion i. Furthermore, ρ_w is the density of the saltwater, and g is the gravitational constant.
The points of intersection, where three of the planes enclosing the chamber meet, are calculated as points P_1, P_2, P_3 and P_4. The placements of these points are illustrated in Figure 2.3.

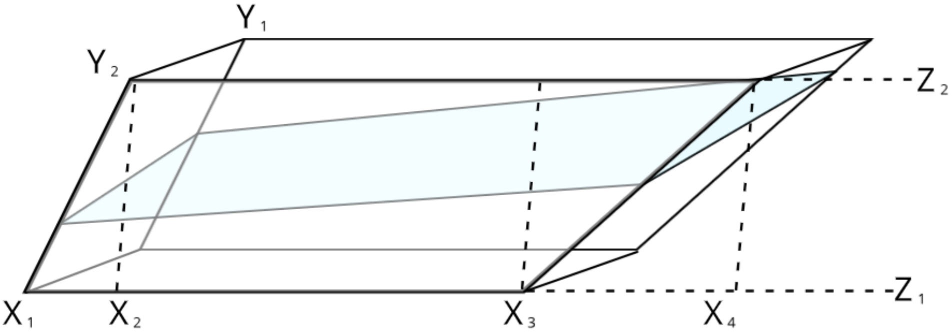

Figure 2.4: Definition of constants x, y and z for an arbitrary cushion chamber.

2.5 Pressure area

The area of the water surface in each chamber is calculated by dividing the chamber into two or four triangles, by drawing a line between points P_2 and P_4. Figure 2.5 helps to illustrate this, and shows how the water area can be divided. The height of each triangle is found through equations (2.10) to (2.14). The surface area in each chamber then becomes the combined area of the triangles.

$$d_i = \frac{P_1 - P_4}{||P_1 - P_4||} \tag{2.10}$$

$$v = P_2 - P_4 \tag{2.11}$$

$$t = v \cdot d \tag{2.12}$$

$$P_p = P_4 + t \times d \tag{2.13}$$

$$h = ||P_p - P_2|| \tag{2.14}$$

Here the d becomes the direction vector of the line from P_4 to P_1. v is the vector from P_4 to P_2. Calculating the dot product of this vector and the directional vector, gives the distance t, between P_4 and the projection of P_2 on the line from P_4 to P_1. Then P_p is the imagined point on the line P_4 to P_1, where a perpendicular line on P_4P_1 will go through point P_2. Finally the distance from the imagined point P_p to P_2, and thus the height of the triangle, is the variable h.

Due to the roll and yaw angles of the vessel, the water area can be decomposed into three areas, A_x, projected onto the y-z-plane, A_y, projected onto x-z-plane and A_z, projected onto the the x-y-plane. Each of these areas will contribute to pressure forces acting on the vessel. A_x and A_z are calculated following equation (2.15) and (2.16). A_y can be calculated using equation (2.22), solving this equation becomes a bit more convoluted, and is further explained in chapter 2.6.

$$A_x = (P_{1y} - P_{2y})(z_1 - \frac{1}{2}(P_{1z} + P_{2z})) - (P_{4y} - P_{3y})(z_1 - \frac{1}{2}(P_{1z} + P_{2z})) \tag{2.15}$$

$$A_z = (\frac{1}{2}(P_{4x} + P_{3x}) - \frac{1}{2}(P_{1x} + P_{2x}))(P_{1y} - P_{2y}) \tag{2.16}$$

In the equations above, the subscripts such as P_{1x} and P_{2y} denote the x-coordinates of point 1, and the y-coordinates of point 2, respectively.

2.5.1 Center of pressure

The water area inside the cushion can be viewed as illustrated in Figure 2.5. The center of pressure in x-direction, $x_{cp}(t)$, is calculated as

$$x_{cp}(t) = \sum_{i=1}^{4} \frac{A_{c_i}(t)(\frac{1}{3}x_{r_i}(t) + x_{cg_i}(t))}{A_t(t)}. \tag{2.17}$$

Here A_i is the area of the triangle shown in Figure 2.5, and $x_{cg_i}(t)$ is the corresponding distance from the center of gravity to the right angle of the triangle. $x_{r_i}(t)$ is the distance from the right angle of the triangle to the corner of each triangle. Because of the angle of the front skirt and aft bag, roll angles will also change the center of pressure in the y-direction, $y_{cp}(t)$. This center of pressure is calculated the same manner as $x_{cp}(t)$, so that $y_{cp}(t)$ can be expressed as

$$y_{cp}(t) = \sum_{i=1}^{4} \frac{A_{c_i}(t)(\frac{1}{3}y_{r_i}(t) + y_{cg_i}(t))}{A_t(t)}. \tag{2.18}$$

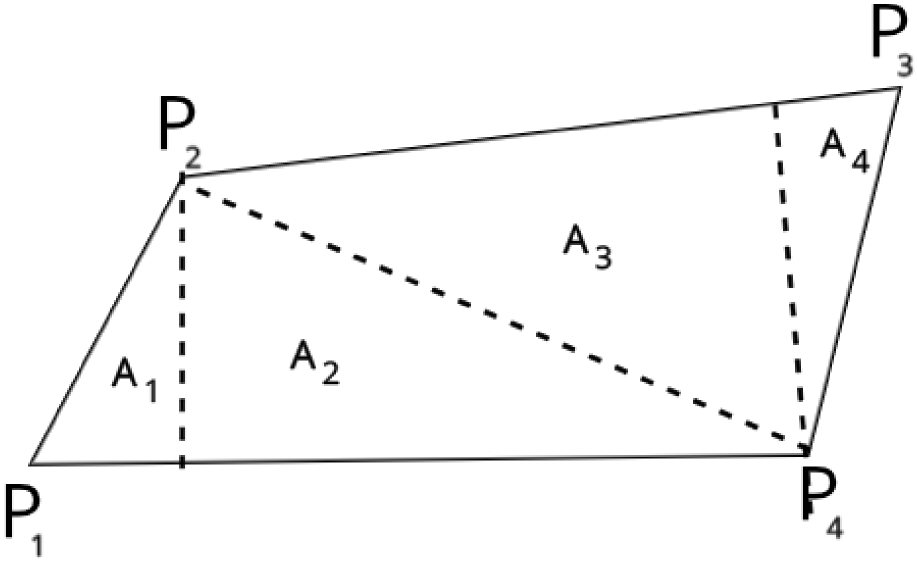

Figure 2.5: Possible shape of water area inside a cushion, as seen from above

2.6 Cushion volume

The traditional way of modelling the air cushion volume (Sørensen 1993) is given according to

$$V(t) = -V_0(t) + A_c(t)(-\eta_3(t) - y_{cp}(t)\eta_4(t) + x_{cp}(t)\eta_5(t)). \tag{2.19}$$

Here V_{0_i} is the chamber volume occupied by waves entering or exiting the cushion chamber. A_{c_i} is the surface area of water inside the cushion, and $\eta_3(t)$, $\eta_4(t)$ and $\eta_5(t)$ are the heave, roll and pitch of the vessel, respectively. Due to the change in the geometry of the cushion chamber, equation (2.19) can no longer be used to calculate the new cushion volumes. With the new cushion geometry, the total volume of each of the cushions can be seen as a 3-dimensional trapezoid. As only the front and aft walls of the chamber are dependent on the spatial coordinates, and their dependence is linear, the total volume of the cushion can be calculated as the average of the top area and the bottom area, multiplied with the height of the cushion. This is formulated in in equation (2.20).

$$V_{T_i} = \frac{(A_T + A_B)}{2}(z_1 - z_2) \tag{2.20}$$

The volume of the water inside a cushion can be calculated as

$$V_{w_i}(t) = \int_{y_0}^{y_1} A_y(y)dy. \tag{2.21}$$

Here $A_y(y)$ represents the cross section area of the cushion in the x-z-plane that is under water, moving from y_1 to y_2. As y becomes a function of time, so does $V_{w_i}(t)$. To simplify and shorten the equations a little, $y(t)$ will be shortened to only y for the remainder of this chapter. $A_y(y)$ can be split into two areas, a trapezoid, and a triangle. Figure 2.6 illustrates these areas. The total area $A_y(y)$ can be expressed as shown in equation (2.22).

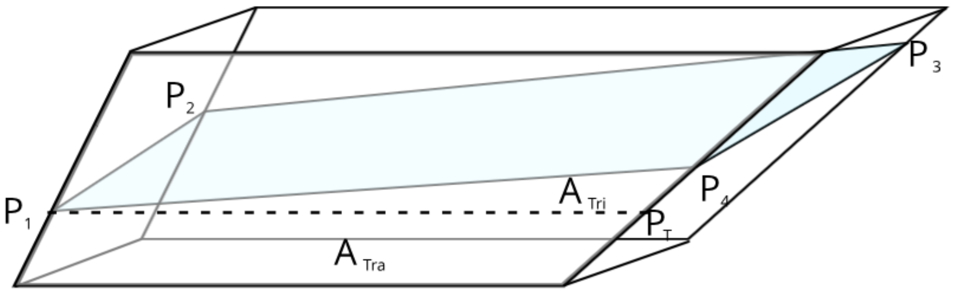

Figure 2.6: Cross section underwater area divided into A^{Tra} and A^{Tri}

$$A_{y_i}(y) = \bar{L}_i^{Tra}(y)H_i^{Tra}(y) + \frac{1}{2}L_i^{Tri}(y)H_i^{Tri}(y) \tag{2.22}$$

In equation (2.22), $\bar{L}_i^{Tra}(y)$ is the average length of the trapezoid, and H_i^{Tra} is the height. These both vary with y as the length and height of the trapezoid varies with the distance from point P_4 to P_3. Hence $\bar{L}_i^{Tra}(y)$ can be described as in equation (2.23) and H_i^{Tra} can be described as in equation (2.24). Furthermore, $L_i^{Tri}(y)$ and $H_i^{Tri}(y)$ is the length and height of the triangle, respectively. These are also functions of y as the height and length of the triangle vary with the changing position from P_1 to P_2 and P_4 to P_3. As all the functions of y here are linear, the water volume inside the cushion can be analytically computed and solved as a 3'rd degree equation. This will contribute to reduce the simulation time relative to a numerical approximation.

$$\bar{L}_i^{Tra}(y) = A_{x_i}^{Tra} + B_{x_i}^{Tra}y \tag{2.23}$$

$$H_i^{Tra}(y) = A_{z_i}^{Tra} + B_{z_i}^{Tra}y \tag{2.24}$$

$$L_i^{Tri}(y) = A_{x_i}^{Tri} + B_{x_i}^{Tri} y \tag{2.25}$$

$$H_i^{Tri}(y) = A_{z_i}^{Tri} + B_{z_i}^{Tri} y \tag{2.26}$$

The equations for the constants A and B used in equations (2.23) to (2.26) are too long to write here, and can be seen in Appendix B in equations (A.1) to (A.8). Following the equations stated above, the water volume inside the cushions can be written as

$$V_{w_i} = \int_{y_0}^{y_1} (A_i + B_i y + C_i y^2) dy, \tag{2.27}$$

where the constants A_i, B_i and C_i are calculated following equations (2.28) through (2.30).

$$A_i = A_{x_i}^{Tra} A_{z_i}^{Tra} + \frac{1}{2} A_{x_i}^{Tri} A_{z_i}^{Tri} \tag{2.28}$$

$$B_i = A_{x_i}^{Tra} B_{z_i}^{Tra} + A_{z_i}^{Tra} B_{x_i}^{Tra} + \frac{1}{2}(A_{x_i}^{Tri} B_{z_i}^{Tri} + A_{z_i}^{Tri} B_{x_i}^{Tri}) \tag{2.29}$$

$$C_i = B_{x_i}^{Tra} B_{z_i}^{Tra} + \frac{1}{2} B_{x_i}^{Tri} B_{z_i}^{Tri} \tag{2.30}$$

The cushion volume change, $\dot{V}_{c_i}$, can be calculated by differentiating the formula for the cushion volume given in equation (2.19). The equation then becomes

$$\dot{V}_{c_i}(t) = A_{c_i}(t)(-\nu_3(t) - y_{cp_i}(t)\nu_4(t) + x_{cp_i}(t)\nu_5(t)) - \dot{V}_{0_i}(t), \tag{2.31}$$

where $\dot{V}_{0_i}(t)$ is the wave volume pumping. The wave volume pumping is further explained in chapter 2.8. Furthermore, $\nu_3(t)$ is the heave velocity, while $\nu_4(t)$ and $\nu_5(t)$ is the roll and pitch-rate. Note that integrating the $\dot{V}_{c_i}(t)$ from the equation given in (2.31) will lead to a minor error, as the area, $A_{c_i}(t)$, is not constant over the distance of $\nu(t)\Delta t$. Since the simulations will run at 200Hz, the error that $A_{c_i}(t)$ introduces is very small. Also, the error is not cumulative as $\dot{V}_{c_i}(t)$ is not integrated to calculate the cushion volume. Therefore it is assumed that this approximation should not cause any significant deviations from the accurate solution.

2.7 Wave volume and wave volume pumping

Wave volume pumping is the rate of volume change due to waves passing through the cushion chambers. The wave volume pumping is calculated according to equation (2.32). The volume that the wave occupies inside the cushion can be described as in equation (2.33). These equations are inspired by Auestad [2015], as well as Sørensen and Egeland [1995].

$$\dot{V}_{0_i}(t) = \int_{y_{1_i}}^{y_{2_i}} \int_{L_{1_i}}^{L_{2_i}} \dot{\zeta}(x, y, t) dA \tag{2.32}$$

$$V_{0_i}(t) = \int_{y_{1_i}}^{y_{2_i}} \int_{L_{1_i}}^{L_{2_i}} \zeta(x, y, t) dA \tag{2.33}$$

In these equations y_{1_i} and y_{2_i} constitute the width of cushion i, while L_{1_i} to L_{2_i} constitutes the length of cushion i, measured at the current water-level. If the vessel holds a roll angle, the length of the cushion will be dependent on the y-coordinate, due to the shape of the cushion chambers. This is simplified here, so that the length L_{1_i} to L_{2_i} are taken as an average of the front and aft corner x-positions of the cushion. Thus L_{1_i} and L_{2_i} are given as shown in (2.34) and (2.35). This approximation is believed to be close enough to the real solution as to not cause any significant error.

$$L_{1_i} = \frac{1}{2}(P_{1x} + P_{2x}) \tag{2.34}$$

$$L_{2_i} = \frac{1}{2}(P_{3x} + P_{4x}) \tag{2.35}$$

Finally, in equation (2.32), $\zeta(x, y, t)$ is the function expressing the wave elevation at position x and y, at time t. This wave elevation can be described as given in equation (2.36), which is gathered from Perez [2005].

$$\zeta(x, y, t) = \bar{\zeta} \sin\Big(\omega t + \epsilon - k(x\cos(\chi) + y\sin(\chi)\Big) \tag{2.36}$$

$$\dot{\zeta}(x, y, t) = \bar{\zeta}\omega \cos\Big(\omega t + \epsilon - k(x\cos(\chi) + y\sin(\chi)\Big) \tag{2.37}$$

In the equations above, $\bar{\zeta}$ is the wave amplitude, ω is the circular wave frequency, and k is the wave number, which can be expressed as $k = \frac{2\pi}{\lambda}$, where λ is the wave length. Furthermore, ϵ is the phase of the wave, and the term $x\cos(\chi) + y\sin(\chi)$ expresses the direction of the wave propagation relative to the vessel body-frame.
Differentiating equation (2.36), provides equation (2.37), which is used to calculate the wave volume pumping in equation (2.32). The wave elevation and corresponding wave-forces acting on the vessel, outside of the cushion pressure, will be modeled using the *Marine Systems Simulator* created by Fossen and Perez [2004], and will not be further elaborated on here.

2.8 Linearized cushion pressure dynamics

This sub-chapter is greatly inspired by the work done in Sørensen and Egeland [1995] and Auestad [2015]. Furthermore, the equations for the pressure dynamics of the cushions are based on equations derived in Sørensen and Egeland [1995] and Auestad [2015].
The linear pressure is considered to be uniform within each cushion chamber. The pressure in each chamber is denoted p_{c_i} and is calculated as

$$p_{c_i}(t) = p_a + p_{u_i}(t). \tag{2.38}$$

Here p_a is the atmospheric pressure, while $p_{u_i}(t)$ is the uniform excess pressure. As discussed in the previous chapters, the cushion volume will vary with the elevation of the water surface, and the heave, pitch and roll of the vessel. When the vessel is in equilibrium, meaning it has no movement, the excess pressure p_{u_i} should equal the equilibrium pressure, p_{0_i}. The excess pressure can be written in a non-dimensional form, as μ_u, where

$$\mu_{u_i}(t) = \frac{p_{u_i}(t) - p_0}{p_0} \tag{2.39}$$

The pressure p_0 is considered to be the same for all cushions. As the vessel is initially designed with a single cushion solution, and the walls of the cushions are considered thin, assuming equal p_0 for all cushions is reasonable. The interaction between the geometry, volume, air leakage, wave volume pumping of the cushions and the movements of the vessel can be expressed as shown in equation (2.40).

$$\begin{aligned} K_{1_i}\dot{\mu}_{u_i}(t) + &K_3\mu_{u_i}(t) + \rho_{c0}A_{c_i}\dot{\eta}_3(t) \\ &+\rho_{c0}A_{c_i}y_{cp_i}\dot{\eta}_4(t) - \rho_{c0}A_{c_i}x_{cp_i}\dot{\eta}_5(t) \\ &= K_{2_i}\Delta A_{2_i}^{ctrl}(t) + \rho_{c0}\dot{V}_{0_i}(t) \end{aligned} \tag{2.40}$$

As explained in chapter 2.5, both the centers of pressure, $x_{cp_i}(t)$ and $y_{cp_i}(t)$, as well as the cushion area, $A_{c_i}(t)$, are dependent on the heave, roll and pitch of the vessel and thus are functions of time. Note that these three variables are not seen as functions of time in this equation. As the the equation is a linear approximation, these values must remain constant in time for the equation to remain linear. Thus, the A_{c_i} used here is the average cushion area, found as

$$A_{c_i} = \frac{A_{c_i}(z_{top}) + A_{c_i}(z_{bot})}{2}. \tag{2.41}$$

The time invariant x_{cp_i} and y_{cp_i} can still be calculated from equations (2.17) and (2.18), only inputting the constant, time-invariant area calculated in (2.41), instead of $A_i(t)$. Note that as the equation is a linearization, it is only valid for small changes in angle, and small changes in pressure around the point of the linearization, which is set at p_0.
The calculations of the constants K_{1_i}, K_{2_i} and K_{3_i} are based on equations derived in Sørensen and Egeland [1995] and Auestad [2015], and are given as shown below.

$$K_{1_i} = \frac{\rho_{c0}(z_1 - z_2)}{\gamma(1 + \frac{p_a}{p_0})}(A_{c_i}^{Top} + A_{c_i}^{Bot})\frac{1}{2} \tag{2.42}$$

$$K_{2_i} = \rho_{c0}c_{n_i}\sqrt{\frac{2p_0}{\rho_a}} \tag{2.43}$$

$$K_3 = \rho_{c0}\sum_{j=1}^{q}\left(\frac{Q_{0j}}{2} - p_0\frac{\partial Q}{\partial p}\bigg|_{0_j}\right) \tag{2.44}$$

Here ρ_a is the density of the air collected from the atmosphere, at the atmospheric pressure p_a. Similarly, p_0 and ρ_0 is the cushion equilibrium pressure and corresponding air density, while γ is the ratio of specific heat for air. The term $(z_1 - z_2) \times (A_{c_i}^{Top} + A_{c_i}^{Bot})\frac{1}{2}$ is an expression for the total volume of the cushion. Q_{0j} is the air flow rate at the forementioned equilibrium pressure, while $\frac{\partial Q}{\partial p}|_{0_j}$ is the corresponding linearized fan slope around the equilibrium point for fan number j. Finally, c_n is the leakage coefficient, which is dependent on the shape of the leakage area. $\dot{V}_{0_i}(t)$ is the wave volume pumping, which is explained in chapter 2.7.

2.9 Non-linear cushion pressure dynamics

The non-linear cushion pressure dynamics is an integral part of the model, and will be derived and explained in this sub-chapter. The non-linear pressure dynamics equations are in inspired by Sørensen and Egeland [1995]. These equations are partly by the work done by Umoe Mandal as implemented part of the model at model take-over. Some assumptions regarding the linearization of the air flow, and spatial variations in pressure vary from Sørensen and Egeland [1995], leading to a few changes to these equations. Further, the equations are adapted to the current model, such that it includes the four cushion solution. Another change to these equations is the correction of a minor error with regards to the pressure-density relation in the cushions, which existed in the current model for one cushion from Umoe Mandal. This correction is highlighted in the derivation below.

The basis for the non-linear pressure dynamics is the equation for continuity of mass flow and the relation between pressure and density, shown in equations (2.45) and (2.52) respectively.

$$\dot{m}_{in_i} - \dot{m}_{out_i} = \frac{d}{dt}(\rho_{c_i}(t)V_{c_i}(t) \tag{2.45}$$

In equation (2.45), the left part can be stated as shown below.

$$\dot{m}_{in_i} - \dot{m}_{out_i} = \rho_a(Q_{in_j}(t) - Q_{out_j}(t)) \tag{2.46}$$

By completing the differentiation on the right-hand side in equation (2.45), and substituting the left side with (2.46), we get equation (2.47).

$$\rho_a(Q_{in_j}(t) - Q_{out_j}(t)) = \dot{\rho}_{c_i}(t)V_{c_i}(t) + \rho_{c_i}(t)\dot{V}_{c_i}(t) \tag{2.47}$$

Here $V_{c_i}(t)$ and $\dot{V}_{c_i}(t)$ is the chamber air volume and its rate of change, as calculated in chapter 2.6. Q_j is the air flow caused by fan j, while ρ_a and ρ_{c_i} are the respective air-densities in the atmosphere and the cushion.

In the software implementation provided at project start, the pressure-density relationship inside the cushions were stated as

$$\rho_{c_i}(t) = \rho_a \left(\frac{p_a + p_{u_i}(t)}{p_a + p_0} \right)^{\frac{1}{\gamma}}, \tag{2.48}$$

which was discovered to be erroneous.

Provided the assumption of an adiabatic pressure-density relationship, the first law of thermodynamics, $\delta U + \delta W = \delta Q = 0$, can be used to derive the pressure-volume relationship as

$$\frac{P}{P_0} = \left(\frac{V_0}{V}\right)^{\gamma}. \tag{2.49}$$

Here γ is the ratio of specific heat for air. Since there is no loss of mass from the volumes V_0 to V, the volume-density relationship between the two spaces can be written as

$$\frac{V_0}{V} = \frac{\rho}{\rho_0}. \tag{2.50}$$

The pressure-density relationship then becomes

$$\rho = \rho_0\left(\frac{P}{P_0}\right)^{\frac{1}{\gamma}}. \tag{2.51}$$

As we are interested in the pressure differential from the atmosphere to the cushion, the values for the cushion and atmospheric pressure and density are substituted into equation (2.51). The equation relevant for our system then becomes as shown in equation (2.52), as opposed to the previously used equation given in (2.48).

$$\rho_{c_i}(t) = \rho_a\left(\frac{p_a + p_{u_i}(t)}{p_a}\right)^{\frac{1}{\gamma}} \tag{2.52}$$

Differentiating equation (2.52) with respect to time, provides the expression for $\dot{\rho}_{c_i}(t)$ as

$$\dot{\rho}_{c_i}(t) = \frac{\rho_a}{p_a^{\frac{1}{\gamma}}\gamma}(p_a + p_{u_i}(t))^{\frac{1-\gamma}{\gamma}}\dot{p}_{u_i}(t). \tag{2.53}$$

By combining equations (2.47), (2.52) and (2.53), the final equation expressing the non-linear cushion pressure can be obtained as

$$\dot{p}_{u_i}(t) = \frac{\gamma(p_a + p_{u_i}(t))}{V_{c_i}(t)}\left(\left(\frac{p_a}{p_a + p_{u_i}(t)}\right)^{\frac{1}{\gamma}}(Q_{in_j}(t) - Q_{out_j}(t)) - \dot{V}_{c_i}(t)\right). \tag{2.54}$$

2.10 Cushion air flow

The amount of air inside the cushions is determined by the rate of the influx of air against the rate of loss inside the cushion. Varying the air-flow in and out of the cushion is the only way to exert control over the system, and will be explained in detail in the next sub-chapters.

2.10.1 Cushion air gain

The flow of air into the cushions are caused by fans. The volumetric flow rate produced by each of these fans, can be described as

$$Q_{in_i} = \frac{s_i}{s_{max}} Q_i^*. \tag{2.55}$$

Here Q_i^* is the flow of the fan for cushion i which is set by the fan characteristics. s_i and s_{max} is the current and maximum fan rotation speed. The pressure generated by the lift fan is given as $p = (\frac{s_i}{s_{max}})^2 p_i^*$, where the specific fan pressure p_i^* can be substituted with p_{u_i}. The flow characteristics Q_i^* and the implementation of equation 2.55 are provided by Umoe Mandal, and is left unchanged in this project.

2.10.2 Cushion air loss, leakage

Airflow out of the cushions is called air leakage. There are two types of leakage to consider, passive leakage and controlled leakage. Controlled air leakage is the airflow that exits out of the controlled ventilation valves at the sides of the cushion chambers. The passive leakage is the uncontrolled leakage that occurs when air is forced out from under the sides of the cushion chambers, or leaves the chamber in any way that is not controlled or intentional. The amount of air leakage is dependent on the leakage area and the cushion pressure. The total leakage area $A_{L_i}(t)$ can be expressed as

$$A_{L_i}(t) = A_{p_i}(t) + A_i^{ctrl}(t), \tag{2.56}$$

where $A_{p_i}(t)$ is the passive leakage area, and $A^{ctrl}(t)$ is the controlled leakage area. All the controlled leakage will occur from cushion to atmosphere, while the total passive cushion leakage can be expressed as

$$A_{p_i}(t) = A_{p_i}^a(t) + A_{p_i}^c(t). \tag{2.57}$$

Here the superscripts a and c denotes the cushion to atmosphere leakage area, and the cushion to cushion leakage area respectively. We wish to create and expression for the air flow out of the cushions. According to White [2015], the volumetric flow rate is defined as

$$Q = vA = vA_L c_n \tag{2.58}$$

where v is the velocity of the fluid, while A is the cross-sectional area. Due to the geometry of the leakage area some flow reduction will occur, such that $A = A_L c_n$, where A_L is the leakage area, and c_n is a orifice coefficient for the leakage area. The volumetric flow determining the rate of the influx and the leakage of air in the cushion can be derived by starting with eulers equation

$$\frac{dp}{\rho} + vdv + gdz = 0. \tag{2.59}$$

An expression for Bernoullis principle can be found by integrating the expression above. We wish to derive an expression for a compressible fluid, and assume an adiabatic pressure-density relationship, such that

$$\frac{p}{\rho^\gamma} = C \quad \longrightarrow \quad \frac{1}{\rho} = \frac{C^{\frac{1}{\gamma}}}{p^{\frac{1}{\gamma}}}. \tag{2.60}$$

The Bernoulli equation for an adiabatic, compressible flow can be derived by inserting the right side expression of (2.60) into (2.59) and completing the integration. The first term in (2.59) can then be written as

$$\int \frac{C^{\frac{1}{\gamma}}}{p^{\frac{1}{\gamma}}} dp + \int v dv + \int g dz = C_1, \tag{2.61}$$

where

$$\int \frac{C^{\frac{1}{\gamma}}}{p^{\frac{1}{\gamma}}} dp = C^{\frac{1}{\gamma}} \frac{\gamma}{\gamma - 1} p^{\frac{\gamma-1}{\gamma}} = \frac{p^{\frac{1}{\gamma}}}{\rho} \frac{\gamma}{\gamma - 1} p^{\frac{\gamma-1}{\gamma}}. \tag{2.62}$$

Shortening the expression found in (2.62), the integrated density over pressure can be written as

$$\int \frac{C^{\frac{1}{\gamma}}}{p^{\frac{1}{\gamma}}} dp = \left(\frac{\gamma}{\gamma - 1}\right) \frac{p}{\rho}. \tag{2.63}$$

Inserting the expression in the equation above into (2.61), and assuming none, or negligible elevation change, the simplified Bernoulli equation for adiabatic compressible flow can be written as

$$\left(\frac{\gamma}{\gamma - 1}\right) \frac{p_{c_i}(t)}{\rho_{c_i}(t)} + \frac{1}{2} v_i^2 = \left(\frac{\gamma}{\gamma - 1}\right) \frac{p_a}{\rho_a} + \frac{1}{2} v_a^2. \tag{2.64}$$

From this, an expression for the air velocity can be derived. We assume no initial air-velocity in the chambers, such that $v_i = 0$. Further, we assume that all excess pressure in the ventilated air from a cushion is converted to air-velocity upon release. Thus equation (2.64) can be rearranged to express the velocity, as shown in equation (2.65).

$$v_a(t) = \sqrt{2 \left(\frac{\gamma}{\gamma - 1}\right) \left(\frac{p_{c_i}(t)}{\rho_{c_i}(t)} - \frac{p_a}{\rho_a}\right)} \tag{2.65}$$

The pressure inside the cushion is described as

$$p_{c_i}(t) = p_a + p_{u_i}(t), \tag{2.66}$$

where p_{c_i} is the total cushion pressure, which can be split into the atmospheric pressure p_a and the uniform cushion pressure p_{u_i}. By inserting this expression for $p_{c_i}(t)$ into (2.65) and combining with equation (2.58), we get a final expression describing the volumetric flow from cushion to atmosphere as

$$Q_i(t) = A^a(t) \sqrt{2 \left(\frac{\gamma}{\gamma - 1}\right) \left(\frac{p_{u_i}(t) + p_a}{\rho_c(t)} - \frac{p_a}{\rho_a}\right)}. \tag{2.67}$$

Here $A^a(t)$ represents an arbitrary leakage area from cushion to atmosphere, which can be substituted to account for the relevant leakage flow.

Controlled leakage

The controlled leakage area can be expressed as

$$A_i^{ctrl}(t) = A_{i_{max}}^{ctrl} \frac{A_{i_{min\%}}^{ctrl} + (1 - A_{i_{min\%}}^{ctrl})u_i(t)}{100}. \tag{2.68}$$

Here $A_{i_{max}}^{ctrl}$ is the leakage area at maximum vent valve opening. $A_{i_{min\%}}^{ctrl}$ is the lowest possible area of the vent valve opening, given as a percentage of the maximum vent valve opening. Finally $u(t)_i$ is the control input signal, for the opening of the vent valves. The controlled volume flow out of louver i can then be expressed as

$$Q_i^{ctrl}(t) = A_i^{ctrl}(t) c_{n_i}^{vv} \sqrt{2\left(\frac{\gamma}{\gamma - 1}\right)\left(\frac{p_{u_i}(t) + p_a}{\rho_c(t)} - \frac{p_a}{\rho_a}\right)}, \tag{2.69}$$

where $c_{n_i}^{vv}$ is the orifice coefficient for the ventilation valves.

Passive leakage

The passive leakage area is calculated as the sum of any area that occurs under the hull, fingers or bag of the vessel that is lifted out of the water.

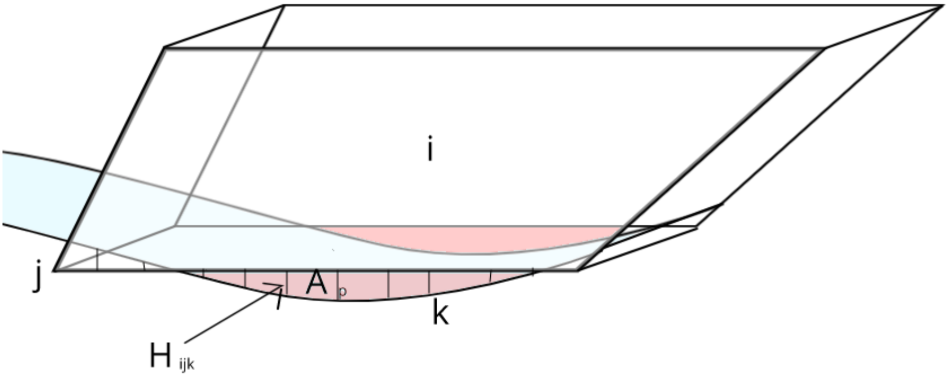

Figure 2.7: Leakage area for cushion chamber *i*. Blue area illustrates the water plane, red area shows the corresponding passive leakage area.

The passive leakage area can be further divided into inter-cushion leakage, and atmospheric leakage. As mentioned in chapter 1.4.1, the cushion dividers were selected to cover the entire distance from wetdeck to baseline in order to minimize the inter-cushion leakage area. To calculate the passive leakage area for a chamber, the bottom edge of each wall surrounding a chamber divided into ten points. At each of these points, the height from the water to the draft at the given point is calculated following equation (2.70). Figure 2.7 attempts to better illustrate this division and the corresponding leak height. If the height calculated by (2.70) is negative, leakage occurs.

$$H_{L_{ijk}}(t) = -T - \eta_3(t) - y_{ijk}(t)\eta_4(t) + x_{ijk}(t)\eta_5(t) + h_{p_i}(t) - \zeta_{ijk}(t) \tag{2.70}$$

In the equation above, $H_{L_{ijk}}(t)$ is the height of point k on line j for cushion i, relative to the water plane. T is the draught of the vessel at the initial heave position, $\eta_3 = 0$. Furthermore $y_{ijk}(t)$ and $x_{ijk}(t)$ is the distance from the center of gravity to point ijk. The first four terms in (2.70) are a part of the leakage height for the single-cushion solution at project start. For the new model, the term $h_{p_i}(t)$ is added to account for the lower water-level in the cushion due to the over-pressure inside the cushion. The effect of $h_p(t)$ is further illustrated in Figure 1.6, and can be expressed as

$$h_p(t) = \frac{p_u(t)}{g\rho_w}. \tag{2.71}$$

Finally, the term $\zeta_{ijk}(t)$ is added to account for the sea elevation at the relative position of point ijk. This elevation can be expressed as

$$\zeta_{ijk}(t) = \sum_n \Big(\zeta_{a_n} \sin(\omega_n t - \kappa_n(x_{ijk}\cos(\chi_n) + y_{ijk}\sin(\chi_n)) + \epsilon_n)\Big). \tag{2.72}$$

Most terms in equation (2.72) are previously addressed and explained in chapter 2.7. Note that in the equation above, the letter k is used as a subscript, therefore the letter κ is used to denote the wave number. For an irregular seastate, the specific wave elevation at a point will be the sum of many different regular waves. The elevation for each of these regular waves are expressed as previously explained in equation (2.36). Therefore, the total wave elevation at point ijk, becomes the sum of the elevation from every regular wave at the given time and the given position of the point. The position of point ijk is expressed by x_{ijk} and y_{ijk}. Finally, ϵ_n represents the phase of regular wave number n. The leakage area from cushion to atmosphere and cushion to cushion, for each cushion, can ultimately be calculated as

$$A^a_{p_i}(t) = \sum_{j_a=1}^{2} \Big(H_{L_{ij_a}}(t) \sum_{k=1}^{10} (\Delta x_{ij_a k} + \Delta y_{ij_a k})\Big), \tag{2.73}$$

and

$$A^c_{p_i}(t) = \sum_{j_c=1}^{2} \Big(H_{L_{ij_c}}(t) \sum_{k=1}^{10} (\Delta x_{ij_c k} + \Delta y_{ij_c k})\Big). \tag{2.74}$$

Here, subscript j_c signifies the walls that separate cushions, and subscript j_a signifies the walls j which separate cushion and atmosphere. The volumetric flow rate from cushion to atmosphere is found by inserting the atmospheric leakage area, $A^a_{p_i}(t)c^p_{n_i}$ into A^a in equation (2.67), where $c^p_{n_i}$ is the orifice coefficient for the passive leakage area.

To find the volumetric flow rate for the inter-cushion leakage, we assume that the pressure in cushion i is higher than the pressure in cushion j. Like before, we also assume no initial air-velocity in i, and that all pressure differential between cushions i and j is converted to air-velocity when the air enters cushion chamber j. By also assuming an adiabatic pressure density relationship, the expression formed for v_j in equation (2.65) can be applied. The volumetric air-flow between cushions can be expressed by substituting the areas, pressures and densities in equation (2.69), with the relevant values for the two cushions affected by the leak. The cushion air density ρ_{c_i} can be calculated from the expression derived in equation (2.52).

$$Q_i(t) = A^c_{p_i}(t)c^p_{n_i}\sqrt{\frac{2\gamma}{\gamma-1}\left(\frac{p_{c_i}(t)}{\rho_{c_i}(t)} - \frac{p_{c_j}(t)}{\rho_{c_j}(t)}\right)} \tag{2.75}$$

Equation (2.75) expresses the air flow out from cushion i, due to leakage into cushion j. There is no loss of mass in the exchange, meaning that the corresponding air-flow out from cushion j is the same as the air flow expressed in (2.75), but with a negative sign. Note that if the cushion pressure is reversed, that is cushion j holds a higher pressure than cushion i, the i and j subscripts in equation (2.75) are switched. Also note that the cushion separating walls are considered solid, such that no air can pass though them. However, as best illustrated by the pictures in chapter 1.5, they are in practice inflatable bags. Because of this, it is believed that a certain amount of leakage between the cushions might occur. To account for this, a static or height varying leakage area can be set as a parameter input in the model. This parameter will have to be found empirically from the scale-model data.

2.11 Cushion forces

The cushion forces can be divided into linear and non-linear forces, which are used for the control plant model and the process plant model, respectively. These two models will be further explained in the next chapters, 2.13 and 2.12.

2.11.1 Non-linear cushion forces

The forces generated by the cushions and their resulting pressure can be calculated following as $F = p \times A$. In similar fashion, the moments generated by the cushion pressure is calculated as $M = d_{cp} \times p \times A$. Here d_{cp} represents the x_{cp} and y_{cp} distance from the center of pressure from the center of gravity as calculated in chapter 2.5.1. Summarizing the force and moments induced by each of the cushions, we get the total forces and moments acting on the vessel caused by the cushion pressure. The expression for these forces and moments can be seen below in equations (2.76) to (2.78).

$$F_{3_c}(t) = \sum_{i=1}^{4} -p_0\mu_{u_i}(t)A_{z_i}(t) \tag{2.76}$$

$$M_{4_c}(t) = \sum_{i=1}^{4} -y_{cp_i}(t)p_0\mu_{u_i}(t)A_{z_i}(t) \tag{2.77}$$

$$M_{5_c}(t) = \sum_{i=1}^{4} x_{cp_i}(t)p_0\mu_{u_i}(t)A_{z_i}(t) \tag{2.78}$$

Note that because the positive z-direction is defined as down, and a positive pressure will cause a force working upwards, the heave force, $F_{3_c}(t)$ and the roll moment, $M_{4_c}(t)$ will have negative signs. Since both the pressure area, $A_{z_i}(t)$, the distance to the center of pressure, $x-$ and $y_{cp_i}(t)$ and the non-dimensional pressure, $p_0\mu_{u_i}(t)$ are all functions of time, the corresponding forces will not be linear. Furthermore, the calculation of the pressure used in these equations is done following the equation shown in (2.54), which means that $p_0\mu_{u_i}(t)$ is not linear either. For simplicity, only the force in heave, and the resulting moments caused by force in the z-direction, that is roll and pitch, will be considered.

As an addition to the existing model at project start, we also wish to include the components from forces acting on the vessel via the ventilation of cushion pressure. Following Newton's third law of motion, every action has an equal and opposite reaction. As the pressurized air escapes out from the ventilation valves in the cushions, an equal and opposite force caused by the velocity and mass of the escaping air, will act on the vessel. This force can be calculated as $F = \rho_a A^{ctrl} v_a^2$, where A^{ctrl} is the controlled leakage area of the chamber, and v is the velocity of the air. Note that v can also be written as $\frac{Q}{A}$, as these are the units that have mainly been used through the modeling. The corresponding forces acting on the vessel from this effect can then be written as

$$M_{4_Q}(t) = -\sum_{i=2}^{3} z_{ca_i}\rho_{a_i}(t)\frac{Q_{out_i}^2(t)}{A_i^{ctrl}(t)} + \sum_{i=\{1,4\}} z_{ca_i}\rho_{a_i}(t)\frac{Q_{out_i}^2(t)}{A_i^{ctrl}(t)}, \tag{2.79}$$

Here Q_{out_i} is the volume flow out of the cushion, where only the controlled leakage is considered. The passive leakage is anticipated to be small enough to be disregarded in this context. In the equation above, z_{ca_i} is the distance from the vessel center of gravity to the center of area for the cushion ventilation valve, A^{ctrl}. An expression for ρ_{c_i} has already been derived, and can be found in equation (2.53). This ventilation of air will also cause substantial forces in sway and yaw, which are not considered here. The combined resulting non-linear forces acting on the vessel can be state on vector form as

$$\boldsymbol{\tau}_{combined} = \boldsymbol{\tau}_c + \boldsymbol{\tau}_Q \tag{2.80}$$

where $\boldsymbol{\tau}$ is a matrix represented as
$\boldsymbol{\tau} = [F_1, F_2, F_3, M_4, M_5, M_6]^T$, with the corresponding subscripts of c and Q.

2.11.2 Linear cushion forces

To create equations for cushion forces that are linear, the area and center of pressure in equations (2.76) through (2.78) will have to be constant. Thus the cushion area is calculated as shown in equation (2.41), with the centers of pressure calculated by equations (2.17) and (2.18) with the average area as input. Furthermore, the pressure must be linear, as expressed by equation (2.66) and discussed in chapter 2.8. Using these time-invariant, constant expressions for A_{z_i}, x_{cp_i} and y_{cp_i}, as well as the linear non-dimensional pressure $p_0\mu_{u_i}$, the linear forces can be expressed as in the equations below.

$$F_{3_c}(t) = \sum_{i=1}^{4} -p_0\mu_{u_i}(t)A_{z_i} \tag{2.81}$$

$$M_{4_c}(t) = \sum_{i=1}^{4} -y_{cp_i}p_0\mu_{u_i}(t)A_{z_i} \tag{2.82}$$

$$M_{5_c}(t) = \sum_{i=1}^{4} x_{cp_i}p_0\mu_{u_i}(t)A_{z_i} \tag{2.83}$$

2.12 Control plant model

The control plant model is the model of the vessel that any controller and observer will relate to. This is a simplified model, which is both fast to compute, and fairly accurate. The equations of motion regarding the control plant model can be stated as a mass-spring-damper system for each of the degrees of freedom, as is discussed in chapter 2.2. For this thesis, the relevant degrees of freedom are heave, roll and pitch. Thus these movements can be modeled as shown in equations (2.84), (2.85) and (2.86).

$$(m + A_{33})\ddot{\eta}_3(t) + B_{33}\dot{\eta}_3 + C_{33}\eta_3 + F_{c_3}(t) = F_3^e(t) \tag{2.84}$$

$$(I_{44} + A_{44})\ddot{\eta}_4(t) + B_{44}\dot{\eta}_4 + C_{44}\eta_4 + M_{c_4}(t) = M_4^e(t) \tag{2.85}$$

$$(I_{55} + A_{55})\ddot{\eta}_5(t) + B_{55}\dot{\eta}_3 + C_{55}\eta_5 + M_{c_5}(t) = M_5^e(t) \tag{2.86}$$

Here, $F_3^e(t)$, $M_4^e(t)$ and $M_5^e(t)$ are excitation forces and moments caused by waves and other external forces. The forces an moments noted with subscript c, are cushion forces and moments acting on the vessel. The equations for these are derived and listed in (2.81), (2.82) and (2.83). The constant m represents the vessel mass. The constants A, B and C represents the hydrodynamic added mass, the potential damping and restoring coefficient for the mass-spring-damper motion of the vessel. Their subscripts 3, 4 and 5 denote the movements in heave, roll and pitch, respectively. A double subscript of i.e. 44 means that the constant contributes to a roll force, due to a roll acceleration, velocity or position. We assume that none of these forces are coupled, meaning that only subscripts 33, 44 and 55 are required. Finally in the equations above, the inertia governing the roll and pitch motion of the vessel is given as I. The values for these A, B and C constants have been computed in ShipX and Veres, and are provided by Umoe Mandal.

2.12.1 State space representation

The equations of motion can be expressed in the linear time-invariant state-space form shown in (2.87) and (2.88).

$$\dot{\boldsymbol{x}}(t) = \boldsymbol{A}\boldsymbol{x}(t) + \boldsymbol{B}\boldsymbol{u}(t) + \boldsymbol{E}\boldsymbol{\omega}(t) \tag{2.87}$$

$$\boldsymbol{y}(t) = \boldsymbol{C}\boldsymbol{x}(t) \tag{2.88}$$

Here, $\boldsymbol{x}(t)$ is the state vector, which represents the relevant degrees of freedom of the vessel. The representation of the vector $\boldsymbol{x}(t)$ is listed in the table below. $\boldsymbol{u}(t)$ is the control input, which will be further discussed in chapter 3. $\boldsymbol{\omega}(t)$ is the disturbance vector, which comprises of external forces and disturbances. $\boldsymbol{y}(t)$ is the output vector, and holds the values for any measured states such as data from accelerometers or gyros. The value for the matrices $\boldsymbol{A}$, $\boldsymbol{B}$, $\boldsymbol{E}$ and $\boldsymbol{C}$ can be found in appendix A. Note that the K-constants in the $\boldsymbol{A}$, $\boldsymbol{B}$ and $\boldsymbol{E}$ matrices have subscripts first denoting which constant it is, with reference to equations (2.42) through (2.44), while the second number is the reference to the cushion number, i.e. K_{23} is the constant K_2 for cushion 3.

States $\boldsymbol{x(t)}$

Number	Description	Symbol
$x_1(t)$	Heave position	η_3
$x_2(t)$	Roll angle	η_4
$x_3(t)$	Pitch angle	η_5
$x_4(t)$	Heave velocity	$\dot{\eta}_3$
$x_5(t)$	Roll velocity	$\dot{\eta}_4$
$x_6(t)$	Pitch velocity	$\dot{\eta}_5$
$x_7(t)$	Non-dim. pressure, chamber 1	μ_{u_1}
$x_8(t)$	Non-dim. pressure, chamber 2	μ_{u_2}
$x_9(t)$	Non-dim. pressure, chamber 3	μ_{u_3}
$x_{10}(t)$	Non-dim. pressure, chamber 4	μ_{u_4}

States $\boldsymbol{y(t)}$

Number	Description	Symbol
$y_1(t)$	Roll angle	η_4
$y_2(t)$	Pitch angle	η_5
$y_3(t)$	Heave velocity	$\dot{\eta}_3$
$y_4(t)$	Roll velocity	$\dot{\eta}_4$
$y_5(t)$	Pitch velocity	$\dot{\eta}_5$
$y_6(t)$	Pressure, chamber 1	p_{c_4}
$y_7(t)$	Pressure, chamber 2	p_{c_4}
$y_8(t)$	Pressure, chamber 3	p_{c_4}
$y_9(t)$	Pressure, chamber 4	p_{c_4}

States $\omega(t)$

Number	Description	Symbol
$\omega_1(t)$	Heave force	F_3^e
$\omega_2(t)$	Roll moment	M_4^e
$\omega_3(t)$	Pitch moment	M_4^e
$\omega_4(t)$	Diff. volume chamber 1	$\dot{V}_1$
$\omega_5(t)$	Diff. volume chamber 2	$\dot{V}_2$
$\omega_6(t)$	Diff. volume chamber 3	$\dot{V}_3$
$\omega_7(t)$	Diff. volume chamber 4	$\dot{V}_4$

2.13 Process plant model

The process plant model is the model that is used to calculate the actual movements of the vessel. This model does not have the same requirements for simplicity and computational speed as the control plant model does. This is because the process plant model will not have to be computed in real-time for the real vessel, but rather is intended to express the physical world of and around the real vessel.

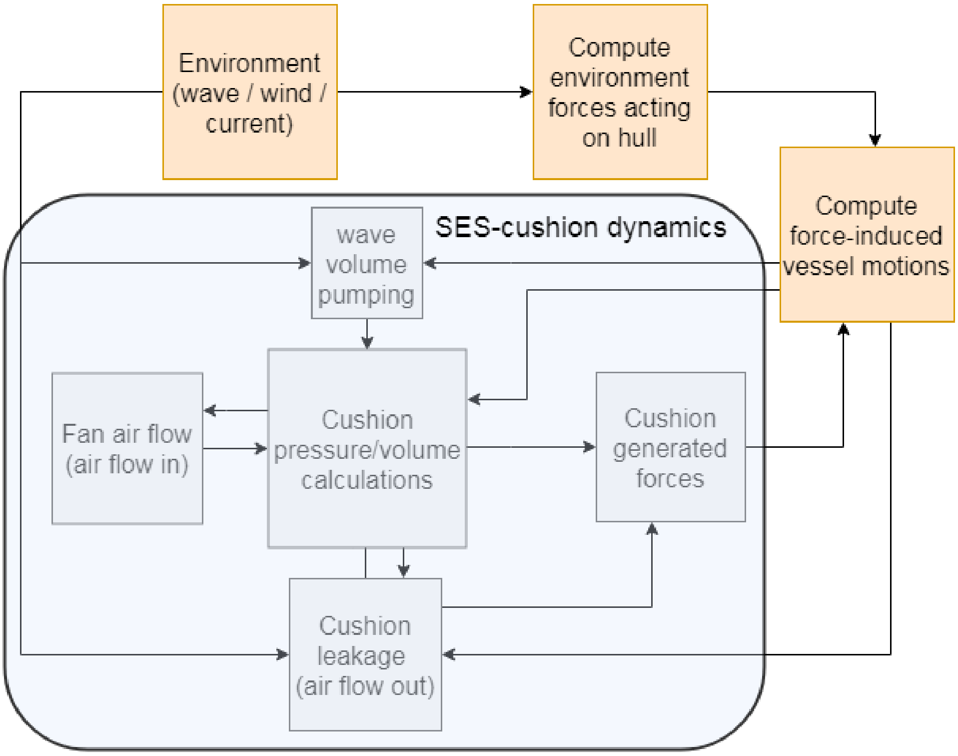

Figure 2.8: Diagram of the SES-sim model structure

As previously mentioned in chapter 2.2, the simulated movements of the vessel is largely handled by the MSS library, created by Fossen and Perez [2004]. Thus only the forces induced by the cushions of the vessel have to be calculated. These forces are the non-linear forces and moments explained in chapter 2.11.1, calculated from equations (2.76), (2.77) and (2.78). As described in chapter 2.11.1, these forces are a product of the non-linear cushion pressure, as well as the time variant cushion areas and centers of pressure. Thus they are the closest representation of the real physical world. The mathematical model derived in the chapter above is implemented in MATLAB®/Simulink®. The equations governing the SES-cushion dynamics and the corresponding forces are integrated into a larger system referred to as SES-sim. An illustration of the structure of this system is given in Figure 2.8. The orange blocks are taken from the Marine System Simulator (MSS), created by Fossen and Perez [2004], which contain a few additions and changes by Umoe Mandal. The blue square contains a simplified overview of the different equations which are derived in the chapters above and gathered into modules.

2.14 Noise

To emulate realistic testing conditions, noise is added to the output states. Generally, the measurement noise can be divided into two components:

- **Sensor noise:** the small fluctuations in the measurement, when no motion is present. The sensor noise can be seen when the vessel is off cushion and without movement in still water. Assuming that the sensors are the same for full scale and model scale, this component of the noise will not have to be scaled for the full scale model.
- **Process noise:** noise caused by the operation of the SES. The process noise is assumed to constitute the main component of the feedback noise. Pumps, louver actuators, escaping air from the cushions and general pressure fluctuations are assumed to be the main causes for the process noise. These phenomenons create vibrations which propagate in the hull and are picked up by the sensors. This component of the noise is scale dependent, and has be to scaled from model scale to full scale. Thus it will provide the same challenges for both the model-scale and the full-scale system.

For the mathematical model, the noise is modeled as Gaussian white noise. The magnitude of both the sensor noise and the process noise is determined from the scale-model tests. There is some uncertainty bound to the scaling the process noise for the 'full-scale' mathematical model from the model-scale testing. The noise should be proportional to the respective undisturbed signal, i.e. according to table 1.1, the full-scale gyroscope noise for roll and pitch rate should be one third of the model scale noise. However, the sensor noise is mainly due to vibrations and motions in the hull. These vibrations and motions can be said to be 9 times larger for the full-scale from a 1:9 scale model. Depending on the workings of the relevant gyroscope, this could result in larger angular disturbances, even though the angle is a non-scaling dimension. Ultimately, the noise has been scaled as to attempt to have the same impact on the 'full-scale' mathematical model as for the model-scale tests. I.e. during the physical model testing, the gains for the controller were limited by the feedback noise. We wish to scale the noise, such that the same limitations will arise for the full-scale model given the same, model scaled, controller gains.

Chapter 3

Filter and controller design

Two simple PID-controllers are designed to control the heave, pitch and roll of the vessel. The control law for a PID-controller can be stated as

$$\boldsymbol{u}(t) = -\boldsymbol{K}\boldsymbol{x}(t) + \boldsymbol{\beta}. \tag{3.1}$$

Here $\boldsymbol{u}(t)$ is the controller output. This output is a vector containing four values, which for the mathematical model translates to the ventilation valve opening of each of the cushions. A controller output of a 100 reads 100% opening on the vent valve, and thus a minimization of the cushion pressure. The constant $\boldsymbol{K}$ is called the gain matrix, and $\boldsymbol{x}(t)$ is the state vector as expressed in chapter 2.12.1. Equations (3.2) and (3.3) show the general structure of the $\boldsymbol{u}(t)$ vector and the $\boldsymbol{K}$ matrix. Finally, $\boldsymbol{\beta}$ is a constant vector signifying the bias of the ventilation valve louvers. The bias essentially states how much lift the vessel should have when no feedback is present.

$$\boldsymbol{u}(t) = \begin{bmatrix} u_1(t) & u_2(t) & u_3(t) & u_4(t) \end{bmatrix}^T \tag{3.2}$$

$$\boldsymbol{K} = \begin{bmatrix} \boldsymbol{KI} & \boldsymbol{KP} & \boldsymbol{KD} \end{bmatrix} \tag{3.3}$$

In the equation above the $\boldsymbol{KI}$, $\boldsymbol{KP}$ and $\boldsymbol{KD}$ matrices specify the integrator gains, the proportional gains, and the derivative gains, respectively. Each of these matrices hold a value for the gain for each cushion, for each degree of freedom. I.e the $\boldsymbol{KI}$-matrix can be expressed as

$$\boldsymbol{KI} = \begin{bmatrix} KI_h & KI_r & KI_p \\ KI_h & -KI_r & KI_p \\ KI_h & -KI_r & -KI_p \\ KI_h & KI_r & -KI_p \end{bmatrix} \tag{3.4}$$

where subscripts h, r and p denote heave, roll and pitch, respectively. The general form of the full $\boldsymbol{K}$-matrix can be seen in equation (3.5). The negative and positive signs in front of each gain in the $\boldsymbol{K}$-matrix in this equation is dependent on which direction the force or moment generated by the cushion affects the specific degree of freedom. I.e. for roll, a positive roll angle should be counteracted by deflating cushions 2 and 3. This means that the valves for cushion 2 and 3 must open, u_2 and u_3 must increase. Following equation (3.1), this means that the $\boldsymbol{K}$-gains for cushion 2 and 3 in roll become negative. Depending on which states we want to control, the structures of $\boldsymbol{K}$ and $\boldsymbol{x}(t)$ might be altered and simplified.

$$K = \begin{bmatrix} KI_h & KI_r & KI_p & KP_h & KP_r & KP_p & KD_h & KD_r & KD_p \\ KI_h & -KI_r & KI_p & KP_h & -KP_r & KP_p & KD_h & -KD_r & KD_p \\ KI_h & -KI_r & -KI_p & KP_h & -KP_r & -KP_p & KD_h & -KD_r & -KD_p \\ KI_h & KI_r & -KI_p & KP_h & KP_r & -KP_p & KD_h & KD_r & -KD_p \end{bmatrix} \tag{3.5}$$

3.1 Controller 1 - Roll, pitch PD controller

We wish to create a PD-position controller to dampen the vessel roll and pitch motions. The control law for this controller is on the form stated in equation (3.1). The controller bias is fixed at $\boldsymbol{\beta} = \mathbf{55.5}$. The gains for the controller is found through aid of the Linear Quadratic Regulator (LQR) optimization. The LQR is a regulator created with the goal of optimizing the amount of control exerted on the system with respect to the resource cost of the control. The cost of control is given by a quadratic function. The goal becomes to minimize the cost function given in equation (3.6) with respect to the control input, $\boldsymbol{u}(t)$.

$$\boldsymbol{J}_{LQR} = \int_{\infty}^{0} [\boldsymbol{x}(t)^T \boldsymbol{Q} \boldsymbol{x}(t) + \boldsymbol{u}(t)^T \boldsymbol{R} \boldsymbol{u}(t) + 2\boldsymbol{x}(t)^T \boldsymbol{N} \boldsymbol{u}(t)] dt \tag{3.6}$$

This minimization is found when the control law $\boldsymbol{u}(t) = -\boldsymbol{K}\boldsymbol{x}(t)$ is used, where $\boldsymbol{K} = \boldsymbol{R}^{-1}(\boldsymbol{B}^T\boldsymbol{P} + \boldsymbol{N})$. The $\boldsymbol{P}$-matrix is determined from the solution to the algebraic Ricatti equation that is shown in equation (3.7). The matrices $\boldsymbol{Q}$ and $\boldsymbol{R}$ can be seen as the weight of a state and the weight of a control input to the cost function, respectively. In other words, large values in the $\boldsymbol{Q}$-matrix will penalize error in the states more, and the LQR will spend more resources to correct the error. On the other hand, large values in the $\boldsymbol{R}$-matrix will penalize the cost of control for correcting the errors, and the LQR will allow more error in the states. The relative difference between the $\boldsymbol{Q}$ and $\boldsymbol{R}$ matrices determine whether or not the controller uses cheap or expensive control. A large $\boldsymbol{R}$ is called expensive control strategy and small values for $\boldsymbol{R}$ is a called cheap control strategy. Note that the control law is the same as the control law for any PID controller. Thus, the LQR optimization can be seen as a simplified and more efficient way of tuning the gains of this controller.

$$(\boldsymbol{A}^T\boldsymbol{P} + \boldsymbol{P}\boldsymbol{A} + \boldsymbol{Q} - (\boldsymbol{P}\boldsymbol{B} + \boldsymbol{N})\boldsymbol{R}^{-1}(\boldsymbol{B}^T\boldsymbol{P} + \boldsymbol{N}^T)) = 0 \tag{3.7}$$

Creating an LQR in Matlab is simply done by using the built in command lqr, which uses the $\boldsymbol{A}$, $\boldsymbol{B}$, $\boldsymbol{Q}$ and $\boldsymbol{R}$ matrices as input to find the minimal solution to the cost function in equation 3.6 and outputs the optimal controller gain, $\boldsymbol{K}$. Through some experimenting, the optimal values for $\boldsymbol{R}$ and a $\boldsymbol{Q}$ are found. $\boldsymbol{R}$ is set as an otherwise empty, diagonal 4x4 matrix with the values of 10^{-4} in the diagonal. $\boldsymbol{Q}$ is a 10x10 matrix, which only has any values in the diagonal at the roll and pitch angle and the roll and pitch velocity. As these are the only states we desire to control they are also the only states we wish to penalize error in. These full matrices can be seen in equations (3.9) and (3.8). The matlab-computed LQR gains then become as listed in equation (3.10).

$$\boldsymbol{R} = \begin{bmatrix} 10^{-4} & 0 & 0 & 0 \\ 0 & 10^{-4} & 0 & 0 \\ 0 & 0 & 10^{-4} & 0 \\ 0 & 0 & 0 & 10^{-4} \end{bmatrix} \tag{3.8}$$

$$\boldsymbol{Q} = \begin{bmatrix} 0 & 0 & 0 & 0 & 0 & 0 & 0 & 0 & 0 & 0 \\ 0 & 1500 & 0 & 0 & 0 & 0 & 0 & 0 & 0 & 0 \\ 0 & 0 & 3000 & 0 & 0 & 0 & 0 & 0 & 0 & 0 \\ 0 & 0 & 0 & 0 & 0 & 0 & 0 & 0 & 0 & 0 \\ 0 & 0 & 0 & 0 & 2000 & 0 & 0 & 0 & 0 & 0 \\ 0 & 0 & 0 & 0 & 0 & 3000 & 0 & 0 & 0 & 0 \\ 0 & 0 & 0 & 0 & 0 & 0 & 0 & 0 & 0 & 0 \\ 0 & 0 & 0 & 0 & 0 & 0 & 0 & 0 & 0 & 0 \\ 0 & 0 & 0 & 0 & 0 & 0 & 0 & 0 & 0 & 0 \\ 0 & 0 & 0 & 0 & 0 & 0 & 0 & 0 & 0 & 0 \end{bmatrix} \tag{3.9}$$

$$\boldsymbol{K} = \frac{3 \times 180}{\pi} \begin{bmatrix} 0 & 10.45 & 13.41 & 0 & 13.07 & 14.21 & 0 & 0 & 0 & 0 \\ 0 & -10.45 & 13.41 & 0 & -13.07 & 14.21 & 0 & 0 & 0 & 0 \\ 0 & -10.63 & -16.85 & 0 & -13.32 & -17.86 & 0 & 0 & 0 & 0 \\ 0 & 10.63 & -16.85 & 0 & 13.32 & -17.86 & 0 & 0 & 0 & 0 \end{bmatrix} \tag{3.10}$$

The term $\frac{3\times180}{\pi}$ is placed outside of the matrix to make a comparison with the gains for the scale-model easier.

3.2 Controller 2 - Heave, roll, pitch damping

This controller is a pure position damping controller, meaning that $\boldsymbol{KI} = \mathbf{0}$ and $\boldsymbol{KP} = \mathbf{0}$, and that only the velocity states, x_4, x_5 and x_6 are relevant. This controller is applied during the scale model experiments. The gains for the controller are selected in real-time, during the scale model experiments. Because of this, a simple controller design is beneficial. The damping gains are symmetric, meaning that they are the same for each cushion, with the signs for the gains of each cushion varying as expressed in 3, and shown in (3.5). The non-zero part of the gain matrix $\boldsymbol{K}$ then becomes

$$\boldsymbol{K} = \begin{bmatrix} KD_h & KD_r & KD_p \\ KD_h & -KD_r & KD_p \\ KD_h & -KD_r & -KD_p \\ KD_h & KD_r & -KD_p \end{bmatrix} \tag{3.11}$$

The damping gains for heave, KD_h vary from 0, meaning no active control, to 200 for the scale model experiments. The damping gains for roll and pitch, KD_r and KD_p, vary from 0 to 6 and 0 to 9 for the model scale, respectively. Since the gains are tuned in real time during the wave basin experiments, they vary from test to test. When this controller is applied to the numerical model, the gains are scaled after table 1.1. In addition, the roll and pitch gains are multiplied by $180/\pi$ to convert from an input in degrees to an input in radians. The complete $\boldsymbol{K}$-gain matrix for a test with heave, roll and pitch control might then look like

$$\boldsymbol{K} = \frac{3 \times 180}{\pi} \begin{bmatrix} 0 & 0 & 0 & 200\frac{\pi}{9\times180} & 6 & 9 & 0 & 0 & 0 & 0 \\ 0 & 0 & 0 & 200\frac{\pi}{9\times180} & -6 & 9 & 0 & 0 & 0 & 0 \\ 0 & 0 & 0 & 200\frac{\pi}{9\times180} & -6 & -9 & 0 & 0 & 0 & 0 \\ 0 & 0 & 0 & 200\frac{\pi}{9\times180} & 6 & -9 & 0 & 0 & 0 & 0 \end{bmatrix}. \tag{3.12}$$

For the scale model experiments, the terms $\frac{3\times180}{\pi}$ and $\frac{\pi}{9\times180}$ would be excluded, as these are scaling terms.

3.3 Stability of the closed loop system

An unstable system can easily lead to unexpected and undesired responses. For physical systems, such responses can easily produce dangerous and harmful situations. Thus, providing a stability proof for the controlled system gives an assurance that the controlled system will only act in a certain way, namely converging towards the equilibrium states of $\boldsymbol{x_0} = 0$.

3.3.1 Stability of unperturbed system

The unperturbed closed loop system, that is $\boldsymbol{E\omega}(t) = 0$, can be said to be exponentially stable around $\boldsymbol{x}_0$ if the closed loop system matrix, $\boldsymbol{A}_{cl}$ is Hurwitz. This means that all the eigenvalues of $\boldsymbol{A}_{cl}$ have strictly negative real parts, i.e $\mathbb{R}(\boldsymbol{\lambda}_i) < \boldsymbol{0}$. By inserting the expression of our chosen controller in (3.1) into the unperturbed state space representation of our system in (2.87), the closed loop system can be expressed as

$$\dot{\boldsymbol{x}}(t) = \boldsymbol{A}\boldsymbol{x}(t) - \boldsymbol{B}\boldsymbol{K}\boldsymbol{x}(t) + \boldsymbol{B}\boldsymbol{\beta} = \boldsymbol{A}_{cl}\boldsymbol{x}(t) + \boldsymbol{B}\boldsymbol{\beta} \tag{3.13}$$

where $\boldsymbol{A}_{cl} = \boldsymbol{A} - \boldsymbol{B}\boldsymbol{K}$. A generalized expression for which values of $\boldsymbol{K}$ that will create a stable closed loop system can be devised by choosing an appropriate Lyapunov function, $\boldsymbol{V}(x)$, and using of the Lyapunov equation. Due to the size of the $\boldsymbol{A}_{cl}$ matrix, and the number of unique gains in the $\boldsymbol{K}$-matrix, such a generalization will become long and tedious. Thus we settle for showing that the selected gains in section 3 will provide a stable closed loop system. The eigenvalues for the closed loop system are calculated in MATLAB®, through the command *eig*($\boldsymbol{A}_{cl}$). The real part of the eigenvalues for controller 1 and for the most aggressive gains for controller 2, as given in (3.12), are given as

$$\mathbb{R}(\boldsymbol{\lambda}^{C_1}_{A_{cl}}) = \begin{bmatrix} -11.2 \\ -11.2 \\ -21.3 \\ -1.35 \\ -1.35 \\ -0.950 \\ -11.4 \\ -11.4 \\ -0.812 \\ -23.6 \end{bmatrix} \qquad \mathbb{R}(\boldsymbol{\lambda}^{C_2}_{A_{cl}}) = \begin{bmatrix} -11.7 \\ -11.7 \\ -11.9 \\ -11.9 \\ -11.8 \\ -11.8 \\ -0.045 \\ -0.018 \\ -0.029 \\ -23.6 \end{bmatrix}. \tag{3.14}$$

As shown in the equations above, the eigenvalues for both controllers all have negative real parts, and thus the closed loop unperturbed system will converge exponentially fast towards the equilibrium states of $\boldsymbol{x}_0$.

3.3.2 Robustness of perturbed system

As the purpose of the system will be to counteract disturbances, the perturbed system, where $||\boldsymbol{E\omega}(t)|| \neq 0$, must be shown to be robust. That is, small disturbances will not result in large steady-state deviations from the equilibrium. The perturbations affecting the vessel are time dependent, and do not stop as the system reaches it's equilibrium point. This means that the perturbations must be seen as non-vanishing. With non-vanishing perturbations we can no longer expected the system to converge at the origin as $t \to \infty$. The best we can hope for is that the system response will be bounded by some small bound, if the disturbance is small, Khalil [2014]. The closed loop perturbed system can be written as

$$\dot{\boldsymbol{x}}(t) = \boldsymbol{A}_{cl}\boldsymbol{x}(t) + \boldsymbol{E}\boldsymbol{\omega}(t) + \boldsymbol{B}\boldsymbol{\beta}. \tag{3.15}$$

The Lyapunov function candidate for the system, $\boldsymbol{V}(x)$, is set as

$$\boldsymbol{V}(\boldsymbol{x}) = \boldsymbol{x}^T\boldsymbol{P}\boldsymbol{x}. \tag{3.16}$$

Differentiating $\boldsymbol{V}(\boldsymbol{x})$ with respect to time will provide an expression for the direction of the trajectory of the system. Thus if $\dot{\boldsymbol{V}}(\boldsymbol{x})$ is negative for all $\boldsymbol{x}$, the system will be stable. $\dot{\boldsymbol{V}}(\boldsymbol{x})$ can be derived as

$$\begin{aligned} \dot{\boldsymbol{V}}(\boldsymbol{x}) =& \boldsymbol{x}^T\boldsymbol{P}\dot{\boldsymbol{x}} + \dot{\boldsymbol{x}}^T\boldsymbol{P}\boldsymbol{x} \\ =& -\boldsymbol{x}^T\boldsymbol{Q}\boldsymbol{x} + \boldsymbol{x}^T\boldsymbol{P}\boldsymbol{E}\boldsymbol{\omega} + \boldsymbol{\omega}^T\boldsymbol{E}^T\boldsymbol{P}\boldsymbol{x} \end{aligned} \tag{3.17}$$

where

$$-\boldsymbol{Q} = \boldsymbol{P}\boldsymbol{A_{cl}} + \boldsymbol{A_{cl}}^T\boldsymbol{P}. \tag{3.18}$$

Equation 3.18 is called the Lyapunov equation. If there exists a solution for the Lyapunov equation where both $\boldsymbol{P}$ and $\boldsymbol{Q}$ are square positive definite matrices, that is $\boldsymbol{P} = \boldsymbol{P}^T > 0$ and $\boldsymbol{Q} = \boldsymbol{Q}^T > 0$, then $\dot{\boldsymbol{V}}(\boldsymbol{x})$ for the unperturbed will be negative, and the system will be stable. Since the system is perturbed, $\boldsymbol{Q}$ must satisfy the inequality shown below.

$$-\boldsymbol{Q} \leq \boldsymbol{P}\boldsymbol{E}\boldsymbol{\omega} + \boldsymbol{\omega}^T\boldsymbol{E}^T\boldsymbol{P} \tag{3.19}$$

Values for $\boldsymbol{P}$ and $\boldsymbol{Q}$ can be calculated from the unperturbed system. Given that the values for the disturbance, $\boldsymbol{\omega}$, are small enough to satisfy the inequality in 3.19, the perturbed closed loop system will produce a bounded response. Lemma 9.2 in Khalil [2014] can be applied as the nominal system has exponential stability about $\boldsymbol{x}_0$, and because the Lyapunov function candidate for the nominal system, chosen in 3.16, satisfy the inequalities 3.20 through 3.22 for $[0, \infty) \times \boldsymbol{D}$, where $\boldsymbol{D} = \{\boldsymbol{x} \in R^n \quad | \quad ||\boldsymbol{x}|| < r\}$. Thus Lemma 9.2 states that the the system response will be bounded by b, following $||\boldsymbol{x}|| \leq b$.

$$c_1||\boldsymbol{x}||^2 \leq \boldsymbol{V}(\boldsymbol{x}) \leq c_2||\boldsymbol{x}||^2 \tag{3.20}$$

$$\frac{\partial \boldsymbol{V}}{\partial \boldsymbol{x}} f(\boldsymbol{x}) \leq -c_3||\boldsymbol{x}||^2 \tag{3.21}$$

$$\left|\left|\frac{\partial \boldsymbol{V}}{\partial \boldsymbol{x}}\right|\right| \leq c_4||\boldsymbol{x}|| \tag{3.22}$$

3.4 Filters

The controller feedback signals are filtered through both a high-pass and a low-pass filter. The low-pass filter aims to remove the components of the signal which stem from the process and sensor noise. The purpose of the high-pass filter is to remove sensor drift.

3.4.1 Low-pass filter

A first order low-pass filter is designed. The filter transfer function can be stated as

$$H(s) = \frac{\omega_0}{s + \omega_0}. \tag{3.23}$$

Here, ω_0 is the cutoff frequency of the filter, and s is the system frequency. s can be rewritten written as $s = j\omega$. According to Balchen et al. [2003], the gain of the filter, and the corresponding phase lag can be calculated as

$$G(j\omega) = |H(j\omega)| = \frac{1}{\sqrt{1 + \left(\frac{\omega}{\omega_0}\right)^2}} \tag{3.24}$$

and

$$\theta(\omega) = -\arctan(\frac{\omega}{\omega_0}). \tag{3.25}$$

The low-pass filter cutoff frequency is set to 5Hz. The smallest wave period we desire to control is $T_p = 5s$. For a wave with this period, the low-pass filter will then create a phase shift of

$$\theta(1/5) = -\arctan(\frac{1}{25}) = -2.29deg. \tag{3.26}$$

The amplitude reduction of $T_p = 5s$ regular waves will be by a factor of $G(0.2) = 0.999$, while the amplitude of noise at 50Hz will be $G(50) = 0.1$. The induced delay is so small as to be assumed non-pertinent with respect to the closed loop system stability. The reduced signal amplitude of the wave frequency with a cutoff at 5Hz is considered negligible. The low-pass filter magnitude response as a function of frequency can be seen in Figure 3.1.

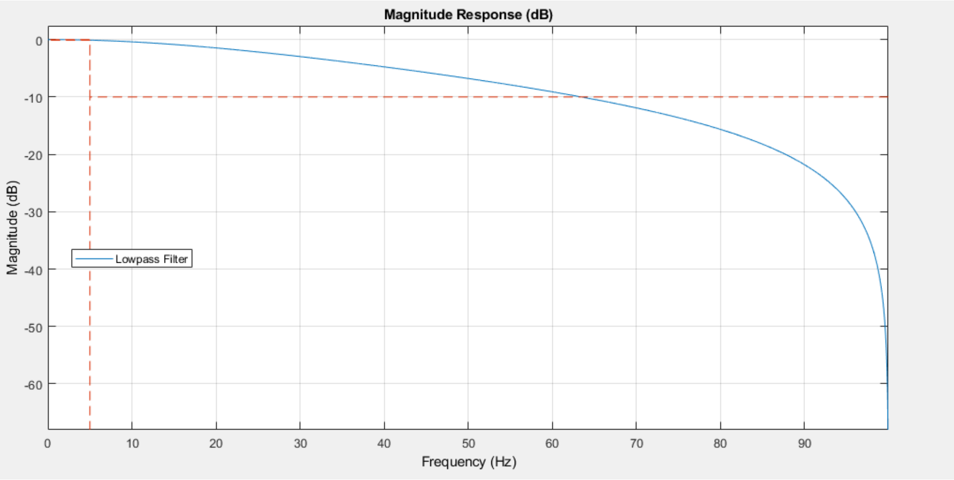

Figure 3.1: Low-pass filter magnitude response as a function of frequency.

3.4.2 High-pass filter

The high-pass filter is relevant only for the accelerometers and gyros. A steady state offset in either of these measurements does not physically make sense. Furthermore a steady offset in these measurements will lead to a drifting error in the heave velocity and roll or pitch angles, which are found through integration of the accelerometer and gyro feedback. The high-pass filter cannot be applied to measurements of position and angles, as a steady state offset here not necessarily is faulty. The transfer function of a first order high-pass filter can be stated as

$$H(j\omega) = \frac{\frac{\omega}{\omega_0}}{1 + \frac{\omega}{\omega_0}}. \tag{3.27}$$

The gain and phase shift caused by the filter can then be expressed as

$$G(j\omega) = \frac{\frac{\omega}{\omega_0}}{\sqrt{1 + \left(\frac{\omega}{\omega_0}\right)^2}} \quad \text{and} \quad \theta(\omega) = \frac{\pi}{2} - \arctan(\frac{\omega}{\omega_0}) \tag{3.28}$$

The largest waves we can expect to encounter will have a period $T_p = 15\text{s}$ or smaller. A rule of thumb states that we can tune the filters such that we remove frequencies which are one third of the maximum expected frequencies. Thus, the high-pass filter cutoff frequency is set to $\frac{1}{15 \times 3} = 0.022\text{Hz}$. The corresponding phase delay for a $T_p = 5s$ wave will then be 5.71 degrees. The filter magnitude response can be seen in figure 3.2.

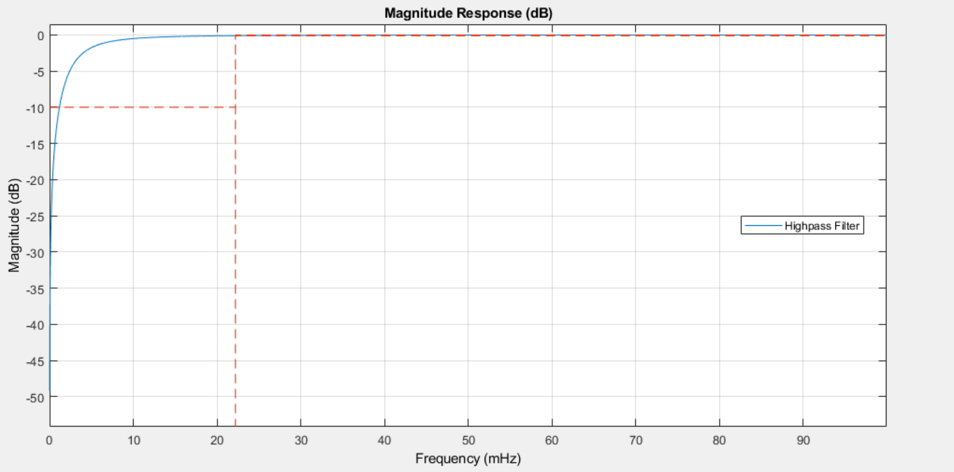

Figure 3.2: High-pass filter magnitude response as a function of frequency.

Chapter 4

Results

This chapter will present the results from heave, roll and pitch control of the four cushion SES in regular and irregular waves. Heave control for the SES is already well documented, and as such the main focus will be on the control of roll and pitch. Some of the tests will however include combined control of both heave, roll and pitch. Results from irregular sea states are presented as *significant height* and *significant angles*. This means that the height/angle represent the expected value of the one third largest heave, roll or pitch displacement. The significant height/angle is calculated through the method expressed in appendix D. As previously stated in chapter 1.7 the data will be normalized, however, these values for significant height and significant angels can be compared to similar values attained from different tests or numerical simulations.

We will present results with waves interacting with the vessel, approaching from different angles. These angles will be referred to as the wave direction, and will be seen as if the vessel heading is unchanged. As an example, a wave direction of $\psi = 180^\circ$ constitutes head sea for the vessel. A wave direction of 0° is following sea, while a wave direction of 90° is beam sea from port side. The simulated and experimental data are scaled after the constants listed in Table 1.1. This is to make a comparison between the scale model tests and numerical simulations possible. Amongst other things, this entails that waves referred to 5 second waves, may show in the plots as having a period of 1.67 seconds.

4.1 Numerical simulations

All the numerical simulations in this sub-chapter are performed with a ventilation valve orifice coefficient of $c_n^{vv} = 0.8$. The cushion separation walls are seen as *solid*, meaning that no amount of air is allowed to penetrate through the walls. Controller 1, discussed in chapter 3.1 will be used for all the numerical simulations in this sub-chapter.

4.1.1 Regular waves - roll control

Regular waves coming from the side of the vessel, also known as beam sea, are simulated to investigate the roll-stabilizing properties of the closed loop controlled system. Several test are performed under the same conditions, but with varying wave periods, T_p, and wave height, H_a. Table 4.1 provides and overview of the waves generated for these tests.

Table 4.1: Wave description

Regular sea	
Wave height, H_a	1 to 2.5 meters
Period, T_p	4 to 12 seconds
Direction, ψ	90°

The comparative results between the controlled and uncontrolled system are displayed in table 4.2. The detailed results for one of the simulations is displayed in Figure 4.1. The first plot in the Figure 4.1 displays the controlled and uncontrolled roll angle for the simulation of 2.5 meters, $T_p = 7s$ waves. The next two plots display the pressure with and without control in two adjacent cushions. The final plot displays the valve openings of the same two adjacent cushions. For the test which is plotted Figure 4.1, the uncontrolled roll has a maximum normalized peak to peak angle of 0.604. The controlled roll for the same case, has a peak to peak angle of 0.0864. This constitutes a 86.5% reduction of the peak to peak roll angle.

Table 4.2: Normalized peak to peak height of roll angle with control OFF/ON

T_p	H_a	η_4-OFF	η_4-ON	Damping
4s	1m	0.609	0.0767	87.4%
5s	1m	0.479	0.0593	87.6%
6s	1m	0.355	0.0461	87.0%
7s	2.5m	0.640	0.0864	86.5%
8s	2.5m	0.500	0.0707	85.8%
9s	2.5m	0.397	0.0600	84.9%
10s	2.5m	0.323	0.0505	84.3%
11s	2.5m	0.268	0.0430	83.9%
12s	2.5m	0.225	0.0386	82.9%

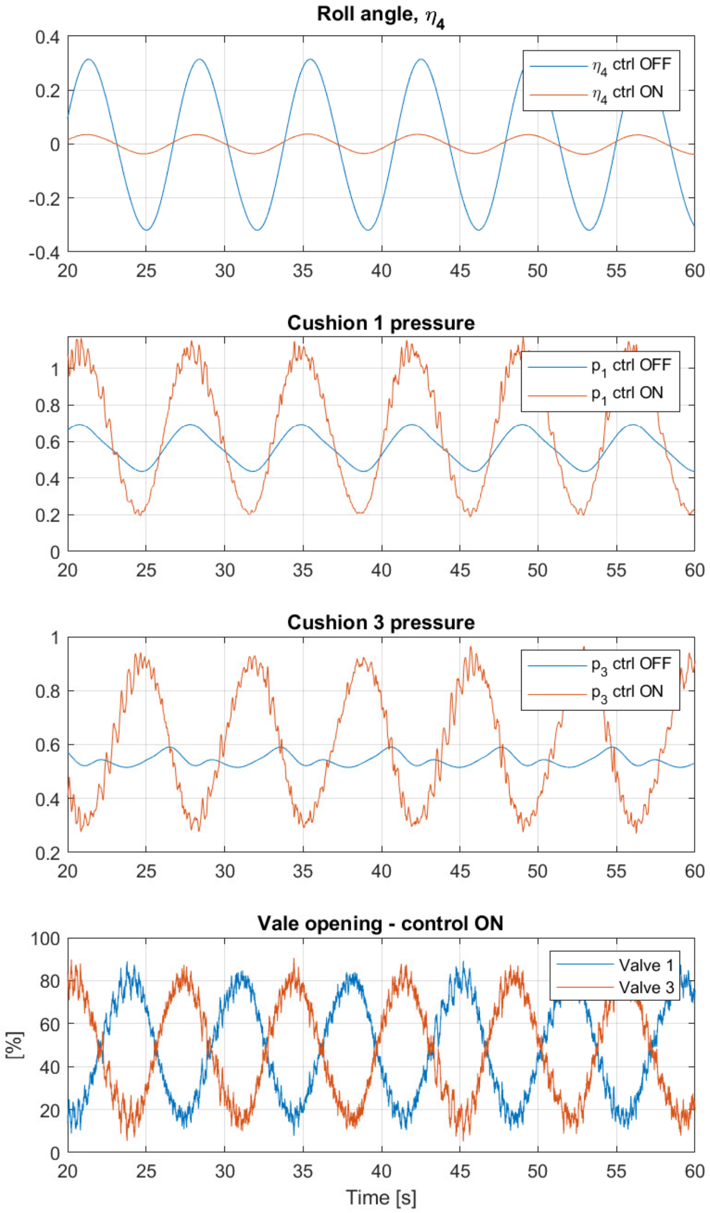

Figure 4.1: Normalized roll angle, cushion 1 pressure, cushion 3 pressure and valve opening for regular, bow sea, 2.5 meter $T_p = 7s$ wave.

4.1.2 Regular waves - pitch control

This sub-chapter present results of numerical simulations where the system is excited with waves described in Table 4.3.

Table 4.3: Wave description

Regular sea	
Wave height, H_a	1 to 2.5 meters
Period, T_p	4 to 12 seconds
Direction, ψ	180°

The pitch properties of the vessel is tested in the same way as the roll. The waves are simulated as regular head sea. The closed loop roll motions of the vessel for one specific wave period and wave height can be seen in Figure 4.2. As with the roll test, table 4.4 shows the overall results from the varying wave heights and periods. The uncontrolled pitch angle in Figure 4.2 has a normalized peak to peak height of 0.541. The controlled pitch for the same case, has a normalized peak to peak angle of 0.121, which constitutes a 77.6% reduction of the peak to peak pitch angle.

Table 4.4: Normalized peak to peak height of pitch angle with control OFF/ON

T_p	H_a	η_5-OFF	η_5-ON	Damping
4s	1m	0.122	0.0305	75.1%
5s	1m	0.254	0.0542	78.7%
6s	1m	0.255	0.0513	79.9%
7s	2.5m	0.541	0.121	77.6%
8s	2.5m	0.450	0.0818	81.8%
9s	2.5m	0.372	0.0660	82.3%
10s	2.5m	0.310	0.0541	82.5%
11s	2.5m	0.261	0.0441	83.1%
12s	2.5m	0.222	0.0394	82.2%

The plot in Figure 4.3 shows the percentile reduction in the peak to peak roll and pitch angles for the simulations stated in this sub-chapter and in sub-chapter 4.1.1. For this plot, the x-axis is the wave period for the waves which excite the roll and pitch motion. The wave height corresponding to these periods are the same as listed in Tables 4.2 and 4.4.

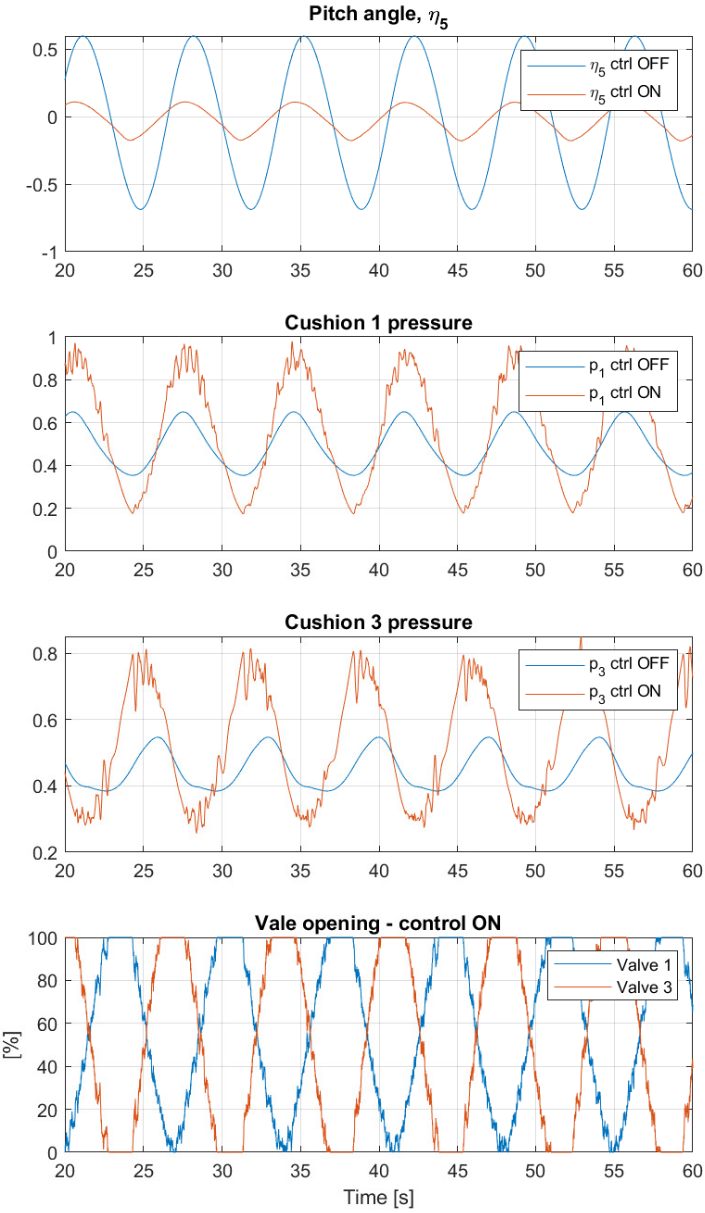

Figure 4.2: Normalized pitch angle, cushion 1 pressure, cushion 3 pressure and valve opening for regular, head sea, 2.5 meter $T_p = 7s$ wave.

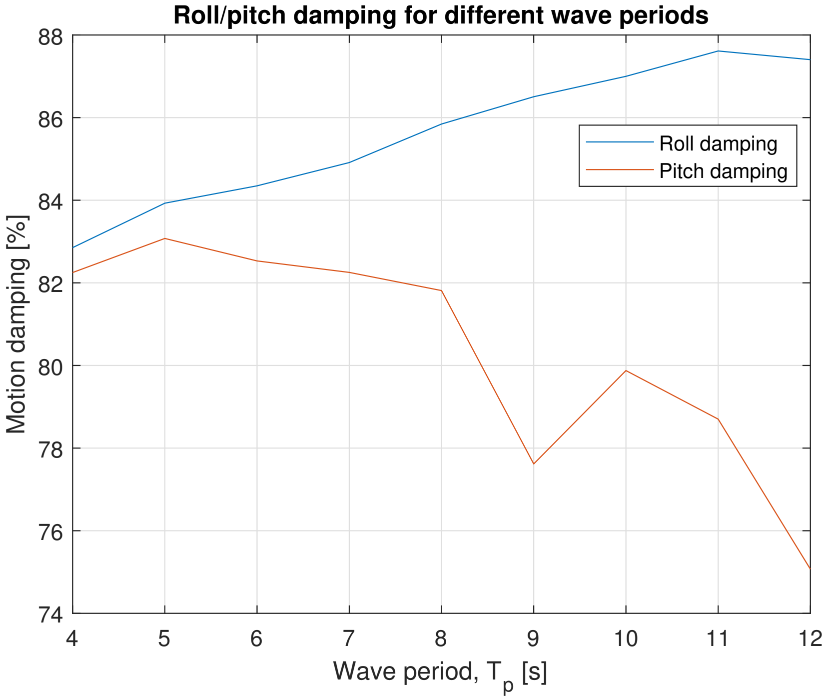

Figure 4.3: Roll and pitch damping percentage in regular waves as a function of the wave period.

4.1.3 Irregular sea - combined roll and pitch control

The sea conditions simulated in this sub-chapter are listed in Table 4.5.

Table 4.5: Wave description

JONSWAP, irregular sea	
Significant height, H_s	2.5 meters
Peak wave period, T_p	Avg. 7 seconds
Wave heading, ψ	$0°$ to $360°$ at $22.5°$ increments
Spectral peakedness, γ	3.3

A total of 18, 500 second long simulations are carried out to verify the damping capabilities of the system in irregular sea. The combined results from all of theses simulations are presented in Figure 4.5. Half of the simulations are with active cushion control, while the other half are without control. The purpose is to test simultaneous control of both roll and pitch in a realistic sea-state, and document the efficacy of the control in various headings. A time series of the roll and pitch motion for beam and head sea, with and without active control can be seen in the plots in Figure 4.4.

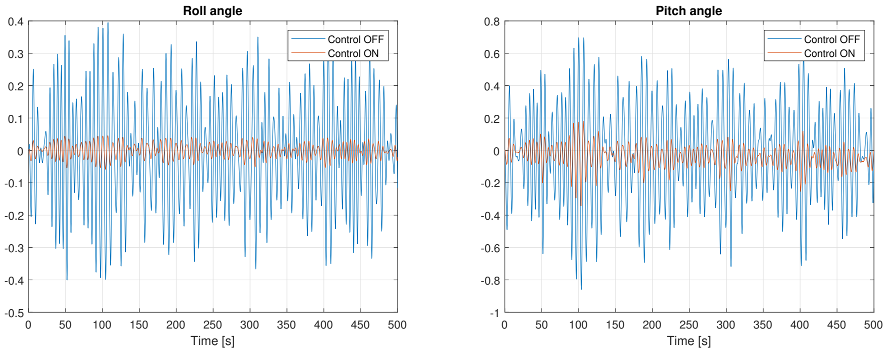

(a) Roll, beam sea.

(b) Pitch, head sea.

Figure 4.4: Time series for normalized roll and pitch angle in irregular beam and head sea.

The polar-plot in Figure 4.5(a) shows the significant angles for the pitch and roll with and without active control. The plot is mirrored about the 0 to 180 degree axis as the vessel is also symmetric around this axis. For wave directions where the excited roll and pitch angles are small, the control system tends to increases the roll or pitch. The increase is minor, and is caused by feedback noise in the controller. The Cartesian plot in Figure 4.5(b) illustrates the percentage damping for each wave direction from 0 to 180.

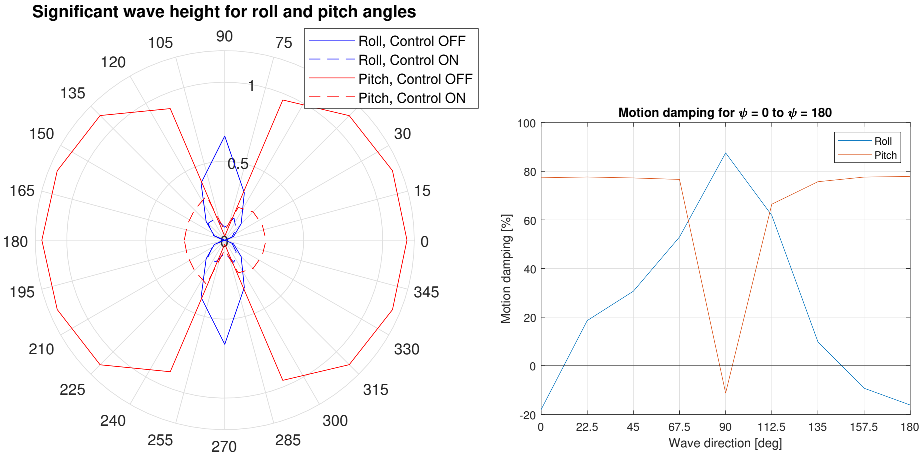

(a) Radial plot of controlled and uncontrolled significant angle for roll and pitch.

(b) Roll and pitch damping percentage.

Figure 4.5: Roll and pitch damping as a function of wave direction.

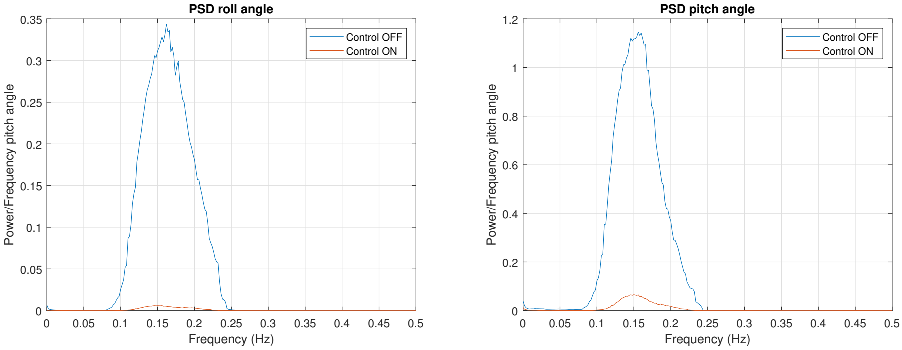

(a) Controlled and uncontrolled roll periodogram.

(b) Controlled and uncontrolled pitch periodogram.

Figure 4.6: Controlled and uncontrolled roll and pitch normalized angle power spectral density.

The combined reduction in significant roll height for the 360 degree wave-direction arch is 57.4%. Similarly, the combined reduction of the significant pitch angle is 75.3%. Figure 4.6 displays the power spectral density (PSD) of the roll angle for beam sea, and pitch angle for head sea, with and without active cushion control.

4.2 Model verification

This chapter will present data from a number of different tests designed to verify the accuracy and validity of the numerical model against the scale model tested in the NTNU wave basin. Though the following sub-chapters, such as chapter 4.3 will also provide useful data for model verification, the plots in this chapter will focus more on comparing the simulated model response with the experimental data, rather than comparing the controlled and uncontrolled motions.

Because of some complications with the feedback of the louver position during the scale model testing, the registered louver position is not completely reliable for many of the tests. The louver position had to be re-calibrated two times during the testing and the registered output relative to the actual louver position may therefore vary from test to test. Figure 4.7 displays the registered louver position, the bias for the same test, and the corrected louver position with respect to bias and initial louver offset. The figure shows that when the adjusted, 'correct', louver opening matches the test bias, $\beta = 75$, the louver position still exceeds a 100% opening, and is limited to a minimum opening of approximately 50%.

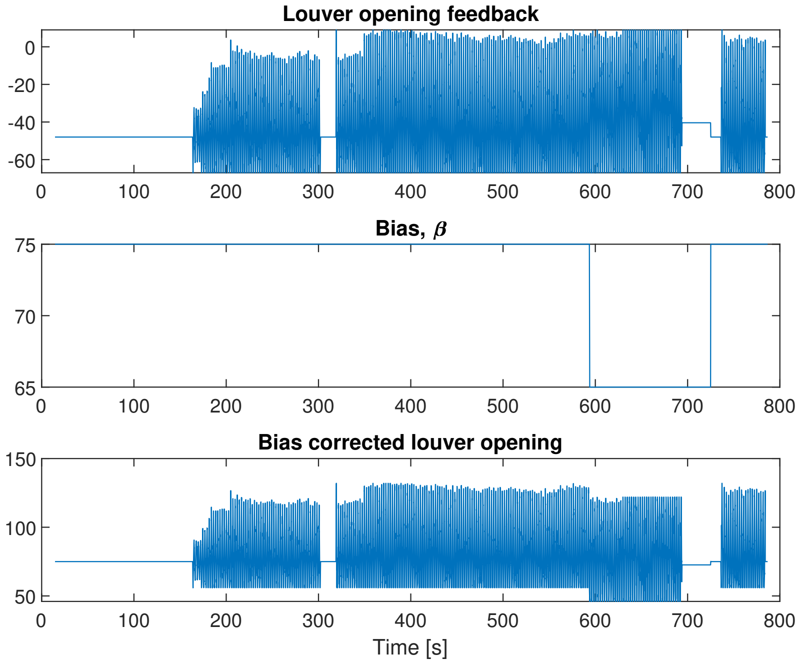

Figure 4.7: Position of the ventilation louvers and corresponding bias.

The initial louver position, or bias, used in each of the scale model test is not necessarily the same as the bias which is registered for the same test. Therefore, comparing the numerical model and the experiments with respect to bias or louver position is not a good solution. We wish to make sure that the bias used in the numerical simulations is as close as possible to the actual bias used for each test. The solution to this is to compare the numerical simulations and the experimental data with respect to average cushion pressure. Before each scale-model test, the vessel remains stationary in the water such that the average cushion pressure without any external excitation forces can be found. During this, the passive leakage is minimal such that the louver position is assumed to correlate directly to the cushion air-flow and thereby to the cushion pressures and vessel heave. Therefore, comparing the two models with respect to average cushion pressure instead of matching bias/louver position is considered to be a reasonable solution to the problem. In the plots where the ventilation valve position is included, the valve position is adjusted such that the average valve position equals the bias position for the test. Because of this, the louver position should be viewed with a sceptical eye in the plots where it is included.

4.2.1 Static heave

Figure 4.8 shows the heave and corresponding average cushion pressure from a simulation and from a scale model test. The purpose of the comparison is to investigate the relationship between the cushion pressure and corresponding heave for the numerical model and the physical scale model. Figure 4.8 displays the average cushion pressure and corresponding vessel heave, when the vessel is lifted from zero pressure to a heave position corresponding to the initial pressure, p_0.

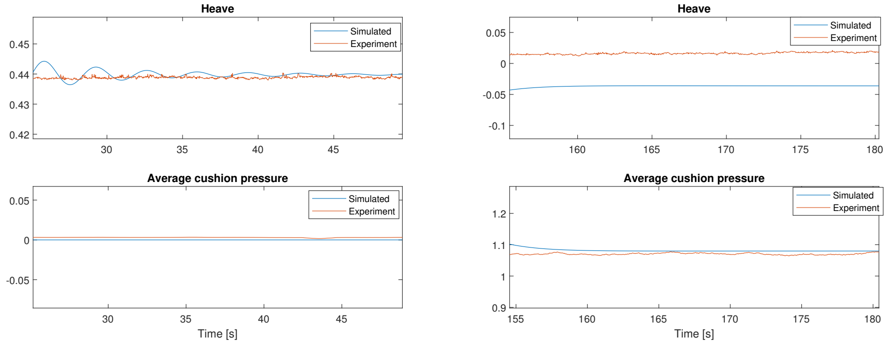

(a) Heave at zero lift, pressure $p_u = 0$

(b) Heave at pressure $p_u = p_0$

Figure 4.8: Pressure and corresponding heave for simulation and experiment.

Note that as previously stated in chapter 2.2, lifting the vessel up from the water, will result in a negative heave. The difference in heave at Figure 4.8(b) is an approximately 12% larger heave motion for the simulation over the experiment, when lifted from zero pressure to p_0.

4.2.2 Static roll

The plot in Figure 4.9 displays the maximum pressure induced static roll angle for the scale model. The purpose of the test is to investigate the relation between pressure and induced roll angle for the simulations compared to the scale model experiments. The roll angle is induced by first fully opening both the port side ventilation valves, while keeping the starboard valves closed. The process is then reversed to create an opposite roll angle. For the simulation, the pressure differential between starboard and port side cushions is matched to the pressure differential attained from the scale model maximum roll angle test.

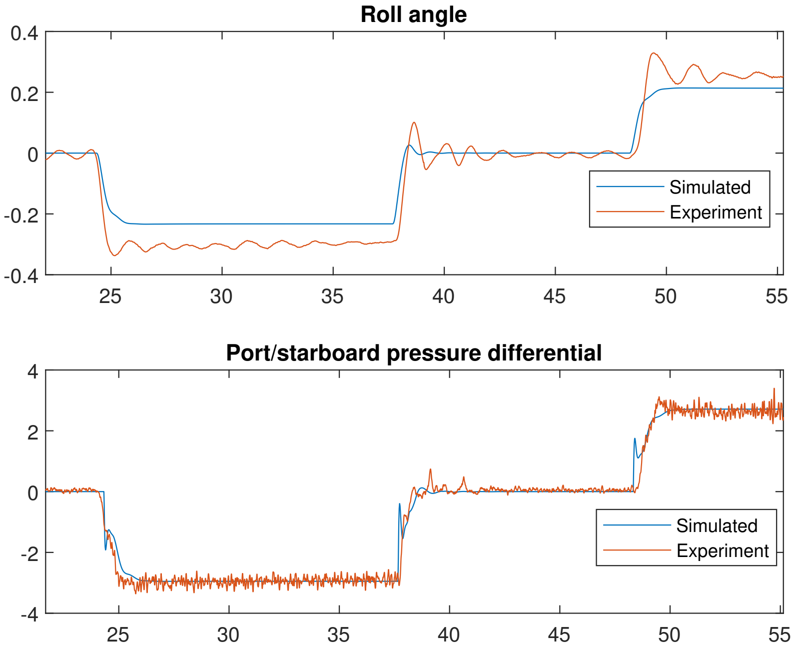

Figure 4.9: Port and starboard pressure differential and corresponding roll angles for simulation and model testing.

The static offset between the simulated roll angle and the roll angle attained during the basin testing, as shown in Figure 4.9, is approximately -22% for the negative roll angle, and -17% for the positive roll angle. As should be clear from Figure 4.9, this means that the numerical simulation creates a 22% and a 17% smaller response in the maximum roll angle than the response attained from the scale model experiments.

4.2.3 Static pitch

As with the heave and roll, the purpose of this test is to investigate the relation between the induced pitch angle and the corresponding cushion pressure. The maximum static pitch angle is achieved by fully opening the front louvers and closing the rear louvers. After a brief period of time, the process is reversed to create an opposite pitch angle. Figure 4.10 shows a comparison of the maximum scale model induced pitch and the simulated induced pitch under the same aft and rear differential cushion pressure. The pitch angle offset between the two models is an approximately 27% larger numerical response for the negative pitch angle, and 17% larger response for the positive pitch angle.

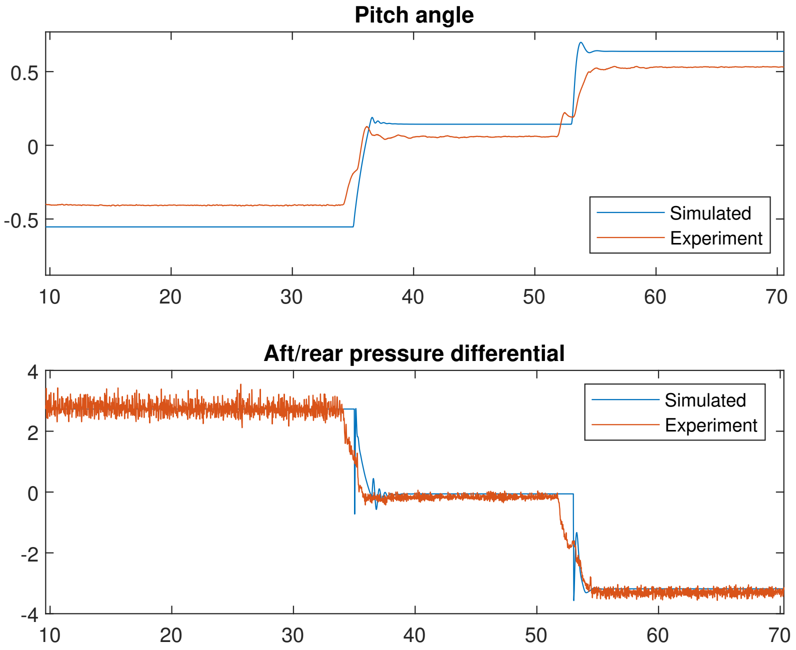

Figure 4.10: Bow and stern pressure differential and corresponding pitch angles for simulation and model testing.

4.2.4 Valve leakage coefficient, c_n^{vv}

Figure 4.11 is a comparison of the average cushion pressure for a numerical simulation and a scale model experiment at a constant 75% valve opening, meaning bias $\beta = 75$. This test is performed shortly after the first louver re-calibration, such that the test bias is assumed to be somewhat closely related to the actual louver opening. The purpose of the test is to investigate and quantify the active leakage from the cushions for the scale model experiments relative to the numerical simulation. To find this relation, we look at the average cushion pressure during the same ventilation valve openings. During this test in the ocean basin, there was no clear leakage from the sides of the hull, such that all air-leakage is assumed to originate from the ventilation valves.

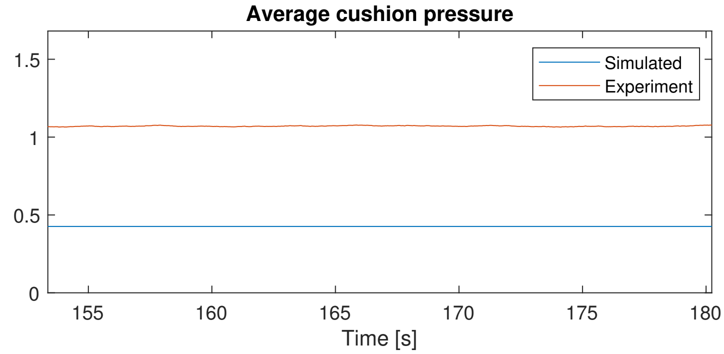

Figure 4.11: Average cushion pressure for simulation and experiment with bias $\beta = 75$ and $c_n^{vv} = 0.8$.

Figure 4.12 shows the same experimental data, but with a different ventilation duct orifice coefficient, c_n^{vv}, for the numerical simulation.

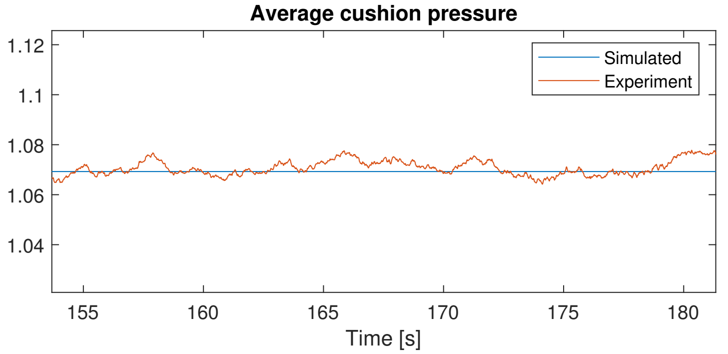

Figure 4.12: Average cushion pressure for simulation and experiment with bias $\beta = 75$ and $c_n^{vv} = 0.4543$.

4.2.5 Non-solid walls

Figure 4.13 shows a comparison of two simulations from the numerical model and data from a scale model test. The vessel is excited by regular, 1 meter 5 second head sea waves. In Figure 4.13(a) the numerical simulation uses the assumption of *solid walls*, which means that no air is allowed to penetrate through the cushion dividers. For the numerical simulation with non-solid walls in Figure 4.13(b), a small fixed percentage of the cushion dividers are modeled as an open leakage area such that some inter-cushion leakage will occur. These numerical simulations are conducted with $c_n^{vv} = 0.8$, and a bias which results in a similar average cushion pressure for the simulation and the experimental data.

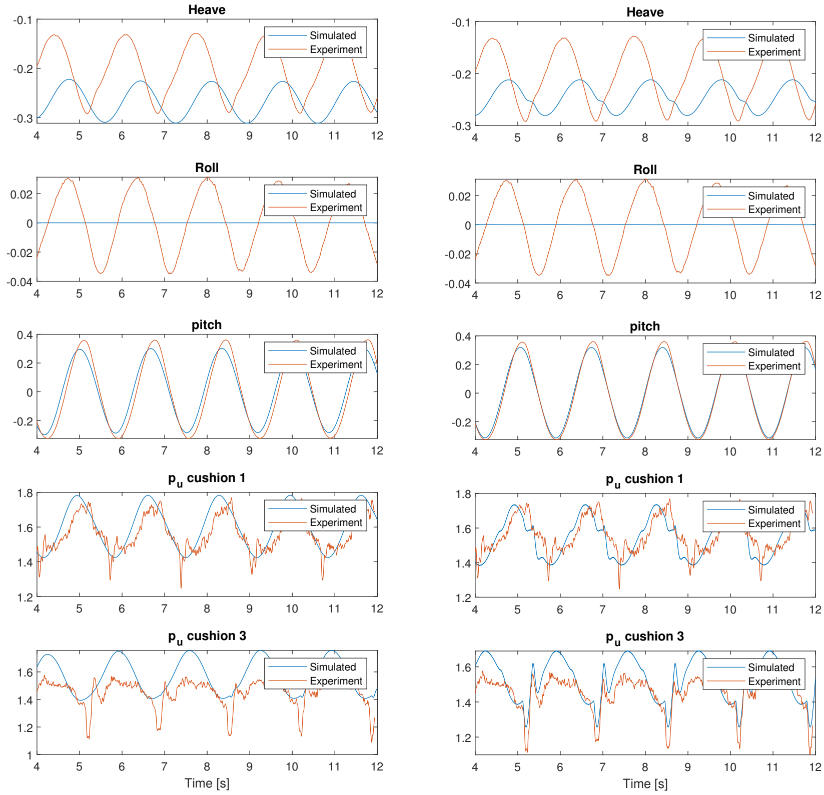

(a) Solid walls.

(b) Non-solid walls.

Figure 4.13: Vessel dynamics and pressure for regular head sea, $\psi = 180°$. Wave height 1 meter, wave period 5 seconds.

4.3 Scale model experiments

This sub-chapter will present data from the scale-model experiments, and will focus on the efficacy of the roll and pitch damping. Data generated from the numerical model under the exact same conditions as the scale model tests will be presented alongside the data from the experiments. The numerical model which is compared to the scale model experiments in this sub-chapter uses a ventilation duct orifice coefficient of $c_n^{vv} = 0.58$. It also uses a minor, fixed, inter cushion leakage area, to emulate the non-solid walls of the scale model. Controller 2, from chapter 3 is used for all the experimental tests and numerical simulations in this sub-chapter. As explained in chapter 3, the controller bias and the controller gains will vary from test to test. The controller gains used in the numerical simulations match the controller gains which are used for each of the different scale model tests. The bias is generally close to the bias used during the testing, but as mentioned in chapter 4.2, the ventilation valve opening corresponding to this bias is not completely reliable for the scale model. Therefore, the bias in the numerical simulations is altered to generate the same average cushion pressure as that registered in the relevant scale model test. The scale model is tested for to two different types of regular waves coming from three different wave directions. Following this, the scale model is tested in irregular sea, generated after the JONSWAP spectra. The response in irregular sea is tested over 5 different wave directions, from $\psi = 180$ to $\psi = 0$.

4.3.1 Regular waves - 1 meter

The specifications for the first type of regular waves is listed in Table 4.6.

Table 4.6: Wave description

Regular sea	
Wave height, H_a	1 meters (peak to peak)
Period, T_p	5 seconds
Direction, ψ	180°, 135° and 90°

Figure 4.14 shows the controlled and uncontrolled roll and pitch response for regular waves coming as bow sea, $\psi = 135°$. The plots also show a comparison to the numerical results from a simulation performed with the same conditions. The figure shows that the controlled response is substantially smaller than the uncontrolled response. The normalized peak to peak height for the uncontrolled roll form the experimental testing is 0.187. The same controlled roll motion has a normalized peak to peak height of 0.0514, constituting a 72.5% reduction. Table 4.7 show the exact normalized peak to peak roll and pitch angle for each of the wave directions. The simulated peak to peak roll angle averaged over the three wave directions, is 28.5% smaller than the roll angles obtained from the scale model experiments. For the pitch angle, the average simulated peak to peak angle is 5.8% smaller than the pitch angle from the scale model experiments. Note that the error is very large for the small pitch and roll angles at 90° and 180°, respectively. For the controlled motion, the equivalent numbers show a 11% smaller average simulated roll angle and a 12.8% smaller simulated pitch.

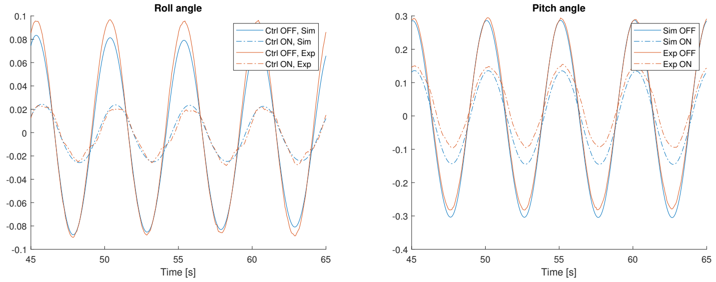

(a) Roll motion.

(b) Pitch motion.

Figure 4.14: Controlled and uncontrolled pitch and roll for 1 meter, 5 second bow sea ($\psi = 135°$).

Figure 4.15(a) shows a comparison of the uncontrolled numerical simulation and the data generated from the experiments. Figure 4.15(b) shows the same comparison for the controlled case. Note that for the controlled case, the heave decreases for the scale model vessel. This is due to a 15% increase in the average cushion pressure when the vessel motions are controlled.

Table 4.7: Experiment data, regular 1 meter, $T_p = 5s$ waves. Peak to peak angle for roll and pitch with control OFF/ON.

	Roll experiment			Roll simulation		
ψ	η_4-OFF	η_4-ON	Damping	η_4-OFF	η_4-ON	Damping
180°	0.0455	0.0594	-30.5%	0.0001	0.0001	3.35%
135°	0.187	0.0514	72.5%	0.175	0.0509	70.9%
90°	0.690	0.161	76.7%	0.542	0.193	64.4%

	Pitch experiment			Pitch simulation		
ψ	η_5-OFF	η_5-ON	Damping	η_5-OFF	η_5-ON	Damping
180°	0.568	0.189	66.8%	0.605	0.228	62.3%
135°	0.581	0.256	56.0%	0.594	0.281	52.6%
90°	0.121	0.140	-15.3%	0.0097	0.0095	1.96%

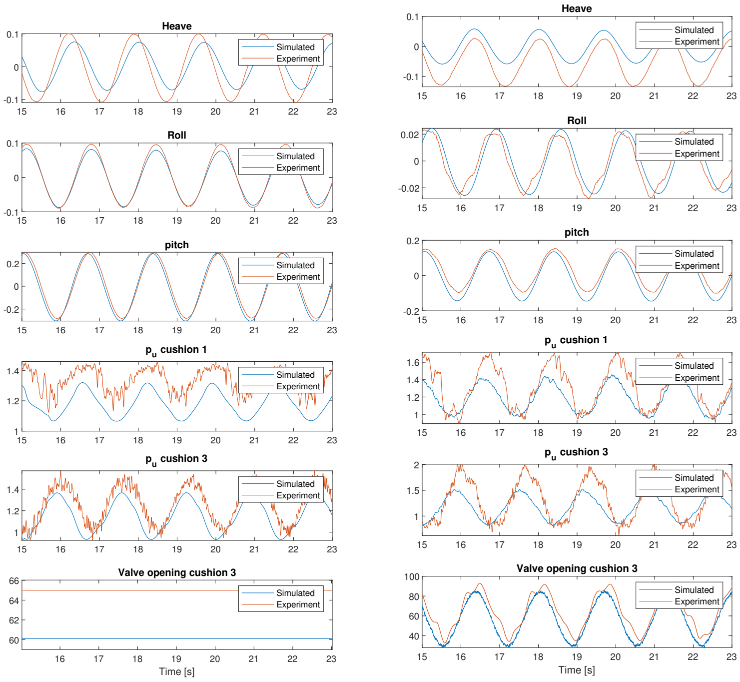

(a) 1 meter bow sea, control OFF.

(b) 1 meter bow sea, control ON.

Figure 4.15: Controlled and uncontrolled vessel dynamics and pressure for 1 meter, 5 second bow sea ($\psi = 135°$).

4.3.2 Regular waves - 2.5 meter

As with the 1 meter waves, the vessel is subjected to regular waves specified in Table 4.8.

Table 4.8: Wave description

Regular sea	
Wave height, H_a	2.5 meters (peak to peak)
Period, T_p	7 seconds
Direction, ψ	180°, 135° and 90°

Figure 4.16 shows the controlled roll and pitch compared to the uncontrolled roll and pitch for $\psi = 90°$ and $\psi = 180°$ respectively. The uncontrolled numerical roll and pitch angles are respectively, 7% smaller and 2% larger than the scale model experiment peak to peak roll and pitch angles. With active cushion control, the difference is a 1% smaller peak to peak angle for the simulated roll, and 9% larger angle for the simulated pitch when compared to the experimental data. Table 4.9 shows the exact peak to peak angle height and damping percentage for each test. The roll damping for the scale model experiments in Figure 4.16(a) is 62.1%. The pitch damping in head sea in Figure 4.16(b) is 66.4%.

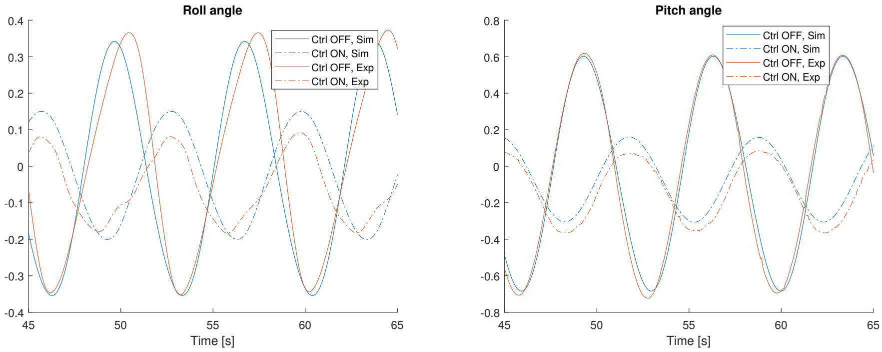

(a) 2.5 meter beam sea.

(b) 2.5 meter head sea.

Figure 4.16: Simulation and experiment pitch and roll with and without cushion control for 2.5 meter, 7 second beam and head sea.

The uncontrolled heave, roll and pitch response for the model and the simulation in Figure 4.17 show that the heave motions are reduced by 6% for the numerical simulations in head sea and a 8% in beam sea. The uncontrolled pitch motions are 6.5% larger for the simulation than for the experimental data during head sea, while the uncontrolled roll motions are 6.5% smaller for the numerical simulation in beam sea. In the controlled response in Figure 4.18 only the roll and pitch motions are controlled. For this plot, the valve opening registered from the experiments is adjusted such that the average valve opening matches the bias that is registered for the relevant experiment.

Table 4.9: Experiment data, regular 2.5 meter, $T_p = 7s$ waves. Peak to peak angle for roll and pitch with control OFF/ON.

	Roll experiment			Roll simulation		
ψ	η_4-OFF	η_4-ON	Damping	η_4-OFF	η_4-ON	Damping
180°	0.0650	0.0681	-4.90%	0.0001	0.0001	-2.64%
135°	0.439	0.164	62.8%	0.320	0.102	67.7%
90°	0.741	0.281	62.1%	0.696	0.351	49.6%

	Pitch experiment			Pitch simulation		
ψ	η_5-OFF	η_5-ON	Damping	η_5-OFF	η_5-ON	Damping
180°	1.34	0.451	66.4%	1.29	0.468	63.6%
135°	0.950	0.424	55.4%	1.18	0.605	48.9%
90°	0.0776	0.0952	-22.9%	0.0220	0.0160	28.7%

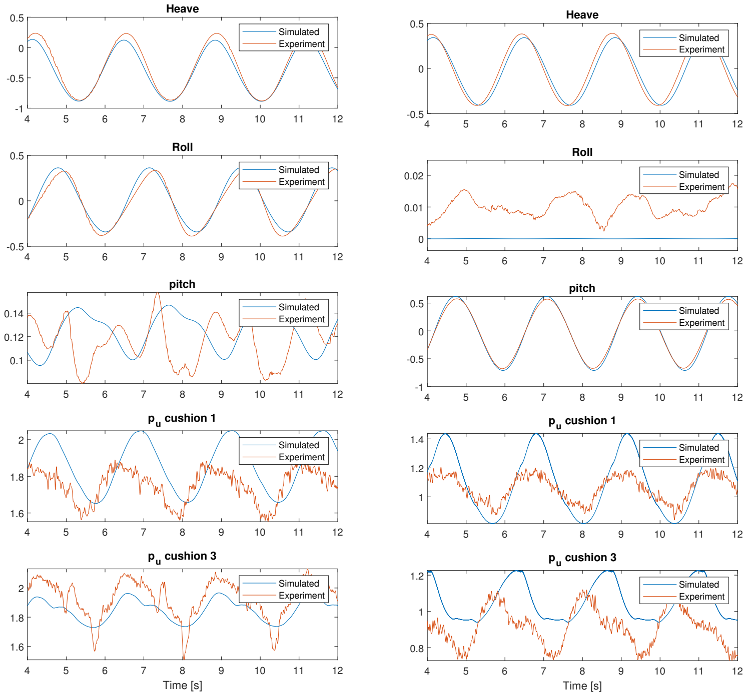

(a) 2.5 meter beam sea.

(b) 2.5 meter head sea.

Figure 4.17: Uncontrolled vessel dynamics and pressure for 2.5 meter, 7 second beam and head sea.

The results from Table 4.9 show that the simulated peak to peak roll angle averaged over the three wave directions, is 22.4% smaller than the roll angles found from the experiments. For the pitch angle, the average simulated peak to peak angle is 5.0% larger than the pitch angle from the scale model experiments. For the controlled motion, the same numbers are 13% smaller simulated roll and 11% larger for the simulated pitch.

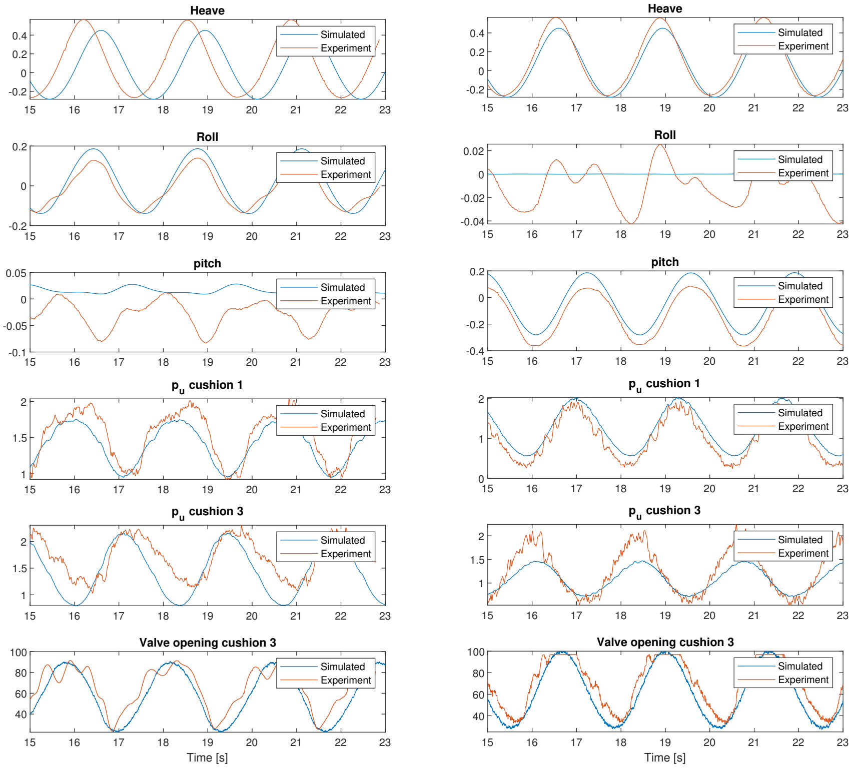

(a) 2.5 meter beam sea.

(b) 2.5 meter head sea.

Figure 4.18: Controlled vessel dynamics and pressure for 2.5 meter, 7 second beam and head sea.

4.3.3 Irregular waves

Table 4.10: Wave description

JONSWAP, irregular sea	
Significant height, H_s	2.5 meters
Peak wave period, T_p	Avg. 7 seconds
Wave heading, ψ	180° to 0° at 45° increments
Spectral peakedness, γ	3.3

The vessel is subjected to the sea state listed in Table 4.10. A total of 10 tests for irregular sea are carried out, 5 with and 5 without active cushion control. The gains for the controllers are found through tuning during the regular wave experiments. The gains vary slightly from heading to heading, but remain unchanged for each test once the test is started. In addition, not all states are controlled for all headings. Table 4.11 show which modes of control are active at which headings. An irregular sea state can be considered as a combination of random wave heights and patterns within a set distribution. The wave pattern generated for the irregular sea which is used in the wave basin experiments is the exact the same for the tests with and without control. I.e. the exact same randomization seed and method of random number generation is applied for both cases. The sea conditions are the same for the numerical simulations as during the experiments, however, the generated random sea pattern is not the same. As with the wave basin experiments, the generated random sea pattern for the numerical simulations is the exact same for the simulations with control as for the simulations without control. Through the calculation of significant height as explained in appendix D, the actual significant height of the random wave pattern generated in the numerical simulations is found to be 2.17 meters. The results from Table 4.12 reflect these findings, as the numerical vessel response is consistently smaller than the response generated in the experiments.

Table 4.11: Modes of control for each heading.

Heading [deg], ψ	Heave	Roll	Pitch
180°	x		x
135°		x	x
90°	x	x	
45°	x	x	x
0°	x		x

Figure 4.19 shows a 500 second snapshot from the time series for roll and pitch, for the scale-model with and without active cushion control activated. The time series for the roll motion is taken during beam sea, $\psi = 90°$. The time series for the pitch motion is taken at head sea, $\psi = 180°$. The plots in Figure 4.20 show the equivalent plot generated from the numerical simulations.

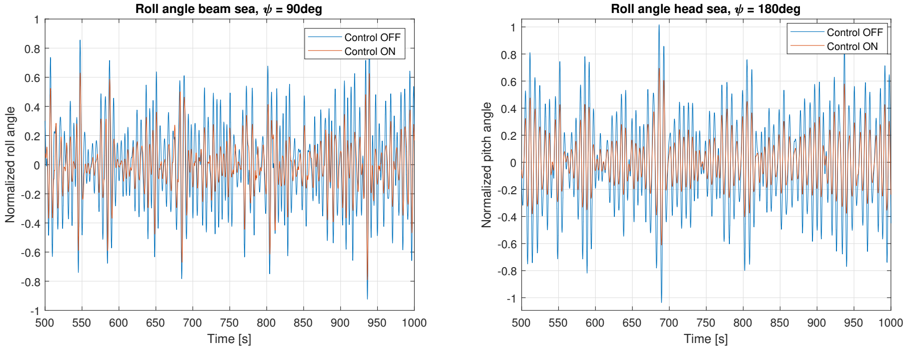

(a) Beam sea roll motion

(b) Head sea pitch motion

Figure 4.19: Snapshot of time series for roll and pitch motion in irregular sea for scale model experiments.

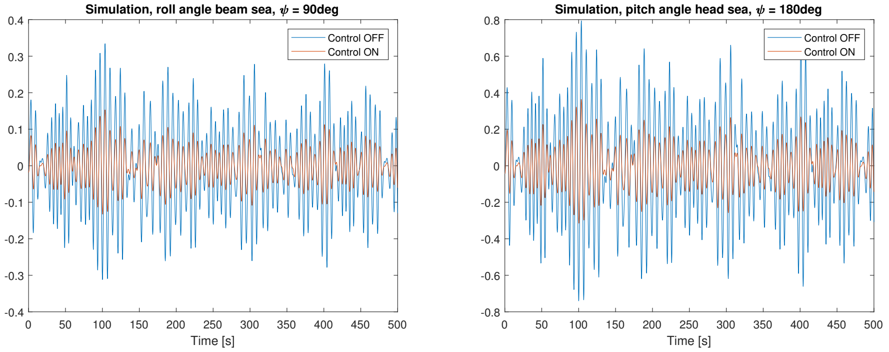

(a) Beam sea roll motion

(b) Head sea pitch motion

Figure 4.20: Snapshot of time series for roll and pitch motion in irregular sea for numerical simulation.

The plots in Figure 4.21 show the normalized significant heave motion, and the normalized significant roll and pitch angles for different wave headings. The plots are mirrored around the half-circle from 180° to 0°. Note that, as shown in Table 4.11, the heave motion is not controlled at 135°.

The exact values for the motion damping percentage and the significant height/angle for each wave direction is listed in Table 4.12. This table also contains comparative data from the numerical simulations with the same controller gains, and under the same irregular sea conditions. Figure 4.22 shows two periodogram estimates of the spectral functions of the roll and pitch angles in beam and head sea for the wave basin experiments.

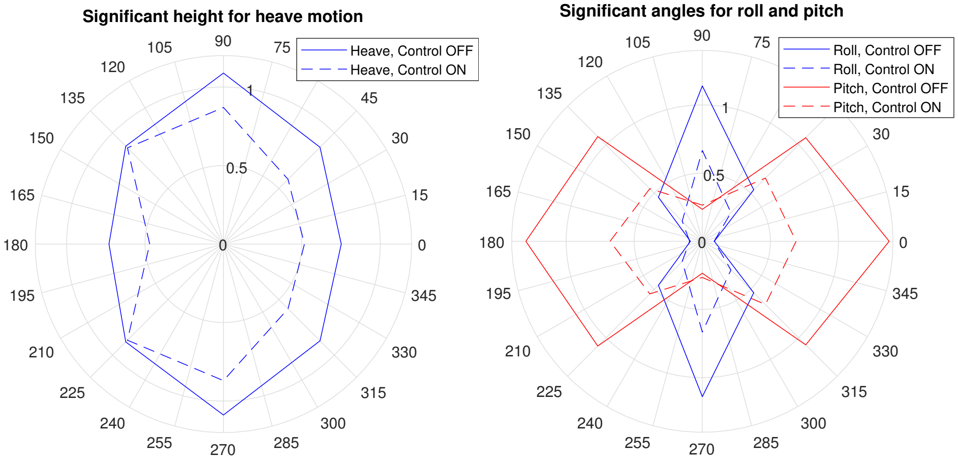

(a) Significant heave height. **(b)** Significant angle of roll and pitch motion

Figure 4.21: Radial plot of the significant heave, roll and pitch motion for scale-model experiments.

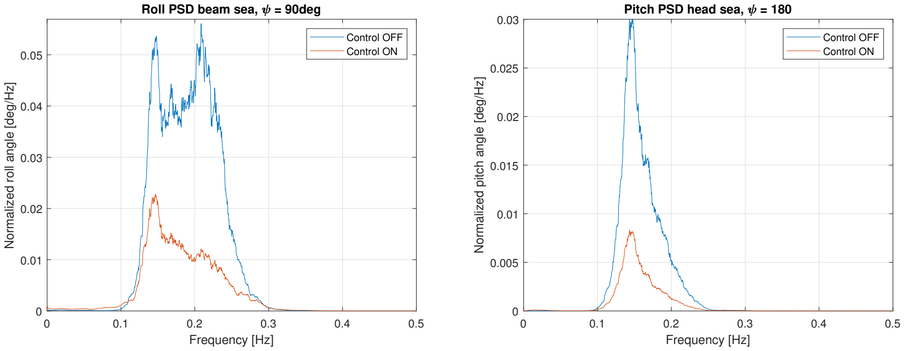

(a) Beam sea, PSD for roll. **(b)** Head sea, PSD for pitch

Figure 4.22: Power spectral density for roll and pitch motion in irregular sea, for wave basin experiments.

Figure 4.23 is a comparison of the heave, roll and pitch damping achieved in the wave basin experiments and in the numerical simulations. This plot is based on the damping percentages show in in Table 4.12.

Table 4.12: Experiment data, irregular waves. Significant height for heave, and significant angles for roll and pitch, with control OFF/ON.

	Heave experiment			Heave simulation		
ψ	η_{3s}-OFF	η_{3s}-ON	Damping	η_{3s}-OFF	η_{3s}-ON	Damping
180°	0.730	0.470	35.6%	0.598	0.351	41.2%
135°	0.881	0.866	1.76%	0.643	0.628	2.30%
90°	1.09	0.869	20.1%	0.875	0.585	33.1%
45°	0.871	0.582	33.1%	0.658	0.396	39.9%
0°	0.751	0.516	31.3%	0.618	0.371	39.9%

	Roll experiment			Roll simulation		
ψ	η_{4s}-OFF	η_{4s}-ON	Damping	η_{4s}-OFF	η_{4s}-ON	Damping
180°	0.087	0.093	-6.88%	0.0001	0.0001	0.283%
135°	0.456	0.209	54.2%	0.195	0.113	42.3%
90°	1.14	0.666	41.5%	0.729	0.327	55.1%
45°	0.534	0.297	44.4%	0.150	0.0883	41.0%
0°	0.088	0.087	1.27%	0.0001	0.0001	4.05%

	Pitch experiment			Pitch simulation		
ψ	η_{5s}-OFF	η_{5s}-ON	Damping	η_{5s}-OFF	η_{5s}-ON	Damping
180°	1.30	0.678	47.7%	1.16	0.568	50.8%
135°	1.09	0.545	49.8%	1.09	0.505	53.7%
90°	0.234	0.265	-13.2%	0.0242	0.0258	-6.20%
45°	1.07	0.655	39.0%	1.10	0.468	57.6%
0°	1.37	0.688	49.8%	1.14	0.443	61.2%

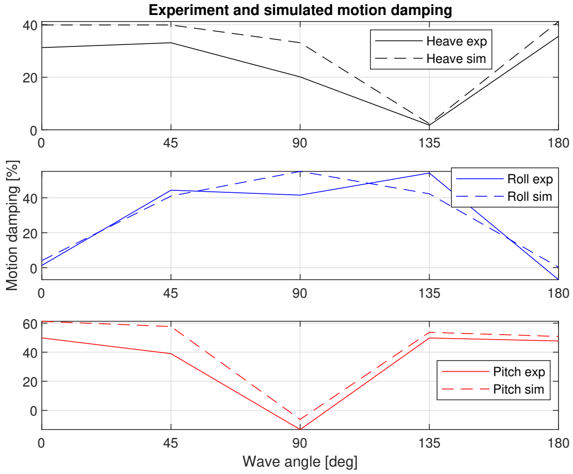

Figure 4.23: Percentage motion damping, irregular sea, experimental data and numerical simulation.

Chapter 5

Discussion

5.1 Model Verification

In this sub-chapter, the experimental data is analyzed and compared to data gathered form the numerical model developed in chapter 2. We attempt to do a step by step comparison of the numerical simulation results against the experimental scale model results. The goal is to verify and document the validity and accuracy of the mathematical model. Further, we try to identify the differences in the two models, and address how the mathematical model can be altered to mitigate these differences.

5.1.1 Pressure - heave relation

The results from the static heave response, Figure 4.8 in chapter 4.2.1, show that when the vessel is lifted from zero pressure to the initial pressure p_0, the same pressures generate an approximately 12% larger heave response for the simulation compared the experiment. Following equation (2.84) we see that when the vessel heave is constant, the heave forces acting on the vessel can be stated as

$$gm = F_{c_3} + F_{h_3}. \tag{5.1}$$

Here gm constitutes the gravitational force, F_{c_3} the heave cushion forces and F_{h_3} the hydrodynamic heave forces from the hull, which are computed from the hydrodynamic constants discussed in 2.12. From the equation above, we can say that the difference in heave can stem from three possible errors.

- **Mass:** The mass of the scale model might be slightly larger than that of the simulation, causing the gm term to be larger than anticipated for the scale model. A possible physical reason for this discrepancy is water-leakage. During the model testing the scale model had to be drained of water two times. However, the amount of water drained was not much, and this effect alone should not amount to a 12% discrepancy.

- **Pressure area:** The cushion forces, term F_{c_3} in equation (5.1), may be smaller than anticipated due to a decreased pressure area. From chapter 2.11 we know that the cushion forces can be calculated as the pressure times area. It is possible that the pressure area for each cushion is smaller than expected due to the area occupied by the separation walls and the thickness of the hull. On the other hand, these walls will provide a lift force equal to or greater than the cushions them-self, as the pressure inside the separation walls will be higher than that inside the cushions.

- **Hydrodynamic constants:** The hydrodynamic constants used in the numerical model can never be completely accurate. As previously stated in chapter 2, the hydrodynamic properties of the vessel are handled by the MSS library, [Fossen and Perez 2004]. This library is dependant on input values for A_{33}, B_{33} and C_{33} as briefly addressed in chapter 2.12. These values are provided by Umoe Mandal, and are calculated to be accurate at the heave level corresponding to the initial pressure p_0. Therefore, at heave-levels and pressures not corresponding to pressure $p_u = p_0$ these constants may no longer serve as accurate approximations. For equation (5.1) this means that the term F_{h_3} may become too large in the numerical model.

5.1.2 Pressure - roll/pitch relation

From the test in chapter 4.2.2, and from Figure 4.9, the difference in the induced static roll angle is found to be an approximately 22% smaller angle for the negative numerical roll angle, and 17% smaller angle for positive roll. As with the heave-pressure relation, we can say that there are no external excitation forces acting on the vessel during this test. By then applying equation (2.85), there are two possible reasons for the observable steady state offset. Firstly, the pressure area might be not be correct. Secondly, the hydrodynamic roll restoring force C_{44}, might be too large for the simulation compared to the scale model test. The distances from the center of rotation to the different centers of pressure for the cushions are assumed to be the same for the numerical model and the scale-model.

The static pitch response can be seen in chapter 4.2.3, Figure 4.10. This graph shows that when the pressure differential between the front and aft cushions are the same for the numerical model and the scale model, the resulting induced pitch angle gives an approximately 27% larger response in the numerical model for negative pitch. For positive pitch, the results show an approximately 17% larger numerical response compared to the results from the scale model tests. Similar to the static heave and roll, equation (2.86) illustrates that the offset could be due to a reduced pressure area for the scale model relative to the pressure area in the numerical model. Also similar to the roll angle offset, another possible effect is that the real restoring coefficient C_{55} for the scale model is larger than the one which is applied in the numerical simulation. As previously stated, these hydrodynamic coefficients are calculated around p_0 and will only be good approximations for small angles and movements around this equilibrium. In addition, the correct restoring coefficient for the scale model might also be larger than anticipated due to the buoyancy of the center cushion divider seen in Figure 1.10. The buoyancy from this divider will create a restoring-force similar to that of a pressurized cushion. Though the same will be true for the transverse cushion dividers, the center cushion divider is a lot larger and will create a larger buoyancy force. In addition, the distance from the center of rotation is larger for pitch motions. This results in a larger arm for the restoring moments. The increased distance from the center of buoyancy will also mean that smaller pitch angles will force the center bag further down in the water, causing yet a larger buoyancy force and an increased restoring moment relative to the transverse dividers.

5.1.3 Cushion air flow

By using the results in chapter 4.2.4 and 4.2.5, we wish to quantify the air-flow out from the cushions in the numerical simulation relative to the scale model experiments. As previously discussed in sub-chapter 2.10, the air flow in the cushion can be divided into active and passive leakage.

Active leakage

As discussed in depth in chapter 2.10.2, active leakage only concerns the air-flow out from the ventilation valves. In the test in chapter 4.2.4 the louver opening is assumed to be the same position for the simulation and for the model. However, due to the inconsistencies in the registered louver position, this might not be an accurate assumption. Passive leakage from the model is largely followed by a spray of water. An example of this can be seen from the picture in Figure 1.8. None, or only negligible passive leakage could be observed at this given heave position during the experiment. Therefore we assume that virtually all of the air leakage from the cushions are due to active leakage. Since the vessel is not affected by any external excitation forces, and the louver positions are constant, we can assume both constant cushion pressures and constant cushion volumes. The equation for the non-linear cushion pressure, (2.54), can then be rewritten as

$$0 = \frac{\gamma(p_a + p_{u_i})}{V_{c_i}} \left(\left(\frac{p_a}{p_a + p_{u_i}} \right)^{\frac{1}{\gamma}} \left(Q_{in_j}(t) - Q_{out_j}(t) \right) \right). \tag{5.2}$$

From this equation we can see that any steady state error in the cushion pressure must come from either the relationship of the volume flow into the cushion against the flow out of the cushion, or from a difference in the cushion volume. From Figure 4.11 we can see that there is a large discrepancy in the pressure for the simulation and the experiment. We assume that the positive air flow into the cushions, caused by the lift fans, is the same for the experiment and the simulations. Since the air flow out from the ventilation valves can be described as shown in equation (2.69), the corresponding discrepancy in the volume flow out from the cushions is likely to stem from at least one of three factors.

- **Louver position:** As mentioned in chapter 4.2, during the testing some technical difficulties occurred with respect to the louver positions. Though the feedback from the louvers read that they were in a certain position, it was clear from visual inspections and from the measured cushion pressures that their registered position was faulty.
- **Obstructed flow:** From chapter 4.3.1 and Figure 4.15, we observed a 15% increase in the average cushion pressure from the test without active cushion control to the test with cushion control. We also observed that some sea states caused a slight

increase in the average cushion pressure when compared to the initial calm water measurements. There are a few possible reasons for this. Firstly, we know that there are some nonlinearities with respect to the ventilation valve leakage area. The louver opening is seen as a 0-100 percentage opening of the maximum valve duct area. However, in reality, the projected leakage area from the louver opening will be a sine function of the angle of the ventilation louvers. This means that when the louvers are moving evenly around a set bias, a 10 degree increased louver opening might result in a 14% increased leakage area, while a 10 degree reduction in the louver opening might result in a 17% decreased leakage area. Therefore the leakage will not be symmetric around the average, bias opening, which will cause an increase in the average cushion pressure. Another possibility is that the louver opening is saturated in one direction. In example, this could mean that from the bias position, the louvers can rotate to close 60 degrees, but only open another 30 degrees. A third possibility is that different sea states act to obstruct the flow through the louvers in different ways, causing an increase in the average cushion pressure. Due to time limitations, and technical difficulties with the registered louver position relative to the actual louver position, neither of these theories can be confirmed or excluded.

- **Effective valve area:** The effective active leakage area is the projected opening onto the ventilation duct where the air flow unobstructed. The louvers effectively take up a lot of the leakage area from the ventilation duct, even when they are completely opened. The effect of this is illustrated in Figure 5.1, which shows the ventilation duct with fully opened ventilation louvers. Through the use of AutoCAD®, and the picture in Figure 5.1, the effective valve leakage area is estimated to be only 61.5% of the total duct area.

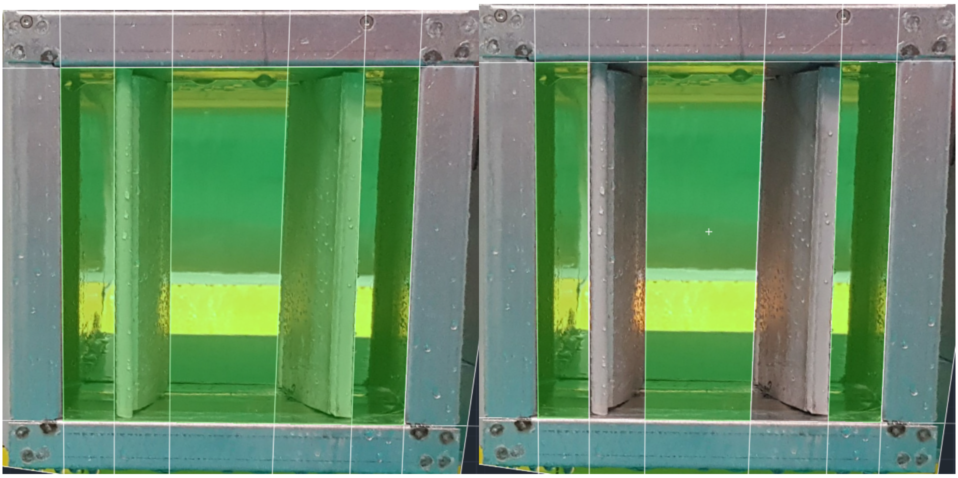

(a) Total ventilation duct leakage area.

(b) Effective ventilation duct leakage area

Figure 5.1: Fully open ventilation valves. Green colored area displays the area which is registered by AutoCAD® for estimation of effective leakage area.

This last effect mentioned in the bullet points above is linear and can therefore be incorporated into the leakage coefficient for the ventilation duct, c_n^{vv}. The initial value for the ventilation valve leakage coefficient is set to $c_n^{vv} = 0.8$. We wish to find an updated estimate for this coefficient. Assuming that the vessel has zero roll and zero pitch, we know from chapter 5.1.1 that the pressure relates closely to the heave of the vessel. Because of this, it is reasonable to assume that the volume of the cushion chambers are close to the same for the experiment and the simulation under similar cushion pressures. Following the assumptions stated above and the expression formulated in (5.2), we can say that by maintaining the same louver positions, we should achieve the same average cushion pressure, provided that the air-flow out from the cushions are the same for the simulation and the experiment. From equation (2.69) we can see that an increase in pressure will cause an increase in the volume flow out from the cushions, which in turn should cause a reduction in the cushion pressure according to (2.54). Given an equal and constant cushion leakage area and a constant over-pressure in the numerical model, only a difference in the ventilation valve leakage coefficient, c_n^{vv}, can account for the increased air flow out of the cushions in the numerical model. Knowing this, we can tune the leakage coefficient for the ventilation valves, c_n^{vv}, until the average cushion pressure is the same in the simulations and the experiment. Since the value for c_n^{vv} incorporates the loss of the effective valve area as described in the last point in the list above, the absolutely highest c_n^{vv} we can hope for is 0.615. The scale model test presented in 4.12 suggests that a leakage coefficient of $c_n = 0.4543$ provides a steady pressure equal to the pressure found from the scale model experiments. Through comparison with other model tests, a final estimate for cn_{vv} was found as $c_n^{vv} = 0.58$. As mentioned in chapter 4.3, this value has been applied and used for the numerical model through the remaining comparisons with the scale model tests.

Passive leakage

The passive leakage that occurs during the experimental testing is hard to quantify. The plots in Figure 4.13 however provide a good illustration for a case where passive leakage takes place. The orange line, representing the scale model cushion pressure show significant and rapid drop in the cushion pressure. This rapid reduction in pressure is believed to be caused by passive cushion to atmosphere leakage. The plots in Figure 4.13(a) are of the scale model tests and a simulation with the assumption of solid walls for the cushion separators. This means that no air is allowed to penetrate through the inflatable walls separating the cushion chambers. Figure 4.13(b) shows an experiment comparison against a simulation with non-solid walls, meaning that there is air leakage between the cushion chambers as a result of air passing through the non-solid cushion dividers. We can see that both the pitch angle and the cushion pressures, particularly that of cushion 3, becomes a much more close fit for the assumption with non-solid walls. Note that though the roll and heave motions in Figure 4.13 are not accurate, both the heave and roll motions are very small for this simulation, and therefore this error is not very significant. The picture in Figure 5.2 shows how the transverse and center cushion dividers look when the scale model is at full lift capacity. This picture provides a good illustration of why the assumption of solid walls will not be correct for a physical implementation with the inflatable cushion dividers. When comparing Figure 1.10 with 5.2, two effects come into play. Firstly, the increased pressure inside the cushion chambers lifts the model out of the water, causing a visible leakage area under the separation cushions. Secondly, the increased pressure inside the cushion chamber contributes to deflate the separation bag, as the relative pressure inside the separation bag is now lower. Thus, there is a visible leakage area between the fingers of the dividers as well as a leakage area under the dividers. In the series with the solid and the non-solid walls in Figure 4.13, the differences are subtle, but substantial. Though the pressures and motions are interconnected and it is hard to distinguish cause from effect, an implementation of non-solid walls is generally observed to equalize the pressure from chamber to chamber and thus dampen the pressure fluctuations in the cushion chambers. This reduced swing in pressure results in a slightly larger pitching motion, which results in increased passive cushion to atmosphere leakage. The passive cushion to atmosphere leakage can clearly be seen in the pressure for cushion 3 at approximately 7 and 8.5 seconds. The induced passive cushion to atmosphere leakage causes yet larger pitching motions. From the picture in Figure 1.8, we can also see that some leakage will occur under the bag in the aft of the vessel. Some leakage here is intended as a part of the design, in order to flush any water that has entered the bag. However, the amount of leakage observed from the model tests seemed to be in excess of what we should expect. Not accounting for this could affect the accuracy of the numerical model.

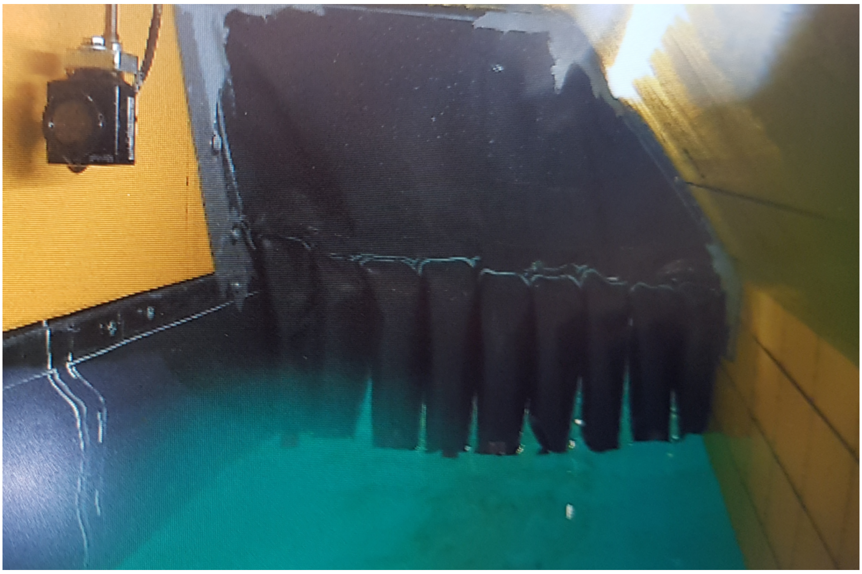

Figure 5.2: Inflated transverse cushion dividers at full cushion lift.

5.1.4 Vessel motion in waves

The response of the numerical model in regular waves is generally very close to the results achieved during the scale model testing. The largest error occurs when the motions of the vessel are very small, such as with roll for head sea and pitch for beam sea. Ignoring these entries, the simulated roll angle is between 27% and 6% smaller than the roll angle generated from the experiments. The largest error occurs for 2.5 meter waves at a wave direction of $\psi = 135°$, while the smallest error is for 2.5 meter waves coming from $\psi = 90°$. The simulated pitch angle varies from 3.8% smaller to 23.3% larger than the equivalent scale model response. As with the roll angle, the largest errors occur when the vessel is subjected to bow sea, while the smallest error occurs when the pitch motion is the dominant motion, such as for head sea. Since the largest error in both roll and pitch occur for bow sea, this could indicate that there are some unmodeled coupling effects between the roll and pitch motions. The heave motions of the vessel generally reflect the same tendencies as the roll and pitch motions. The error in the numerical simulation is large for small motions relative to the experimental results. The plot in Figure 4.15 illustrates this, and shows a large difference in the heave motion when the motions are small. Figure 4.17 and 4.18 illustrate that when the motions are larger, the percentage difference in the heave motion between the numerical model and the scale model diminishes.

5.2 Motion control

The conditions for the simulations in the sub-chapter 4.1 are more ideal with respect to cushion leakage and process noise than what we observed during the scale model experiments. Under these conditions, the numerical model indicates that a roll and pitch damping up towards 80-90% may be possible. These simulations assume that the cushion separation walls are solid and that the ventilation valve leakage coefficient is $c_n^{vv} = 0.8$. The gains for controller 1, discussed in sub-chapter 3.1, which is used in the numerical simulations in sub-chapter 4.1 are also much higher than the gains used in the scale model experiments. These gains have shown to be too high to be applied for the scale model. During the scale model tests, the tuning of the controller gains were limited by the feedback process noise from the sensors. From the experiments we observed that with too high gains the control system simply amplified the noise. From Figures 4.15 and 4.18 we can observe that the control output, which is the louver position, is rarely saturated. Ideally we wish to have a bias of 50%, with controller gains that saturate at 0 and 100 for large excitations. This will result in a maximum response range with respect to increasing and decreasing the cushion pressure. Compared to the louver position shown in Figures 4.15 and 4.18 this means that a smaller bias, and increased controller gains theoretically should produce a better response. The motion damping achieved from the model test experiments is substantial. For regular waves the scale model experiments show that we can achieve a roll damping of the peak to peak roll angle which ranges between 76.7% and 62.1% reduction. The roll damping is most effective for the smaller, 1 meter waves with a period of $T_p = 5s$. For irregular sea, we achieve a reduction in the significant height of the roll angle which is between 41.5% to 54.2%. For regular waves the peak to peak pitch angle is reduced by more than 66.8% for head sea, and more than 55% for bow sea. Also for irregular sea, we can observe that when both the heave, roll and pitch is controlled at $\psi = 45°$, the damping in pitch is smaller than when only two states are controlled. Excluding this test, the significant pitch angle for irregular sea is reduced by approximately 48-50% when pitch control is active. From the power spectral density plots in figure 4.22, we can also observe that around the excitation frequencies of 0.125-0.27 Hz for roll and 0.125-0.2 Hz for pitch, the power is significantly reduced when cushion control is active.

Chapter 6

Conclusion

The results from the scale model tests confirm that the mathematical model serves as a good approximation of the physical system. Accurate modeling of the air flow in the cushions, specifically air leakage, is crucial in order to generate an accurate response. With respect to this, there are some known sources for error, such as leakage through the cushion dividers, which is as of yet only modelled empirically from the results obtained in the wave basin tests. The scale model tests confirm that the four cushion solution can be utilized to obtain a significant roll and pitch damping. For the basin tests in regular sea, the peak to peak roll angles are reduced by as much as 76.7%. For irregular sea, the significant roll angle is reduced by up to 54.2%. For pitch damping, the equivalent tests show a 66.8% and 49.8% damping, respectively. The best results generated by the numerical model indicate that under more ideal conditions with respect to air leakage and noise, as much as 80-90% damping for both roll and pitch may be obtainable.

The scale model tests were carried out quite close to the thesis deadline and thus further work should include further analysis of this data. Through further analysis more definite conclusions may be drawn and additional and improved design criteria may be discovered. With respect to the mathematical model, the initial results from the scale model tests indicate that further work to improve the model may include additional modelling of the cushion air flow, specifically the cushion air leakage. Controlling the airflow within the cushion chambers is key to maintain a high degree of motion control. For a full scale implementation, the cushion separation walls need to be retractable during transit. In addition, the separation walls must be designed in a way that minimizes the air leakage from chamber to chamber during pitch and roll control. The current solution provides very promising results, but further work and improvement on of the design of the separation walls is believed to produce even better results. In addition to this, a new design of the ventilation valves should be considered. By increasing the effective leakage area, the response of the control system will increase. In addition, this increase will mean a reduction in the bias. The vessel can then operate at a louver opening closer to a 50%. This is ideal because saturation of the louver response is then less likely to occur.

Bibliography

Ø. F. Auestad. *The Boarding Control System: Modelling and Control of a Surface Effect Ship for improved accessibility to Offshore Wind Turbines.* PhD thesis, Department of Engineering Cybernetics, Norwegian University of Science and Technology, 2015.

Ø. F. Auestad, J. T. Gravdahl, A. Sørensen, and T. H. Espeland. Motion compensation system for a free floating surface effect ship. In *The 19th World Congress of the International Federation of Automatic Control, IFAC24, Cape Town, South Africa*, 2014.

Ø. F. Auestad, J. T. Gravdahl, T. Perez, and A. J. Sørensen. Boarding control system for improved accessibility to offshore wind turbines: Full-scale testing. *Control Engineering Practice, vol 45, pp. 199-214*, 2015.

J. G. Balchen, T. Andresen, and B. A. Foss. *Reguleringsteknikk.* Institutt for Teknisk Kybernetikk, NTNU, Trondheim, 2003.

O. M. Faltinsen. *Hydrodynamics of high-speed marine vehicles*. Camebridge University Press, 40 West 20th Street, New York, 2005.

T. I. Fossen and T. Perez. Marine systems simulator (mss), 2004. URL `https://github.com/cybergalactic/MSS`.

O. M. Haukeland, V. Hassani, and Ø. F. Auestad. Dynamic modeling and simulation of a surface effect ship with four air cushions. *Submitted to the 12th IFAC Conference on Control Applications in Marine Systems, Robotics, and Vehicles (CAMS 2019)*, 2019a.

O. M. Haukeland, V. Hassani, and Ø. F. Auestad. Roll and pitch damping of a surface effect ship utilizing a four cushion solution. *Submitted to the 12th IFAC Conference on Control Applications in Marine Systems, Robotics, and Vehicles (CAMS 2019)*, 2019b.

P. Kaplan and S. Davis. System analysis techniques for designing ride control system for ses craft in waves. In *The 5th Ship Contr. Syst. Symp. Annapolis, Maryland, USA*, 1978.

H. K. Khalil. *Nonlinear Systems, Third Edition*. Pearson Education Limited, Edinburgh Gate, Harlow, Essex CM20 2JE, 2014.

Umoe Mandal. Umoe voyager, 2018. URL `https://www.wavecraft.no/model/voyager-38x/`.

MATLAB®. Power spectral density estimates using fft, 2019a. URL `https://se.mathworks.com/help/matlab/ref/fft.html`.

MATLAB®. Periodogram power spectral density estimate, 2019b. URL `https://se.mathworks.com/help/signal/ref/periodogram.html`.

MRPC. Marine roll & pitch control, 2019. URL `http://www.mrpc.no/?page_id=44`.

D. Myrhaug and W. Lian. *Marine Dynamics Irregular Waves*. Institute for marine technology, NTNU, Kompendieforlaget, Nardoveien 12, 7005 Trondheim, 2009.

T. Perez. *Ship Motion Control: Course Keeping and Roll Reduction using Roll and Fins. Advances in Industrial Control Series*. Springer-Verlag, London, UK, 2005.

B. Pettersen. *Marin Teknikk 3, Hydrodynamikk*. Marine Technology Centre, Department of Marine Technology, Trondheim, Norway, 2007.

K. J. Rawson and E. C. Tupper. *Basic Ship Theory, Fifth Edition, Volume 2*. Butterworth-Heinemann Linieare House, Jordan Hill, Oxford, 2001.

B. R. Reguram, S. Suredran, and S. K. Lee. Application of fin system to reduce pitch motion. *International Journal of Naval Architecture and Ocean Engineering 8*, 2016.

T. C. Smith and W. L. Thomas. *A Survey of Ship Motion Reduction Devices*. David Taylor Research Center, Ship Hydromechanics Department, Bethesda, Maryland 20084-5000, 1990.

A. J. Sørensen. *Modelling and control of SES dynamics in the vertical plane*. PhD thesis, Department of Engineering Cybernetics, Norwegian University of Science and Technology, 1993.

A. J. Sørensen. *Marine Control Systems Propulsion and Motion Control of Ships and Ocean Structures, Lecture notes*. Department of Marine Technology, NTNU, 2012.

A. J. Sørensen and O. Egeland. Design of ride control system for surface effect ships using dissipative control. *Automatica*, 31(2):183–199, 1995.

J. Tønnessen, H. E. Bryn, Ø. Auestad, J. T. Gravdahl, and V. Hassani. Roll damping of a surface effect ship with split air cushion. In *The 11th IFAC Conference on Control Applications in Marine Systems (CAMS)*, 2018.

V. Vamråk, N. H. Bua, V. Hassani, and Ø. Auestad. Robust lateral control of a surface effect ship using h-inf mixed sensitivity synthesis. In *The 10th IFAC Conference on Control Applications in Marine Systems (CAMS)*, 2016.

F. M. White. *Fluid Mechanics 8th Edition*. McGraw-Hill Education, 2015.

Appendix A

State space matrices

$$B = \begin{bmatrix} 0 & 0 & 0 & 0 \\ 0 & 0 & 0 & 0 \\ 0 & 0 & 0 & 0 \\ 0 & 0 & 0 & 0 \\ 0 & 0 & 0 & 0 \\ 0 & 0 & 0 & 0 \\ \frac{K_{21}}{K_{11}} & 0 & 0 & 0 \\ 0 & \frac{K_{22}}{K_{12}} & 0 & 0 \\ 0 & 0 & \frac{K_{23}}{K_{13}} & 0 \\ 0 & 0 & 0 & \frac{K_{24}}{K_{14}} \end{bmatrix} \tag{A.1}$$

$$E = \begin{bmatrix} 0 & 0 & 0 & 0 & 0 & 0 & 0 \\ 0 & 0 & 0 & 0 & 0 & 0 & 0 \\ 0 & 0 & 0 & 0 & 0 & 0 & 0 \\ 1 & 0 & 0 & 0 & 0 & 0 & 0 \\ 0 & 1 & 0 & 0 & 0 & 0 & 0 \\ 0 & 0 & 1 & 0 & 0 & 0 & 0 \\ 0 & 0 & 0 & \frac{\rho_{c0}}{K_{11}} & 0 & 0 & 0 \\ 0 & 0 & 0 & 0 & \frac{\rho_{c0}}{K_{12}} & 0 & 0 \\ 0 & 0 & 0 & 0 & 0 & \frac{\rho_{c0}}{K_{13}} & 0 \\ 0 & 0 & 0 & 0 & 0 & 0 & \frac{\rho_{c0}}{K_{14}} \end{bmatrix} \tag{A.2}$$

$$C = \begin{bmatrix} 0 & 1 & 0 & 0 & 0 & 0 & 0 & 0 & 0 & 0 \\ 0 & 0 & 1 & 0 & 0 & 0 & 0 & 0 & 0 & 0 \\ 0 & 0 & 0 & 1 & 0 & 0 & 0 & 0 & 0 & 0 \\ 0 & 0 & 0 & 0 & 1 & 0 & 0 & 0 & 0 & 0 \\ 0 & 0 & 0 & 0 & 0 & 1 & 0 & 0 & 0 & 0 \\ 0 & 0 & 0 & 0 & 0 & 0 & 1 & 0 & 0 & 0 \\ 0 & 0 & 0 & 0 & 0 & 0 & 0 & 1 & 0 & 0 \\ 0 & 0 & 0 & 0 & 0 & 0 & 0 & 0 & 1 & 0 \\ 0 & 0 & 0 & 0 & 0 & 0 & 0 & 0 & 0 & 1 \end{bmatrix} \tag{A.3}$$

$$\mathrm{A} = \begin{matrix} 0 & 0 & 0 & 1 & 0 & 0 & 0 & 0 & 0 & 0 \\ 0 & 0 & 0 & 0 & 1 & 0 & 0 & 0 & 0 & 0 \\ 0 & 0 & 0 & 0 & 0 & 1 & 0 & 0 & 0 & 0 \\ -\frac{C_{33}}{m+A_{33}} & 0 & 0 & -\frac{B_{33}}{m+A_{33}} & 0 & 0 & \frac{p_0 A_{c_1}}{m+A_{33}} & \frac{p_0 A_{c_2}}{m+A_{33}} & \frac{p_0 A_{c_3}}{m+A_{33}} & \frac{p_0 A_{c_4}}{m+A_{33}} \\ 0 & -\frac{C_{44}}{I_{44}+A_{44}} & 0 & 0 & -\frac{B_{44}}{I_{44}+A_{44}} & 0 & \frac{y_{cp_1} p_0 A_{c_1}}{I_{44}+A_{44}} & \frac{y_{cp_2} p_0 A_{c_2}}{I_{44}+A_{44}} & \frac{y_{cp_3} p_0 A_{c_3}}{I_{44}+A_{44}} & \frac{y_{cp_4} p_0 A_{c_4}}{I_{44}+A_{44}} \\ 0 & 0 & -\frac{C_{55}}{I_{55}+A_{55}} & 0 & 0 & -\frac{B_{55}}{I_{55}+A_{55}} & -\frac{x_{cp_1} p_0 A_{c_1}}{I_{55}+A_{55}} & -\frac{x_{cp_2} p_0 A_{c_2}}{I_{55}+A_{55}} & -\frac{x_{cp_3} p_0 A_{c_3}}{I_{55}+A_{55}} & -\frac{x_{cp_4} p_0 A_{c_4}}{I_{55}+A_{55}} \\ 0 & 0 & 0 & -\frac{\rho_{c0} A_{c_1}}{K_{11}} & -\frac{\rho_{c0} A_{c_1} y_{cp_1}}{K_{11}} & \frac{\rho_{c0} A_{c_1} x_{cp_1}}{K_{11}} & -\frac{K_3}{K_{11}} & 0 & 0 & 0 \\ 0 & 0 & 0 & -\frac{\rho_{c0} A_{c_2}}{K_{12}} & -\frac{\rho_{c0} A_{c_2} y_{cp_2}}{K_{12}} & \frac{\rho_{c0} A_{c_2} x_{cp_2}}{K_{12}} & 0 & -\frac{K_3}{K_{12}} & 0 & 0 \\ 0 & 0 & 0 & -\frac{\rho_{c0} A_{c_3}}{K_{13}} & -\frac{\rho_{c0} A_{c_3} y_{cp_3}}{K_{13}} & \frac{\rho_{c0} A_{c_3} x_{cp_3}}{K_{13}} & 0 & 0 & -\frac{K_3}{K_{13}} & 0 \\ 0 & 0 & 0 & -\frac{\rho_{c0} A_{c_4}}{K_{14}} & -\frac{\rho_{c0} A_{c_4} y_{cp_4}}{K_{14}} & \frac{\rho_{c0} A_{c_4} x_{cp_4}}{K_{14}} & 0 & 0 & 0 & -\frac{K_3}{K_{14}} \end{matrix} \tag{A.4}$$

Appendix B

Equations for water volume calculations

$$\begin{aligned}A_{x_i}^{Tra} &= \frac{1}{2}(-P_{3_y}\frac{P_{4_x}-P_{3_x}}{P_{4_y}-P_{3_y}}+P_{3_x}+x_4)\\ &\quad -\frac{1}{2}(\frac{x_1-x_2}{z_1-z_2}(-P_{1_z}-P_{3_y}\frac{P_{4_z}-P_{3_z}}{P_{4_y}-P_{3_y}}+P_{3_z})+P_{1_x}+x_1)\end{aligned} \tag{A.1}$$

$$B_{x_i}^{Tra} = \frac{1}{2}\frac{P_{4_x}-P_{3_x}}{P_{4_y}-P_{3_y}}-\frac{1}{2}\frac{x_1-x_2}{z_1-z_2}\frac{P_{4_z}-P_{3_z}}{P_{4_y}-P_{3_y}} \tag{A.2}$$

$$A_{z_i}^{Tra} = z_1+P_{3_y}\frac{P_{4_z}-P_{3_z}}{P_{4_y}-P_{3_y}}-P_{3_z} \tag{A.3}$$

$$B_{z_i}^{Tra} = \frac{P_{4_z}-P_{3_z}}{P_{4_y}-P_{3_y}} \tag{A.4}$$

$$A_{x_i}^{Tri} = P_{3_x}-P_{3_y}\frac{P_{4_x}-P_{3_x}}{P_{4_y}-P_{3_y}}-(\frac{x_1-x_2}{z_1-z_2}(\frac{P_{4_z}-P_{3_z}}{P_{4_y}-P_{3_y}}(-P_{3_y})+P_{3_z}-P_{1_z})+P_{4_x}) \tag{A.5}$$

$$B_{x_i}^{Tri} = \frac{P_{4_x}-P_{3_x}}{P_{4_y}-P_{3_y}}-\frac{x_1-x_2}{z_1-z_2}(\frac{P_{4_z}-P_{3_z}}{P_{4_y}-P_{3_y}}) \tag{A.6}$$

$$A_{z_i}^{Tri} = -P_{2_y}\frac{-P_{1_z}+P_{2_z}+P_{4_z}-P_{3_z}}{P_{1_y}-P_{2_y}}-P_{2_z}+P_{3_z} \tag{A.7}$$

$$B_{z_i}^{Tri} = \frac{-P_{1_z}+P_{2_z}+P_{4_z}-P_{3_z}}{P_{1_y}-P_{2_y}} \tag{A.8}$$

Appendix C

Simulink block-diagram of the SES-dynamics

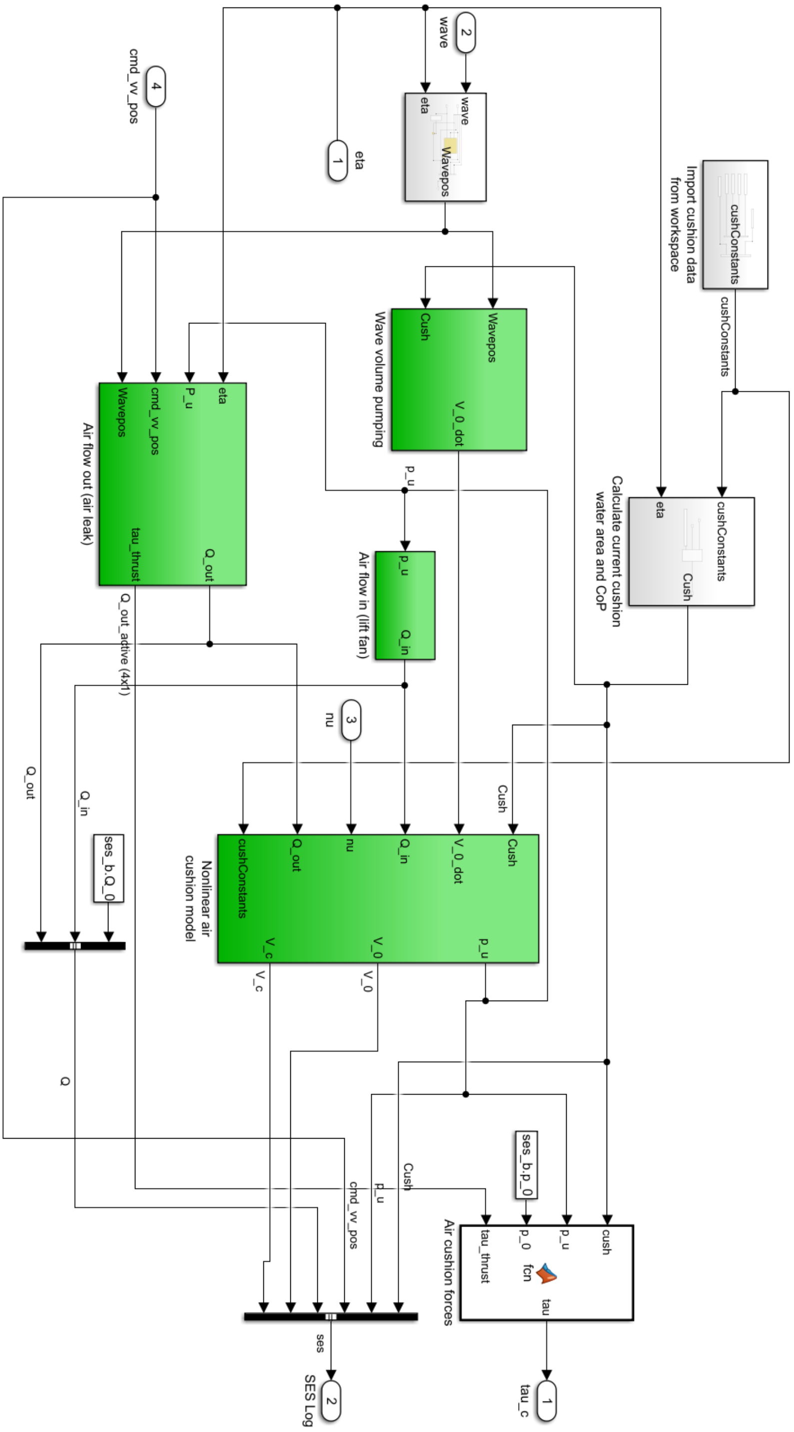

2
wave
eta
Wavepos
1
eta
4
cmd_vv_pos
cushConstants
Import cushion data from workspace
cushConstants
Wavepos
Cush
V_0_dot
Wave volume pumping
eta
P_u
cmd_vv_pos
Wavepos
Q_out
tau_thrust
Air flow out (air leak)
Q_out_active (4x1)
p_u
p_u
Q_in
Air flow in (lift fan)
cushConstants
eta
Cush
Calculate current cushion water area and CoP
3
nu
Cush
Cush
V_0_dot
Q_in
nu
Q_out
cushConstants
p_u
V_0
V_c
Nonlinear air cushion model
V_0
V_c
Q_in
Q_out
ses_b.Q_0
Q
ses_b.p_0
cush
p_u
p_0
tau_thrust
fcn
tau
Air cushion forces
Cush
p_u
cmd_vv_pos
1
tau_c
ses
2
SES Log

Appendix D

Calculation of significant heave, roll and pitch motions

Through the use of the Fast Fourier Transform (FFT) function in MATLAB® *fft*, MATLAB® [2019a], the time-series for the heave/roll/pitch motion of the vessel can be converted to the a discrete Fourier transform,

$$Y(k) = \sum_{j=1}^{n} X(j) e^{(-2\pi i/n)(j-1)(k-1)} \tag{A.1}$$

As we are only interested in the motions of the heave, roll and pitch movement we subtract the average, such that the MATLAB® *fft* implementation for in example heave, becomes; *ifft*$(\eta_3 - \bar{\eta}_3)$. According to MATLAB® [2019b], an estimation of the spectral density for the heave/roll/pitch motions, also known as a periodogram, can then be calculated as

$$P(f) = \Delta t |Y(k)|^2 \tag{A.2}$$

According to Myrhaug and Lian [2009], the moment of the spectrum can be calculated as

$$m_n^f = \int_0^\infty f^n S(f) df, \qquad S(f) \approx P(f). \tag{A.3}$$

Also according to Myrhaug and Lian [2009], the significant height of waves in a JONSWAP spectrum can be calculated as shown in (A.4). Because the significant angles and the significant heave response will be directly related to the wave height inducing the motion, we assume the distribution of these motions and the corresponding wave height to be the same.

$$H_s = 4\sqrt{m_0} = \int_0^\infty P(f) df. \tag{A.4}$$

Here, the significant height, H_s, signifies the significant heave position, or the significant roll or pitch angle depending on which degree of freedom is input as the initial time-series, represented by $X(j)$.

Appendix E

IFAC CAMS 2019 submissions

E.1 Dynamic Modeling and Simulation of aSurface Effect Ship with Four Air Cushions

Dynamic Modeling and Simulation of a Surface Effect Ship with Four Air Cushions

Ola M. Haukeland [*] **Vahid Hassani** [*,**] **Øyvind Auestad** [***]

[*] *Centre for autonomous marine operations and systems (AMOS), Dept. of Marine Technology, Norwegian Univ. of Science and Technology, Trondheim, Norway.*
[**] *Department of Ships and Ocean Structures, SINTEF Ocean, Trondheim, Norway.*
[***] *Umoe Mandal AS, Mandal, Vest-Agder, Norway.*

Abstract: This paper deals with dynamic modelling and numerical simulations of a Surface Effect Ship (SES) with split cushion. Traditionally, a SES is a catamaran with front and aft seals equipped with lift fans that could fill an air cushion with pressurized air to lift up to 90 % weight of the vehicle. A new SES concept is designed by UMOE Mandal AS that consists of four air chambers, each one equipped with variable vent valves, through which cushion pressures can be controlled by adjusting the air out-flow from the cushion. The new designs makes it possible to actively regulate the motion of the SES in all decrees of freedom but surge. Basic model scale tests have shown effectiveness of such design in for active motion damping. In this paper, we develop a dynamic model of the four cushion SES. Furthermore, we present a high fidelity numerical simulator that can effectively simulates the dynamics of the vessel. Results from early model test experiments are used to validate the developed simulation model. A companion paper studies the performance of the control system through numerical simulation using the presented high fidelity model of SES subject to waves.

Keywords: Surface Effect Ship, Split Cushion, Motion control, Process Plant Model

---

1. INTRODUCTION

1.1 Motivation

The rough seas surrounding offshore structures such as oil platforms, oil-rigs and wind turbines provide a challenge for both crew transport and offshore structure inspections. The use of surface effect ships has emerged as a competitive alternative to helicopter transport, proving high levels of safety, comfort, fuel efficiency and overall reduced cost of offshore logistics, Mandal 2018. The main challenge for sea transport is safety at crew transfer and ride comfort at high transit speeds. Increased motion control and motion damping provides the solution to these challenges, and contributes to further expand the window of operations for the surface effect vessels at harsh weather conditions.

1.2 Surface effect ship

The surface effect ship can be described as a hybrid between a catamaran and hovercraft. The hull of a SES is formed like the hull of a catamaran except the bow and stern is sealed off. Figure 1 gives an illustration of a SES cross-section as seen from the side. The purpose of this special shape, is to create a volume in which the air will be trapped and the flow of air can be controlled. This volume is referred to as the cushion chamber, where as the air inside the volume is referred to as the air cushion. This cushion allows the vessel to glide on the layer of air, rather than floating due to the displacement of the hull like conventional vessels. The design brings a few benefits such as reduction in drag, improved ride comfort and added flexibility with respect to heave. The new SES design proposed in this paper is to further divide the cushion into four air chambers. Doing so, one can add the pitch and roll control to the list of benefits. Due to the low drag and improved ride comfort of the SES, most SES-vessels are high-speed vessels. The drawback with the cushion solution is that the seals in the front and aft of the vessel suffer a lot of wear and tear. Depending on use and the transit velocities of the vessel, these seals might need replacement more than once per year. This project is done in collaboration with Umoe Mandal. At their request, and to avoid the publication of sensitive data, the results for the simulations and experiments will be normalized with respect to angles, pressure or volume flow.

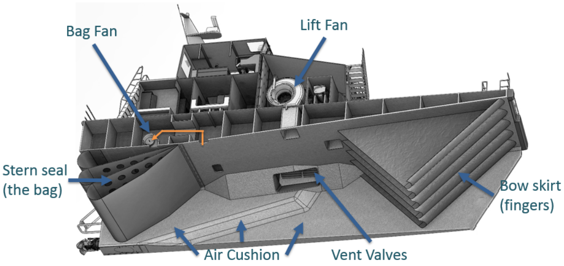

Fig. 1. Cross section of a SES. Illustration by Umoe Mandal.

1.3 *Ses cushion-control*

Other systems for controlling a SES-vessel by manipulating the cushion pressure are already developed and in use, among them is the ride control system and the boarding control system. The ride control system was first featured in Kaplan and Davis 1978, and has since been further developed by Sørensen and Egeland 1995. The purpose of the system is to create a more smooth ride at high transit velocities. The system provides active damping of vertical motions by manipulating and reducing the cushion pressure fluctuations caused by rough sea. The boarding control system has been developed by Ø. F. Auestad 2015. The main use of the boarding control system is to reduce the movements of the vessel's bow, so that it is possible to secure safer transfer from the ship to offshore structures, specifically, offshore wind-turbines. The boarding control system relies on manipulating the pressure of the single cushions to induce heave motions, counteracting the wave-induced motions. These are examples of manipulating the cushion pressure as a way of controlling the vessel motions, that have been of great practical importance, and that provide a good basis and motivation for further development within the field.

1.4 *Cushion division*

In this paper, we consider a SES design in which the single cushion is divided into four sections by the use of solid walls or inflatable separators. The division and subsequent cushion numbering can be seen in figure 2. The implementation of the four chambers solution using inflatable bags allows for usage of a the traditional one-cushion solution when the four cushion division is not needed.

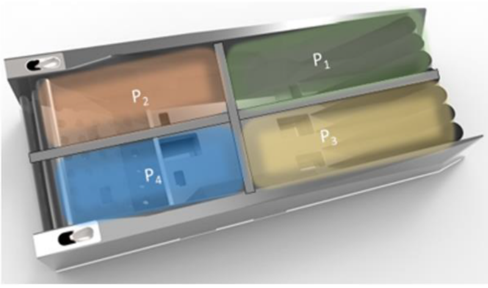

Fig. 2. The cushion separation and numbering as seen from below.

2. MATHEMATICAL MODELING

The system is modeled around a body-fixed coordinate system, centered at the center of gravity in the x and y-direction, and at the center of buoyancy in the z-direction. The heave center of buoyancy will vary for a SES, depending on the current cushion pressure. With respect to the coordinate system, it is defined at the initial cushion pressure p_0, also known as the equilibrium pressure. The coordinate system is illustrated in figure 3.

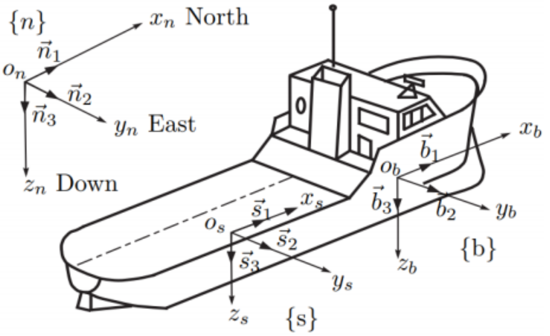

Fig. 3. Coordinate system used for the mathematical model, {b}.

2.1 *Air-cushion volume and wave volume pumping*

The volume of air inside each of the cushions can be described as

$$V_i = -V_{0_i} + A_{c_i}(-\eta_3 - y_{cp_i}\eta_4 + x_{cp_i}\eta_5) \tag{1}$$

Here V_{0_i} is the volume occupied by waves entering or exiting each of the cushion chambers. A_{c_i} is the area of the water surface inside each cushion, while y_{cp_i} and x_{cp_i} describe the cushion center point, which is also referred to as the center of pressure. Lastly, η_3, η_4 and η_5 represent the heave, roll and pitch of the vessel, respectively. The cushion volume rate of change, $\dot{V}_{c_i}$, can be calculated by differentiating the formula for the cushion volume given in equation (1) with respect to time. The equation then becomes

$$\dot{V}_{c_i} = A_{c_i}(-\nu_3 - y_{cp_i}\nu_4 + x_{cp_i}\nu_5) - \dot{V}_{0_i} \tag{2}$$

where $\dot{V}_{0_i}$ is called the wave volume pumping and ν_3, ν_4 and ν_5 represent the heave speed, roll rate and pitch rate of the vessel, respectively. Wave volume pumping is the rate of volume change due to waves passing through the cushion chambers. The wave volume pumping is calculated according to equation (3). The volume that the wave occupies inside the cushion can be described as in equation (4). These equations are inspired by Auestad 2015, as well as Sørensen and Egeland 1995.

$$\dot{V}_{0_i}(t) = \int_{y_{1_i}}^{y_{2_i}} \int_{L_{1_i}}^{L_{2_i}} \dot{\zeta}(x,y,t)dA \tag{3}$$

$$V_{0_i}(t) = \int_{y_{1_i}}^{y_{2_i}} \int_{L_{1_i}}^{L_{2_i}} \zeta(x,y,t)dA \tag{4}$$

In these equations y_{1_i} and y_{2_i} constitute the width of cushion i, while L_{1_i} to L_{2_i} constitutes the length of cushion i measured at the current water-level. In equation (3), the term $\zeta(x,y,t)$ is the wave elevation function expressing the wave elevation at position x and y, at time t. According to Perez 2005, this wave elevation can be described as

$$\zeta(x,y,t) = \bar{\zeta}\sin\left(\omega t + \epsilon - k(x\cos(\chi) + y\sin(\chi)\right) \tag{5}$$

$$\dot{\zeta}(x,y,t) = \bar{\zeta}\omega\cos\left(\omega t + \epsilon - k(x\cos(\chi) + y\sin(\chi)\right) \tag{6}$$

In the equations above, $\bar{\zeta}$ is the wave amplitude, ω is the circular wave frequency, and k is the wave number. The wave number can be expressed as $k = \frac{2\pi}{\lambda}$, where λ is the wave length. Furthermore, ϵ is the phase of the wave, and the term $x\cos(\chi) + y\sin(\chi)$ expresses the direction of the wave propagation relative to the vessel body-frame.

Differentiating equation (5), provides equation (6), which is used to calculate the wave volume pumping in equation (3). The wave elevation and corresponding wave-forces acting on the vessel, outside of the cushion pressure, will be modeled using the *Marine Systems Simulator* created by Fossen and Perez 2004, and will not be further elaborated on in this section.

2.2 Non-linear cushion pressure dynamics

The non-linear pressure dynamics equations are in inspired by Sørensen and Egeland 1995. Some assumptions regarding linearization of the air flow, and spatial variations in pressure vary from Sørensen and Egeland 1995, leading to a few changes to these equations. Further, the equations are adapted to the current model, such that it includes the four cushion solution. The basis for the non-linear pressure dynamics is the equation for continuity of mass flow and the relation between pressure and density, shown in equations (7) and (13), respectively. The cushion pressure is considered to be uniform within each of the cushion chambers.

$$\dot{m}_{in_i} - \dot{m}_{out_i} = \frac{d}{dt}(\rho_{c_i}(t)V_{c_i}(t)) \tag{7}$$

In equation (7), the left part of the equation can also be stated as

$$\dot{m}_{in_i} - \dot{m}_{out_i} = \rho_a(Q_{in_j}(t) - Q_{out_j}(t)). \tag{8}$$

By performing the differentiation of the right side expression in equation (7), and substituting the left side with (8), we get equation (9).

$$\rho_a(Q_{in_j}(t) - Q_{out_j}(t)) = \dot{\rho}_{c_i}(t)V_{c_i}(t) + \rho_{c_i}(t)\dot{V}_{c_i}(t) \tag{9}$$

Here $V_{c_i}(t)$ and $\dot{V}_{c_i}(t)$ is the chamber air volume and its rate of change, which can be expressed as derived in section 2.1. Q_j is the air flow caused by fan j, while ρ_a and ρ_{c_i} are the respective air-densities of the atmosphere and the cushion. Assuming an adiabatic process, the first law of thermodynamics, $\delta U + \delta W = \delta Q^{heat} = 0$, can be used to derive the adiabatic pressure-volume relationship

$$\frac{p}{p_0} = \left(\frac{V_0}{V}\right)^{\gamma}. \tag{10}$$

where γ is the ratio of specific heat for air. Since there is no loss of mass in the air flow traveling from the volumes V_0 to V, the volume-density relationship between the two spaces can be written as

$$\frac{V_0}{V} = \frac{\rho}{\rho_0}. \tag{11}$$

The pressure-density relationship then becomes

$$\rho = \rho_0\left(\frac{p}{p_0}\right)^{\frac{1}{\gamma}}. \tag{12}$$

As we are interested in the pressure differential from the atmosphere to the cushion, the values for the cushion and atmospheric pressure and density are substituted into equation (12).

$$\rho_{c_i}(t) = \rho_a\left(\frac{p_a + p_{u_i}(t)}{p_a}\right)^{\frac{1}{\gamma}} \tag{13}$$

Differentiating equation (13) with respect to time leads to

$$\dot{\rho}_{c_i}(t) = \frac{\rho_a}{p_a^{\frac{1}{\gamma}}\gamma}(p_a + p_{u_i}(t))^{\frac{1-\gamma}{\gamma}}\dot{p}_{u_i}(t). \tag{14}$$

By combining equations (9), (13) and (14), the final equation representing the non-linear cushion pressure can be expressed as shown in equation (15).

$$\begin{aligned}\dot{p}_{u_i}(t) =& \frac{\gamma(p_a + p_{u_i}(t))}{V_{c_i}(t)}\times \\ & \left(\left(\frac{p_a}{p_a + p_{u_i}(t)}\right)^{\frac{1}{\gamma}}(Q_{in_j}(t) - Q_{out_j}(t)) - \dot{V}_{c_i}(t)\right)\end{aligned} \tag{15}$$

2.3 Cushion air flow

The flow of air into the cushions are caused by fans. The volumetric flow rate produced by each of these fans, can be described as

$$Q_{in_i} = \frac{s_i}{s_{max}}Q_i^*. \tag{16}$$

Here Q_i^* is the flow of the fan for cushion i which is set by the fan characteristics. s_i and s_{max} is the current and maximum fan rotation speed. The pressure generated by the lift fan is given as $p = (\frac{s_i}{s_{max}})^2 p_i^*$, where the specific fan pressure p_i^* can be substituted with p_{u_i}.

Airflow out of a cushion is called air leakage. There are two types of leakages to consider, passive leakage and controlled leakage. Controlled air leakage is the airflow that exits out of the controlled ventilation valves at the sides of the cushion chambers. The passive leakage is the uncontrolled leakage that occurs when air is forced out from under the sides of the cushion chambers, or leaves the chamber in any way that is not controlled or intentional. The amount of air leakage is dependent on the leakage area and the cushion pressure. The total air leakage of a chamber can be described as:

$$A_{L_i}(t) = A_{p_i}(t) + A_i^{ctrl}(t). \tag{17}$$

$A_{L_i}(t)$ represents the total leakage area, A_{p_i} is the passive leakage area, and A_i^{ctrl} is the controlled leakage area.

Controlled leakage The controlled leakage area can be described as

$$A_i^{ctrl}(t) = A_{i_{max}}^{ctrl}\frac{A_{i_{min\%}}^{ctrl} + (1 - A_{i_{min\%}}^{ctrl})u_i(t)}{100} \tag{18}$$

Here $A_{i_{max}}^{ctrl}$ is the leakage area at maximum vent valve opening. $A_{i_{min\%}}^{ctrl}$ is the lowest possible area of the vent valve opening, given as a percentage of the maximum vent valve opening. Lastly $u(t)_i$ is the control input signal, for the opening of the vent valves.

We wish to express the flow out of the cushion. The volumetric flow rate is defined as

$$Q = vA \tag{19}$$

where v is the velocity of the fluid, while A is the cross-sectional area. Due to the geometry of the leakage area some flow reduction will occur, such that $A = A_L c_n$, where A_L is the leakage area, and c_n is a orifice coefficient for the leakage area. Starting with the Euler equation,

$$\frac{dp}{\rho} + vdv + gdz = 0, \tag{20}$$

and assuming an adiabatic pressure-density relationship, such that

$$\frac{p}{\rho^{\gamma}} = C, \tag{21}$$

the Bernoulli equation for an adiabatic, compressible flow can be derived. Assuming none, or negligible elevation change, the simplified Bernoulli equation for adiabatic compressible flow can be written as

$$\left(\frac{\gamma}{\gamma-1}\right)\frac{p_{c_i}(t)}{\rho_{c_i}(t)} + \frac{1}{2}v_{c_i}^2 = \left(\frac{\gamma}{\gamma-1}\right)\frac{p_a}{\rho_a} + \frac{1}{2}v_a^2. \tag{22}$$

From this, an expression for the air velocity can be derived. We assume no initial air-velocity in the chambers, such that $v_{c_i} = 0$. Further, we assume that all excess pressure in the ventilated air from a cushion is converted to air-velocity upon release. Thus equation (22) can be rearranged to express the velocity, as shown in equation (23).

$$v_a(t) = \sqrt{2\left(\frac{\gamma}{\gamma-1}\right)\left(\frac{p_{c_i}(t)}{\rho_{c_i}(t)} - \frac{p_a}{\rho_a}\right)} \tag{23}$$

The pressure inside the cushion is described as;

$$p_{c_i}(t) = p_a + p_{u_i}(t) \tag{24}$$

where p_{c_i} is the total cushion pressure, which can be split into the atmospheric pressure p_a and the uniform cushion pressure p_{u_i}. By inserting this expression for $p_{c_i}(t)$ into (23) and combining with equation (19), we get a final expression describing the volumetric flow of the controlled leakage as shown in (25).

$$Q_i(t) = A_i^{ctrl}(t)c_n(i)\sqrt{\frac{2\gamma}{\gamma-1}\left(\frac{p_{u_i}(t)+p_a}{\rho_{c_i}(t)} - \frac{p_a}{\rho_a}\right)} \tag{25}$$

Here $\rho_c(t)$ is found from the expression derived in (13).

Passive leakage The passive leakage area is calculated as the sum of any area that occurs under the hull, fingers or bag of the vessel that is no longer below water-level, as seen from inside the cushion. The passive leakage area can be further divided into inter-cushion leakage, and atmospheric leakage. To calculate the passive atmospheric leakage area for a chamber, the bottom edge of every wall surrounding a chamber is represented as a line. Each of these four lines enclosing a chamber are divided into ten points from the start of the wall to the the end of the wall. At each of these points, the height from the water-surface to the draft of the given point is calculated. This height is calculated following equation (26). If the height is negative, leakage occurs.

$$\begin{aligned} H_{L_{ijk}}(t) = & -T - \eta_3(t) - y_{ijk}\eta_4(t) \\ & + x_{ijk}\eta_5(t) + h_{p_i}(t) - \zeta_{ijk}(t) \end{aligned} \tag{26}$$

In the equation above, $H_{L_{ijk}}$ is the height of point k on line j for cushion i, relative to the water plane. T is the draught of the vessel at the initial heave position, $\eta_3 = 0$. Furthermore y_{ijk} and x_{ijk} is the distance from the center of gravity to point ijk. The term h_{p_i} is added to equation (26) as the cushion pressure leakage will be dependent on the height of the water column inside the cushion. The over-pressure inside the cushion will displace water from inside the cushion, such that the water-level inside the cushion will be lower than that on the outside. The term h_{p_i} can be expressed as shown in equation (27), and can simply be explained as a pressure to water-column height conversion.

$$h_{p_i}(t) = \frac{p_{u_i}(t)}{g\rho_w} \tag{27}$$

In equation (26), ζ_{ijk} represents the sea level elevation at the relative position of point ijk. This elevation can be expressed as

$$\begin{aligned} \zeta_{ijk}(t) = \sum_n \Big(& \zeta_{a_n}\sin(\omega_n t - \kappa_n(x_{ijk}\cos(\chi_n) \\ & + y_{ijk}\sin(\chi_n)) + \epsilon_n) \Big) \end{aligned} \tag{28}$$

Most terms in equation (28) are previously addressed and explained in section 2.1. Note that in the equation above, the letter k is used as a subscript, therefore the letter κ is used to denote the wave number. For an irregular seastate, the specific wave elevation at a point will be the sum of many different regular waves. The elevation for each of these regular waves are expressed as previously explained in equation (5). Therefore, the total wave elevation at point ijk, becomes the sum of the elevation from every regular wave at the given time and the given position of the point. The position of point ijk is expressed by x_{ijk} and y_{ijk}. Lastly, ϵ_n represents the phase of regular wave number n. The total passive cushion leakage area can be expressed as

$$A_{p_i}(t) = A_{p_i}^a(t) + A_{p_i}^c(t) \tag{29}$$

where the superscripts a and c denotes the cushion to atmosphere leakage area, and the cushion to cushion leakage area, respectively. The passive leakage area from cushion to atmosphere can be expressed as

$$A_{p_i}^a(t) = \sum_{j_a=1}^{2}\left(H_{L_{ij_a}}(t)\sum_{k=1}^{10}(\Delta x_{ij_ak} + \Delta y_{ij_ak})\right), \tag{30}$$

where subscript j_a signifies the lines j which represent a wall separating the cushions from the atmosphere. Similarly, the passive leakage area from cushion to cushion, can be expressed as

$$A_{p_i}^c(t) = \sum_{j_c=1}^{2}\left(H_{L_{ij_c}}(t)\sum_{k=1}^{10}(\Delta x_{ij_ck} + \Delta y_{ij_ck})\right), \tag{31}$$

where subscript j_c signifies the lines j separating cushions. The volumetric flow for passive cushion to atmosphere leakage can be expressed in the same way as the controlled leakage in equation (25), by simply substituting the leakage area $A_i^{ctrl}(t)c_n(i)$ with $A_{p_i}^a$.

For the volumetric flow for the inter-cushion leakage, we assume that the pressure in cushion i is higher than the pressure in cushion j. Like before, we also assume no initial air-velocity in i, and that all pressure differential between cushions i and j is converted to air-velocity when the air enters cushion chamber j. The expression formed for v_j in (23) can then be applied. The volumetric airflow between cushions can be expressed by substituting the areas, pressures and densities in equation (25) with the relevant values for the two cushions affected by the leak. The cushion air density ρ_{ci} can be calculated from the expression derived in equation (13).

$$Q_i(t) = A_{p_i}^c(t)c_n\sqrt{\frac{2\gamma}{\gamma-1}\left(\frac{p_{c_i}(t)}{\rho_{c_i}(t)} - \frac{p_{c_j}(t)}{\rho_{c_j}(t)}\right)} \tag{32}$$

Equation (32) expresses the air flow out from cushion i, due to leakage into cushion j. There is no loss of mass in the exchange, and so the corresponding air-flow out from cushion j is the same as in (32), with a negative sign. Note that if the cushion pressure is reversed, that is cushion j holds a higher pressure than cushion i, the i and j subscripts in equation (32) are switched. Also note that the cushion separating walls are considered solid, such that no air can pass though them. However in practice, as previously explained, they are inflatable bags, such that some unknown leakage might occur. The sealing properties of these dividers will not be known until a model is created. To account for this, the model includes the option of adding a percentage, fixed or varying leakage area for each of the cushion dividers.

2.4 *Cushion forces*

The model is created for stationary or very low vessel speeds. Therefore only the forces in heave, roll and pitch are considered. The forces generated by the pressure in the cushions is calculated following the pressure force relation, $F = pA$. In similar fashion, the moments generated by the cushion pressures is calculated as $M = d_{cp_i} pA$, where d_{cp_i} represents the distance from the vessel center of gravity to the center of pressure in cushion i. Adding the forces and moments induced by each of the cushions, provides the total forces and moments acting on the vessel caused by the cushion pressures. The resulting expression for these forces and moments are given below in equations (33) to (35).

$$F_{3_c}(t) = \sum_{i=1}^{4} -p_0 \mu_{u_i}(t) A_{xy_i} \tag{33}$$

$$M_{4_c}(t) = \sum_{i=1}^{4} -y_{cp_i} p_0 \mu_{u_i}(t) A_{xy_i} \tag{34}$$

$$M_{5_c}(t) = \sum_{i=1}^{4} x_{cp_i} p_0 \mu_{u_i}(t) A_{xy_i} \tag{35}$$

In the equations above, A_{xy_i} is the area of the water surface, mapped onto the x-y-plane. Note that because the positive z-direction is defined as down, and a positive pressure will cause a force working upwards, the heave force, $F_{3_c}(t)$ and the roll moment, $M_{4_c}(t)$ have a negative sign.

The last force caused on the vessel from the cushions is caused by the ventilation of cushion air through the ventilation valves. Following Newton's third law of motion, as the pressurized air escapes out from the ventilation valves in the cushions, an equal and opposite force caused by the velocity and mass of the escaping air, will act on the vessel. This force can be calculated as

$$F = \rho_a A^{ctrl} v_a^2 \tag{36}$$

where A^{ctrl} is the controlled leakage area of the chamber, and v is the velocity of the air. Note that v can also be written as $\frac{Q}{A}$, as these are the units that have mainly been used through the modeling. This generates a force in sway as well as a moment in roll and yaw. As previously mentioned, only the generated moment in roll, which can be described by equation (37), is regarded in this model.

$$\begin{aligned} M_{4_Q}(t) = &-\sum_{i=2}^{3} z_{ca_i} \rho_{c_i}(t) \frac{Q^2_{out_i}(t)}{A^{ctrl}_i(t)} \\ &+ \sum_{i=\{1,4\}} z_{ca_i} \rho_{c_i}(t) \frac{Q^2_{out_i}(t)}{A^{ctrl}_i(t)} \end{aligned} \tag{37}$$

In the equation above, Q_{out_i} is the volumetric flow out of the cushion, as expressed in equation (25). x_{ca_i} and z_{ca_i} is the distance from the vessel center of gravity to the center of area for the cushion ventilation valve, also known as the controlled leakage area, A^{ctrl}. The combined resulting forces acting on the vessel from the cushions and corresponding air-flow can be written as

$$\boldsymbol{\tau_{combined}} = \boldsymbol{\tau_c} + \boldsymbol{\tau_Q}. \tag{38}$$

Here $\boldsymbol{\tau}$ is a vector represented as
$\boldsymbol{\tau} = [F_1, F_2, F_3, M_4, M_5, M_6]$, with the corresponding subscripts of c and Q.

3. SES-SIM

The mathematical model derived in the section above is implemented in MATLAB®/Simulink®. The equations governing the SES-cushion dynamics and the corresponding forces are integrated into a larger system referred to as SES-sim. An illustration of the structure of this system is given in figure 4.

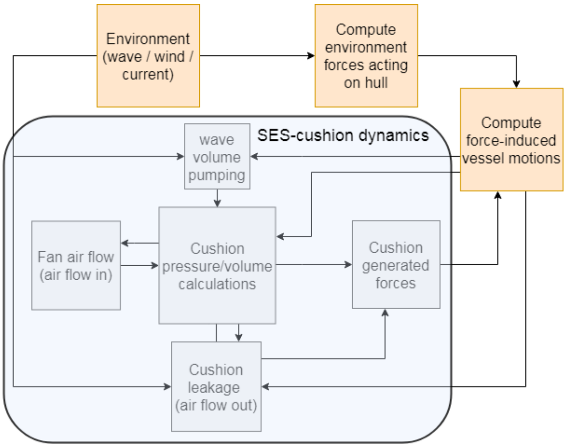

Fig. 4. Diagram of the SES-sim model structure

The orange blocks are taken from the Marine System Simulator (MSS), created by Fossen and Perez 2004, with a few additions and changes by Umoe Mandal. The blue square contains a simplified overview of the different equations derived above gathered into modules. The MSS toolbox takes forces acting on the vessel as input, and returns the 6 degrees of freedom movement for the vessel. It is also used to generate the waves and other environmental forces acting on the vessel.

3.1 *Simulated pitch movement*

Figure 5 shows the results from a pitch induced motion caused by opening and closing the aft and bow ventilation by using two sinusoidal functions in counter-phase.

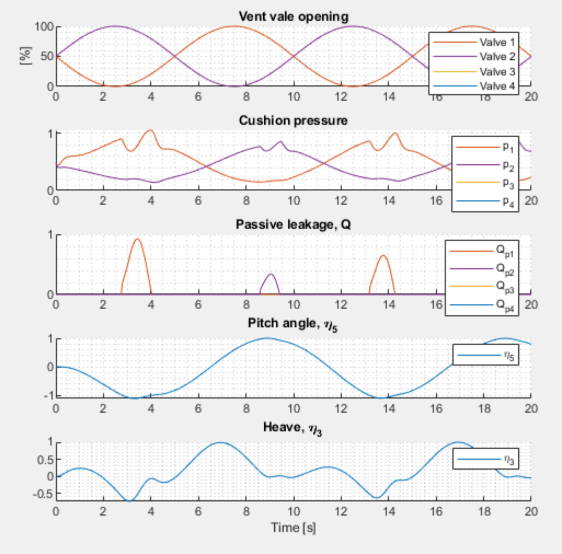

Fig. 5. Vessel dynamics from two sinusoidal vent valve signals

The purpose of the test is to confirm that the mathematical model developed above and its implementation into Simulink® produces a reasonable vessel response. The valves and cushions are numbered as illustrated by figure 2. Opening the aft valves causes a reduced pressure in the aft cushions, which leads to an induced pitch angle. When the pitch angle becomes too large, the front of the vessel is lifted out of the water, and passive air leakage occurs from the front chambers. As expected, this causes a pressure drop in the front cushions. From the graph displaying pitch angle, it's possible to recognize that the pitch velocity changes at this point. Furthermore, as the pressure drops in the front cushions, the vessel heave increases, which is expected as the positive heave direction is defined as down. The following pressure spike can be explained by the vessel bow accelerating downwards due to the pressure loss, and subsequently being cushioned by the air cushion as the leakage stops.

3.2 Scale model comparison

An early experimental results with scale model of SES with split cushions is used to validate the developed model. For this test a minor leakage area is added to the cushion dividers. Since the scale model visibly had leakage between the cushions during testing, in the developed model a minor leakage area is added to the cushion dividers i.e. the cushion dividers could not be assumed to be solid.

The first comparative test is a test of the maximum static pitch angle. The simulation is shown with and without the solid walls assumption. In the test for figure 7, the model had a slight steady roll angle, which results in a pressure increase in cushion 1, and a slight pressure drop in cushion 4. The variation in cushion pressure for the simulation is slightly higher than for the physical model. The cushion pressure lifts approximately 70% of the weight of the vessel for this test.

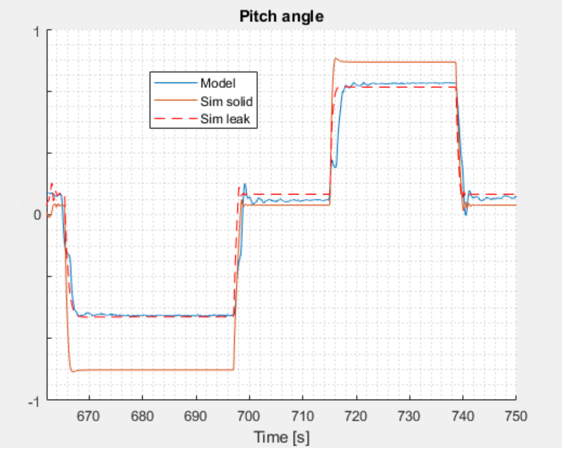

Fig. 6. Maximum static pitch angle for physical model and simulation with and without 'solid walls'.

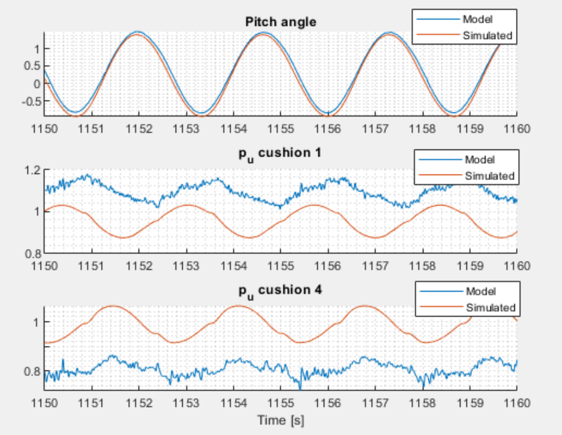

Fig. 7. Vessel dynamics in 1.5 meter 8s period waves.

4. CONCLUSION

The mathematical model seems to provide a good representation of the physical response for a surface effect ship. The exactness of the model seems to be quite dependent on factors regarding the leakage of air from the cushion chambers. Unfortunately these factors are hard to know before any physical testing has been done. Over all, the tests show that a four cushion solution provides a very potent solution to vessel pitch control. Due to the limited length of this paper, and limited experimental data, the focus for model verification has been on pitch. Similar results are expected for roll, with further experimental data planned for near future.

REFERENCES

Kaplan, P. and S. Davis (1978). *(1978), System analysis techniques for designing ride control system for ses craft in waves.* Proceedings of the 5th Ship Contr. Syst. Symp., , Annapolis, Maryland, USA.

Sørensen, A. J. and O. Egeland (1995). “Design of Ride Control System for Surface Effect Ships using Dissipative Control”. In: *Automatica* 31.2, pp. 183–199.

Fossen, T. I. and T. Perez (2004). *Marine Systems Simulator (MSS).* URL: `URL:%20https://github.com/cybergalactic/MSS`.

Perez, T. (2005). *Ship Motion Control: Course Keeping and Roll Reduction using Roll and Fins. Advances in Industrial Control Series.* Springer-Verlag, London, UK.

Auestad, Ø. F. (2015). “The Boarding Control System: Modelling and Control of a Surface Effect Ship for improved accessibility to Offshore Wind Turbines.” In: *PhD thesis, Department of Engineering Cybernetics, Norwegian University of Science and Technology.*

Ø. F. Auestad, Et Al. (2015). “Jan T. Gravdahl, Tristan Perez, Asgeir J. Sørensen. Boarding control system for improved accessibility to Offshore Wind Turbines: Full-scale testing”. In: *Elsevier.*

Mandal, Umoe (2018). *WAVE CRAFT: The Seaborne Helicopter.* URL: `https://www.wavecraft.no/model/voyager-38x/`.

E.2 Roll and Pitch Damping of a Surface EffectShip Utilizing a Four Cushion Solution

Roll and Pitch Damping of a Surface Effect Ship Utilizing a Four Cushion Solution

Ola M. Haukeland * **Vahid Hassani** *,** **Øyvind Auestad** ***

* *Centre for autonomous marine operations and systems (AMOS), Dept. of Marine Technology, Norwegian Univ. of Science and Technology, Trondheim, Norway.*
** *Department of Ships and Ocean Structures, SINTEF Ocean, Trondheim, Norway.*
*** *Umoe Mandal AS, Mandal, Vest-Agder, Norway.*

Abstract: This paper introduce damping of roll and pitch motion on a Surface Effect Ship (SES) in low vessel speeds. The SES consist of two side-hulls, a reinforced rubber bow and stern seal skirt system and four air cushion. The air cushions can lift 20-85 % of the total vessel mass depending on the output of the controller. The pressure in the air cushions are controlled using feedback from gyros which results in heavily reduced motions in roll and pitch. The effectiveness of the proposed system is examined through numerical simulation in a high fidelity simulator as well as experimental model tests with scale SES model at SINTEF Ocean's Basin.

Keywords: Surface Effect Ship, Split Cushion, Process Plant Model

1. INTRODUCTION

The Surface Effect Ship (SES) is a seagoing vehicle that traditionally operates at high-speed at the interface area between air and water. This is possible due lift fan(s) that blows air into an air cushion and thereby pressurizing it. The air cushion is a trapped volume underneath the vessel enclosed by the water surface, side-hulls, bow and stern seals. The seals inhabit the same structural properties found on the seals of a hovercraft but with a different geometry. Figure 1 gives an illustration of a SES cross-section, as seen from the side.

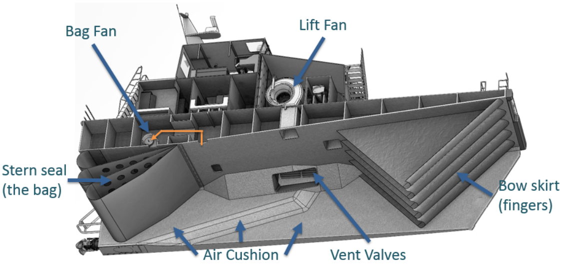

Fig. 1. Cross section of a SES. Illustration by Umoe Mandal.

The SES discussed in this paper is slightly modified compared to the traditional SES since the volume underneath the vessel is divided into four air cushions and not one. In addition to inheriting the high-speed, the SES discussed in this paper also present roll and pitch motion control at low speeds which is the topic of this work. Roll and pitch damping is possible by altering the pressures individual in the four chambers. For instance, if the two starboard cushions have higher pressure then on the port side, then the motion induced by a sea wave crest encountering the port deck-side can be damped.

Though this project is done in collaboration with Umoe Mandal, the properties of the simulated model are generic. The results given in chapter 4 do not represent any one of Umoe Mandal's vessels in particular.

1.1 Motivation

The rough seas surrounding offshore structures such as oil platforms, oil-rigs and wind turbines provide a challenge for both crew transport and offshore structure inspections. The use of surface effect ships has emerged as a competitive alternative to helicopter transport, proving high levels of safety, comfort, fuel efficiency and overall reduced cost of offshore logistics, Mandal 2018. The main challenge for sea transport is safety at crew transfer and ride comfort at high transit speeds. Increased motion control and motion damping provides the solution to these challenges, and contributes to an expand of the operational window for marine vessels at harsh weather conditions.

1.2 Simulation environment

The numerical simulations will be carried out in a process plant model referred to as SESSim, Haukeland 2019. This is a mathematical model implemented in MATLAB®/Simulink®, created to accurately depict the dynamics of the surface effect ship. The model is expanded to include the four cushion solution, and also provides the basis for the derivation of the control plant model in section 2.

1.3 SES Cushion-control

Other systems for controlling a SES-vessel by manipulating the cushion pressure are already developed and in use, among them is the ride control system and the boarding control system. The ride control system was first featured in Kaplan and Davis 1978, and has since been further developed by Sørensen and Egeland 1995. The purpose of the system is to create a more smooth ride at high transit velocities. The system provides active damping of vertical motions by manipulating and reducing the cushion pressure fluctuations caused by rough sea. The boarding control system has been developed by Ø. F. Auestad 2015. The main use of the boarding control system is to reduce the movements of the vessel's bow, so that it is possible to secure safer transfer from the ship to offshore structures, specifically, offshore wind-turbines. The boarding control system relies on manipulating the pressure of the single cushions to counteract the wave-induced motions.

1.4 Cushion division

In this paper, we consider a SES design in which the single cushion is divided into four sections by the use of solid walls or inflatable separators. The division and subsequent cushion numbering can be seen in figure 2. The implementation of the four chambers solution using inflatable bags allows for usage of a the traditional one-cushion solution when the four cushion division is not needed.

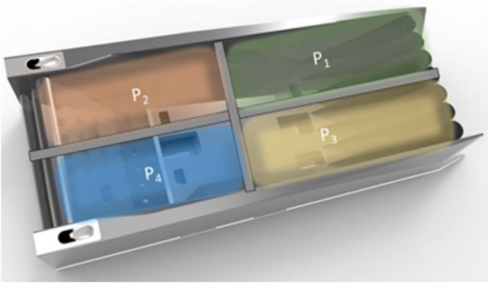

Fig. 2. The cushion separation and numbering as seen from above.

2. MATHEMATICAL MODEL

A linear time-invariant mathematical model is developed for the system to act as a control plant model. Ultimately the model will be expressed on the LTI-state space form. The derivation of the linear representation of the four cushion SES dynamics is based on the non-linear process plant model derived in Haukeland 2019.

2.1 Cushion pressure dynamics

The cushion pressure is considered to be uniform within each cushion chamber. The pressure in each chamber is denoted p_{c_i} and can be expressed as shown in equation 1.

$$p_{c_i}(t) = p_a + p_{u_i}(t) \tag{1}$$

Here p_a is the atmospheric pressure, while $p_{u_i}(t)$ is the uniform excess pressure. When the vessel is in equilibrium, meaning it has no movement, the excess pressure p_{u_i} is defined as the equilibrium pressure, p_{0_i}. The excess pressure can be written in a non-dimensional form as μ_u, where

$$\mu_{u_i}(t) = \frac{p_{u_i}(t) - p_0}{p_0} \tag{2}$$

As the vessel is designed for a single cushion solution with the option of four cushions, and the walls of the cushions are considered thin, assuming that the equilibrium pressure p_0 is the same for all of the cushions is reasonable. The volume of air inside each cushion will vary with the elevation of the water surface as well as the heave, pitch and roll of the vessel. The interaction between the volume, air leakage, wave volume pumping of the cushions and the equations of motion for the vessel can be expressed as shown in equation 3. This equation is based on the uniform pressure equation derived in Sørensen and Egeland 1995. The equation has since been altered and expanded to fit the current system and four cushion solution. Note that the equation is a linearization, and is only valid for small changes in pressure around the linearization point at p_0.

$$\begin{aligned} K_{1_i}\dot{\mu}_{u_i}(t) + &K_3\mu_{u_i}(t) + \rho_{c0}A_{c_i}\dot{\eta}_3(t) \\ &+\rho_{c0}A_{c_i}y_{cp_i}\dot{\eta}_4(t) - \rho_{c0}A_{c_i}x_{cp_i}\dot{\eta}_5(t) \\ &= K_{2_i}\Delta A_{2_i}^{ctrl}(t) + \rho_{c0}\dot{V}_{0_i}(t) \end{aligned} \tag{3}$$

Here A_{c_i} is the area of cushion i, projected onto the water plane. The constants x_{cp_i} and y_{cp_i} are the centers of pressure, or center of area for each of the cushions. The constants K_{1_i}, K_{2_i} and K_3 are calculated as shown in the equations below.

$$K_{1_i} = \frac{\rho_{c0}V_{c0_i}}{\gamma(1 + \frac{p_a}{p_0})} \tag{4}$$

$$K_{2_i} = \rho_{c0}c_{n_i}\sqrt{\frac{2p_0}{\rho_a}} \tag{5}$$

$$K_3 = \rho_{c0}\sum_{j=1}^{q}\left(\frac{Q_{0j}}{2} - p_0\frac{\partial Q}{\partial p}\bigg|_{0j}\right) \tag{6}$$

Here ρ_a is the atmospheric air density, and p_a is the atmospheric pressure. Similarly, p_0 and ρ_0 is the cushion equilibrium pressure and air density, while γ is the ratio of specific heat for air. Q_{0j} is the air flow rate at the forementioned equilibrium pressure, while $\frac{\partial Q}{\partial p}|_{0j}$ is the corresponding linearized fan slope around the equilibrium point $0j$. Here subscript j denotes the numbering of the fans, providing air-flow Q. Lastly, c_n is the leakage coefficient, which is dependent on the shape of the leakage area. $\dot{V}_{0_i}(t)$ is the wave volume pumping, which is further explained and derived in Haukeland 2019, but can be expressed as shown in equation 7. Note that V_{c0_i} denotes the cushion volume for cushion i at the equilibrium pressure, and is not related to the wave volume pumping.

$$\dot{V}_{0_i}(t) = \int_{y_{1_i}}^{y_{2_i}}\int_{L_{1_i}}^{L_{2_i}}\dot{\zeta}(x, y, t)dA \tag{7}$$

$$V_{0_i}(t) = \int_{y_{1_i}}^{y_{2_i}}\int_{L_{1_i}}^{L_{2_i}}\zeta(x, y, t)dA \tag{8}$$

Here y_{1_i} and y_{2_i} constitute the width of cushion i, while L_{1_i} to L_{2_i} constitutes the length of cushion i, measured at the current water-level. $\dot{\zeta}(x, y, t)$ is the function expressing the rate of change in the wave elevation at position x and y, at time t. This rate of change can be expressed as shown in equation 9, and is further detailed in Haukeland 2019.

$$\dot{\zeta}(x,t) = \bar{\zeta}\omega \cos\left(\omega t + \epsilon - k(x\cos(\chi) + y\sin(\chi)\right) \tag{9}$$

2.2 Equations of motion

Only the forces in heave, roll and pitch will be of relevance to the control and simulations of the vessel dynamics in this paper. The vessel is considered stationary, such that the forces and moments in surge, sway and yaw will be negligible. The sum of forces acting on the vessel can be split into two components. Forces generated by the excess pressure in the cushions, and forces generated as a result of the buoyancy and hydrodynamic properties of the hull. Equations 10 through 12 express the forces and moments generated by the cushions in heave, roll and pitch.

$$F_{3_c}(t) = \sum_{i=1}^{4} -p_0 \mu_{u_i}(t) A_{z_i} \tag{10}$$

$$M_{4_c}(t) = \sum_{i=1}^{4} -y_{cp_i} p_0 \mu_{u_i}(t) A_{z_i} \tag{11}$$

$$M_{5_c}(t) = \sum_{i=1}^{4} x_{cp_i} p_0 \mu_{u_i}(t) A_{z_i} \tag{12}$$

Equations 13 through 15 express the equations of motion for the vessel. The hydrodynamic forces acting on the vessel are expressed through the first three terms on the left hand side of the equations. These forces and moments and the corresponding movements of the vessel can be stated as a mass-spring-damper system for each of the degrees of freedom.

$$(m + A_{33})\ddot{\eta}_3(t) + B_{33}\dot{\eta}_3 + C_{33}\eta_3 + F_{c_3}(t) = F_3^e(t) \tag{13}$$

$$(I_{44} + A_{44})\ddot{\eta}_4(t) + B_{44}\dot{\eta}_4 + C_{44}\eta_4 + M_{c_4}(t) = M_4^e(t) \tag{14}$$

$$(I_{55} + A_{55})\ddot{\eta}_5(t) + B_{55}\dot{\eta}_3 + C_{55}\eta_5 + M_{c_5}(t) = M_5^e(t) \tag{15}$$

The forces and moments $F_3^e(t)$, $M_4^e(t)$ and $M_5^e(t)$ are excitation forces and moments caused by waves and other external forces. The constant m represents the vessel mass, and the constants A, B and C represents the hydrodynamic added mass, the potential damping and restoring coefficient for the mass-spring-damper motion of the vessel. Their subscripts 3, 4 and 5 denote the movements in heave, roll and pitch, respectively. Lastly the vessel inertia governing the roll and pitch motion of the vessel is given as I. The values for these constants are been computed in ShipX and Veres, and have been provided and Umoe Mandal.

2.3 State space representation

The equations of motion can be represented in the linear time-invariant state-space form shown in 16 and 17.

$$\dot{\boldsymbol{x}}(t) = \boldsymbol{A}\boldsymbol{x}(t) + \boldsymbol{B}\boldsymbol{u}(t) + \boldsymbol{E}\boldsymbol{\omega}(t) \tag{16}$$

$$\boldsymbol{y}(t) = \boldsymbol{C}\boldsymbol{x}(t) \tag{17}$$

Here, $\boldsymbol{x}(t)$ is the state vector, which represents the relevant degrees of freedom of the vessel. The representation of the vector $\boldsymbol{x}(t)$ is listed in the table below. $\boldsymbol{u}(t)$ is the control input, which will be further discussed in section 3. $\boldsymbol{\omega}(t)$ is the disturbance vector, which comprises of external forces and disturbances. $\boldsymbol{y}(t)$ is the output vector, and holds the values for any measured states such as data from accelerometers or gyros. The expressions for the matrices $\boldsymbol{A}$, $\boldsymbol{B}$, $\boldsymbol{E}$ and $\boldsymbol{C}$ can be found in the thesis, **Suggestions on thesis title?**

States $\boldsymbol{x(t)}$

State	Description	Symbol
$x_1(t)$	Heave position	η_3
$x_2(t)$	Roll angle	η_4
$x_3(t)$	Pitch angle	η_5
$x_4(t)$	Heave velocity	$\dot{\eta}_3$
$x_5(t)$	Roll velocity	$\dot{\eta}_4$
$x_6(t)$	Pitch velocity	$\dot{\eta}_5$
$x_7(t)$	Non-dim. pressure, chamber 1	μ_{u_1}
$x_8(t)$	Non-dim. pressure, chamber 2	μ_{u_2}
$x_9(t)$	Non-dim. pressure, chamber 3	μ_{u_3}
$x_{10}(t)$	Non-dim. pressure, chamber 4	μ_{u_4}

States $\boldsymbol{y(t)}$

State	Description	Symbol
$y_1(t)$	Roll angle	η_4
$y_2(t)$	Pitch angle	η_5
$y_3(t)$	Heave velocity	$\dot{\eta}_3$
$y_4(t)$	Roll velocity	$\dot{\eta}_4$
$y_5(t)$	Pitch velocity	$\dot{\eta}_5$
$y_6(t)$	Pressure, chamber 1	p_{c_4}
$y_7(t)$	Pressure, chamber 2	p_{c_4}
$y_8(t)$	Pressure, chamber 3	p_{c_4}
$y_9(t)$	Pressure, chamber 4	p_{c_4}

3. CONTROLLER DESIGN

We wish to device a simple but reliable controller which ultimately can be applied to a real vessel similar to the one described by our model. We desire to control the roll and pitch of the vessel, and so a simple P-velocity controller is applied. The control law is formulated as shown in equation 18 below.

$$\boldsymbol{u}(t) = -\boldsymbol{K}\boldsymbol{x}(t) + \boldsymbol{\beta} \tag{18}$$

The controller output, $\boldsymbol{u}(t)$, returns the opening percentages of the cushion ventilation valves. A controller output of 100 reads 100% opening on the vent valve, and thus the corresponding cushion pressure is minimized. $\boldsymbol{\beta}$ is a constant matrix signifying the bias of the ventilation valve louvers. The bias essentially states how much lift the vessel should have when no feedback is present. The structure of the control output matrix is shown below. The subscripts denote the ventilation valve louvers corresponding to the equally numbered cushion chamber.

$$\boldsymbol{u}(t) = [u_1(t)\ u_2(t)\ u_3(t)\ u_4(t)] \tag{19}$$

3.1 Stability of the closed loop system

An unstable system can easily lead to unexpected and undesired responses. For physical systems, such responses can easily produce dangerous and harmful situations. Thus, providing a stability proof for the controlled system gives an assurance that the controlled system will only act in a certain way, namely converging towards the equilibrium states of $\boldsymbol{x_0} = 0$.

Stability of unperturbed system The unperturbed closed loop system, that is $\boldsymbol{E\omega}(t) = 0$, can be said to be exponentially stable around $\boldsymbol{x}_0$ if the closed loop system matrix, $\boldsymbol{A}_{cl}$ is Hurwitz. This means that all the eigenvalues of $\boldsymbol{A}_{cl}$ have strictly negative real parts, i.e $\mathbb{R}(\lambda_i) < 0$. By inserting the expression of our chosen controller in 18 into the unperturbed state space representation of our system in 16, the closed loop system can be expressed as

$$\dot{\boldsymbol{x}}(t) = \boldsymbol{Ax}(t) - \boldsymbol{BKx}(t) + \boldsymbol{B\beta} = \boldsymbol{A}_{cl}\boldsymbol{x}(t) + \boldsymbol{B\beta} \qquad (20)$$

where $\boldsymbol{A}_{cl} = \boldsymbol{A} - \boldsymbol{BK}$. A general expression for the values of $\boldsymbol{K}$ which create a stable closed loop system can be devised by choosing an appropriate Lyapunov function, $\boldsymbol{V}(x)$ through use of the Lyapunov equation. Due to the size of the matrix $\boldsymbol{A}_{cl}$ and the number of unique gains in the $\boldsymbol{K}$-matrix, such a generalization will become long and tedious. Thus we settle for showing that the selected gains in section 3 will provide a stable closed loop system. The eigenvalues for the closed loop system are calculated in MATLAB®, through the command $eig(A_{cl})$. The resulting eigenvalues all have negative real parts. Thus the closed loop unperturbed system will converge exponentially fast towards the equilibrium states of $\boldsymbol{x}_0$.

Robustness of perturbed system As the purpose of the system will be to counteract disturbances, the perturbed system, where $||\boldsymbol{E\omega}(t)|| \neq 0$, must be shown to be robust. That is, small disturbances will not result in large steady-state deviations from the equilibrium. The perturbations affecting the vessel are time dependent, and do not stop as the system reaches it's equilibrium point, thus the perturbations can be seen as non-vanishing. This means that we can no longer expected the system to converge at the origin as $t \to \infty$. The best we can hope for is that the system response will be bounded by some small bound, if the disturbance is small, Khalil 2014. The closed loop perturbed system can be written as

$$\dot{\boldsymbol{x}}(t) = \boldsymbol{A}_{cl}\boldsymbol{x}(t) + \boldsymbol{E\omega}(t) + \boldsymbol{B\beta} \qquad (21)$$

The Lyapunov function candidate for the system, $\boldsymbol{V}(x)$, is set as

$$\boldsymbol{V}(x) = \boldsymbol{x}^T\boldsymbol{Px} \qquad (22)$$

Differentiating $\boldsymbol{V}(x)$ with respect to time will provide an expression for the direction of the trajectory of the system. Thus if $\dot{\boldsymbol{V}}(x)$ is negative for all x, the system will be stable. $\dot{\boldsymbol{V}}(x)$ can be derived as

$$\begin{aligned}\dot{\boldsymbol{V}}(x) =& \boldsymbol{x}^T\boldsymbol{P}\dot{\boldsymbol{x}} + \dot{\boldsymbol{x}}^T\boldsymbol{Px} \\ =& -\boldsymbol{x}^T\boldsymbol{Qx} + \boldsymbol{x}^T\boldsymbol{PE\omega} + \boldsymbol{\omega}^T\boldsymbol{E}^T\boldsymbol{Px}\end{aligned} \qquad (23)$$

where

$$-\boldsymbol{Q} = \boldsymbol{PA_{cl}} + \boldsymbol{A_{cl}}^T\boldsymbol{P} \qquad (24)$$

Equation 24 is called the Lyapunov equation. If there exists a solution for the Lyapunov equation where both $\boldsymbol{P}$ and $\boldsymbol{Q}$ are square positive definite matrices, that is $\boldsymbol{P} = \boldsymbol{P}^T > 0$ and $\boldsymbol{Q} = \boldsymbol{Q}^T > 0$, then $\dot{\boldsymbol{V}}(x)$ for the unperturbed will be negative, and the system will be stable. Since the system is perturbed, $\boldsymbol{Q}$ must satisfy the inequality shown below.

$$-\boldsymbol{Q} \leq \boldsymbol{PE\omega} + \boldsymbol{\omega}^T\boldsymbol{E}^T\boldsymbol{P} \qquad (25)$$

Values for $\boldsymbol{P}$ and $\boldsymbol{Q}$ can be calculated from the unperturbed system. Given that the values for the disturbance, $\boldsymbol{\omega}$, are small enough to satisfy the inequality in 25, the perturbed closed loop system will produce a bounded response. Lemma 9.2 in Khalil 2014 can be applied as the nominal system has exponential stability about x_0, and because the Lyapunov function candidate for the nominal system, chosen in 22, satisfy the inequalities 26 through 28 for $[0, \infty) \times \boldsymbol{D}$, where $\boldsymbol{D} = \{\boldsymbol{x} \in R^n \ | \ ||\boldsymbol{x}|| < r\}$. Thus Lemma 9.2 states that the the system response will be bounded by b, following $||\boldsymbol{x}|| \leq b$.

$$c_1||x||^2 \leq V(x) \leq c_2||x||^2 \qquad (26)$$

$$\frac{\partial V}{\partial x}f(x) \leq -c_3||x||^2 \qquad (27)$$

$$\left|\left|\frac{\partial V}{\partial x}\right|\right| \leq c_4||x|| \qquad (28)$$

4. NUMERICAL SIMULATIONS

The simulations are carried out in the environment expressed by the process plant model derived in Haukeland 2019. Zero perforating air leakage is assumed, i.e. all chamber walls are considered solid. The focus of the numerical simulations will be on control of roll and pitch. All the simulations below will have a fixed bias of $\boldsymbol{\beta} = 42.8$, which corresponds to the equilibrium pressure, p_0, for this vessel. The control gains will be fixed as found in section 3. All the tests will be simulated with and without the closed loop controlled system, in order to generate comparative data.

4.1 Pitch control

This section present results of numerical simulations where the system is excited with waves described in Table 1.

Table 1. Wave description

Regular sea	
Wave height, H_a	1 to 2.5 meters
Period, T_p	4 to 12 seconds
Direction, ψ	0°

Regular oncoming waves generating only pitch momentum are simulated to investigate the pitch-stabilizing properties of the closed loop controlled system. Several test are performed under the same conditions, but with varying wave periods, T_p, and wave height, H_a. The comparative results between the controlled and uncontrolled system are displayed in table 2. The detailed results for one of the simulations is displayed in Figure 3. The first plot in the Figure above displays the controlled and uncontrolled pitch angle for the simulation of $T_p = 8s$ waves. The second plot displays the valve openings of two adjacent cushions. The bottom two graphs display the pressure with and without control in one of the two aft and and one of the two rear cushions, respectively. The uncontrolled pitch has a maximum significant angle of 9.64 degrees, meaning that

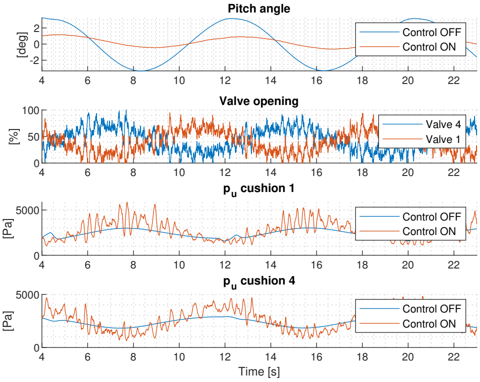

Fig. 3. Pitch angle, valve opening, cushion 1 pressure, cushion 4 pressure, for a $T_p = 8s$ wave.

one third of the largest pitch angles will be 9.64 degrees peak to peak height or larger. The controlled pitch for the same case, has a significant angle of 2.11 degrees. This constitutes a 78.1% reduction of the significant peak to peak pitch angle, and a reduction of roughly 7.5 degrees from peak to peak.

Table 2. Significant angle pitch movement with control OFF/ON

T_p	H_a	H_s-OFF	H_s-ON	Damping
4s	1m	3.17	0.783	75.3 %
5s	1m	3.72	0.804	78.4 %
6s	1m	3.98	0.855	78.8 %
7s	2.5m	9.64	2.11	78.1 %
8s	2.5m	9.08	2.05	77.4 %
9s	2.5m	8.53	2.03	76.1 %
10s	2.5m	7.94	1.95	75.5 %
11s	2.5m	7.48	1.92	74.3 %
12s	2.5m	6.98	1.84	73.8 %

4.2 Roll control

This section present results of numerical simulations where the system is excited with waves described in Table 3

Table 3. Wave description

Regular sea	
Wave height, H_a	1 to 2.5 meters
Period, T_p	4 to 12 seconds
Direction, ψ	90°

The roll properties of the vessel is tested in the same way as the pitch, with a regular wave, but coming from the side. The closed loop roll movements of the vessel for one specific wave period and height can be seen in Figure 4. As with the pitch test, table 4 displays the overall results from the varying wave height and periods. The uncontrolled roll has a maximum significant angle of 15.0 degrees. The controlled pitch for the same case, has a significant angle of 2.51 degrees. This constitutes a 83.4% reduction of the significant peak to peak pitch angle, and a reduction of roughly 12.5 degrees from peak to peak.

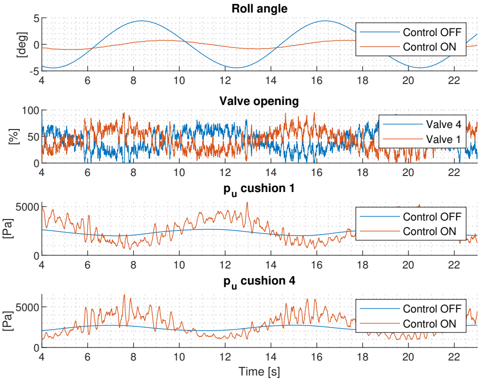

Fig. 4. Roll angle, valve opening, cushion 1 pressure, cushion 2 pressure, for a $T_p = 8s$ wave.

Table 4. Significant angle of roll movement with control OFF/ON

T_p	H_a	H_s-OFF	H_s-ON	Damping
4s	1m	9.95	1.20	88.0 %
5s	1m	9.23	1.20	87.0 %
6s	1m	7.66	1.12	85.4 %
7s	2.5m	15.0	2.51	83.4 %
8s	2.5m	12.3	2.28	81.5 %
9s	2.5m	10.2	2.10	79.5 %
10s	2.5m	8.54	1.93	77.4 %
11s	2.5m	7.29	1.78	75.5 %
12s	2.5m	6.22	1.69	72.8 %

4.3 Roll and pitch control in irregular seas

The sea conditions tested in this section is given as in Table 5.

Table 5. Wave description

JONSWAP, irregular sea	
Significant height, H_s	2.5 meters
Peak wave period, T_p	Avg. 7 seconds
Wave heading, ψ	0° to 360° at 22.5° increments
Spectral peakedness, γ	3.3

A total of 18 simulations are presented in Figure 8. Half of them are with control on, the other half with control off. Each simulation is 500 seconds long. The aim is to test simultaneous control of both pitch and roll in a realistic sea-state, and document the efficiency of the controller in various headings. The roll and pitch time series of the controlled and the uncontrolled vessel for $\psi = 135°$ can be seen in Figures 5 and 6.

The over all reduction in roll for the 360 degree wave-direction arch is 74.9%. Similarly, the error of the pitch angle is reduced by 73.1%.

The radial plot in Figure 8 shows that for angles where no roll or no pitch should occur, the control system tends to increases the roll or pitch. This is because both pitch and roll movement can be induced by the cushions via noise or small amplified excitation forces. Figure 7 displays the

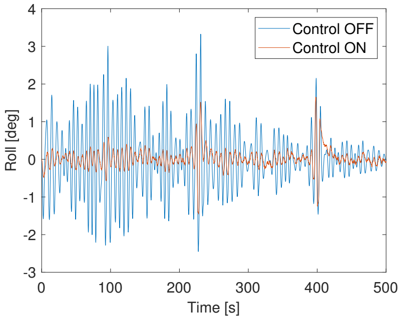

Fig. 5. Roll angle with and without cushion control, $\psi = 135°$.

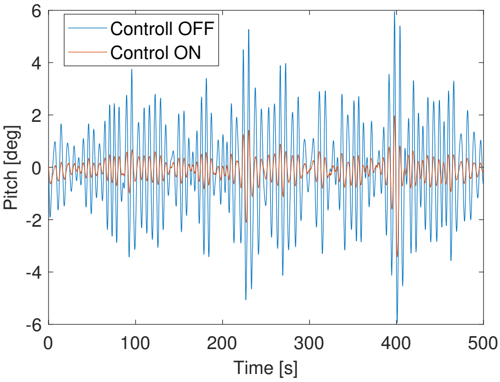

Fig. 6. Pitch angle with and without cushion control, $\psi = 135°$.

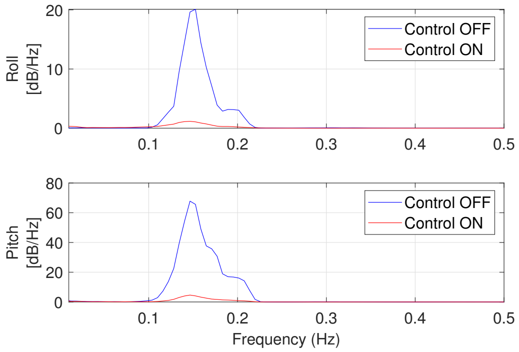

Fig. 7. Roll and pitch angle power spectral density, $\psi = 135°$.

power spectral density (PSD) of the roll and pitch angle with and without active cushion control.

5. EXPERIMENTAL MODEL TEST

A scaled model of a SES design by UMOE Manadal AS is built in SINTEF Ocean and a series of experiment are carried out in SINTEF Ocean's Laboratory (more test to be carried in near future). Fig. 9 shows the scale model in SINTEF Ocean's Basin. A soft mooring system is designed to keep the model at center of the basin without influencing the dynamics of the vessel. The Table 6 summarizes the wave description that was created during the model test.

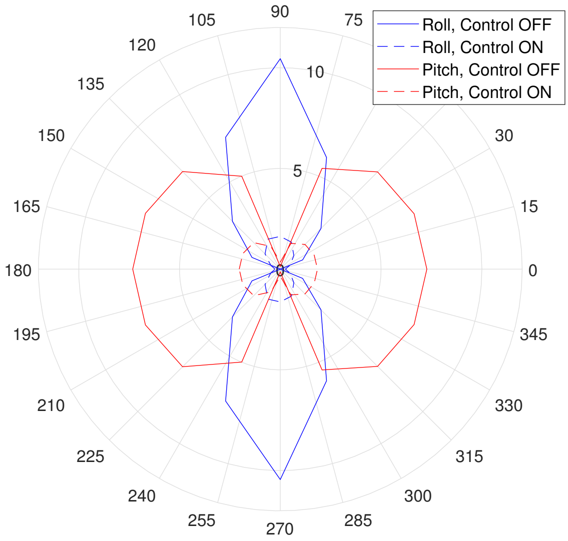

Fig. 8. Roll and pitch angles for all headings. The angles of the radial plot show $\psi[°]$. The radius shows significant roll and pitch magnitude.

Fig. 9. Scale model SES in the ocean basin at SINTEF Ocean.

Table 6. Wave description in experimental test

Regular sea	
Wave height, H_a	2.5 meters
Period, T_p	8 seconds
Direction, ψ	180°

The plot in Figure 10 shows the efficacy of a four cushion scale-model SES that has been used for experiments in the SINTEF Ocean's ocean basin. To maintain the preservation of intellectual property rights, the scale of the y-axis has been normalized on a scale of approximately 1 to -1. The significant height of the uncontrolled pitching motion on this normalized scale is 1.76. The corresponding significant height of the controlled pitching motion is 0.663, constituting a 62.3% reduction. This early experimental results agrees with our numerical simulation. The experimental results confirms high performance of split cushion concept for motion regulation in SES.

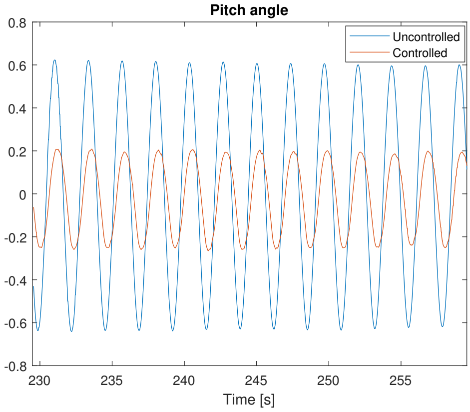

Fig. 10. Uncontrolled and controlled pitch movement in 2.5m, 8s head sea.

6. CONCLUSION

This paper presented active pitch and roll damping algorithm for motion regulation in a Surface Effect Ship (SES) with split cushion. The roll and pitch angles were reduced as much as 13 and 7 degrees, constituting more than a 83% and 78% reduction, respectively. The roll damping is especially efficient around the roll eigenperiod of the vessel. The results are predicated on the assumption that the cushion separation walls can be seen as solid. Early experimental testing in the SINTEF Ocean's Basin with scale model of SES agrees with numerical simulations studies and shows superior performance of split cushion SES in motion regulation.

REFERENCES

Kaplan, P. and S. Davis (1978). *(1978), System analysis techniques for designing ride control system for ses craft in waves.* Proceedings of the 5th Ship Contr. Syst. Symp., , Annapolis, Maryland, USA.

Sørensen, A. J. and O. Egeland (1995). "Design of Ride Control System for Surface Effect Ships using Dissipative Control". In: *Automatica* 31.2, pp. 183–199.

Khalil, Hassan K. (2014). *Nonlinear Systems, Third Edition.* Pearson Education Limited, Edinburgh Gate, Harlow, Essex CM20 2JE.

Ø. F. Auestad, Et Al. (2015). "Jan T. Gravdahl, Tristan Perez, Asgeir J. Sørensen. Boarding control system for improved accessibility to Offshore Wind Turbines: Full-scale testing". In: *Elsevier*.

Mandal, Umoe (2018). *Marine Systems Simulator (MSS).* URL: `URL:%20https://www.wavecraft.no/model/voyager-38x/`.

Haukeland, O. M. et al (2019). "Dynamic Modeling and Simulation of a Surface Effect Ship with Four Air Cushions". In: *submitted to the 12th IFAC Conference on Control Applications in Marine Systems, Robotics, and Vehicles (CAMS 2019).*